TÉCNICO LISBOA

Topological Optimization of an Interface Metal Structure

Rafael Vieira De Sequeira

Thesis to obtain the Master of Science Degree in

Mechanical Engineering

Supervisors: Prof. Nuno Miguel Rosa Pereira Silvestre
Eng. João Daniel Ramos Ricardo

Examination Committee

Chairperson: Prof. João Orlando Marques Gameiro Folgado
Supervisor: Prof. Nuno Miguel Rosa Pereira Silvestre
Member of the Committee: Prof. Hélder Carriço Rodrigues

October 2018

"Persistence is very important. You should not give up unless you are forced to give up."

Elon Musk

"Great things in business are never done by one person. They're done by a team of people."

Steve Jobs

"We all need people who will give us feedback. That's how we improve."

Bill Gates

"Life is a series of experiences, each one of which makes us bigger, even though sometimes it is hard to realize this. For the world was built to develop character, and we must learn that the setbacks and grieves which we endure help us in our marching onward."

Henry Ford

Dedicated to my family for all their support over these 23 years.

Acknowledgments

I would like to thank to everyone that somehow contributed to my development as a student and as a person along this course. But in special:

First of all, to my beloved family and Marta for all the love, unceasing strength, presence, tolerance and motivation to pursue nothing less than the very best.

To my dear friends, Bráulio, João and Pedro, for the company, patience, laughs, adventures and friendship shown.

To everyone that I knew in Formula Student project but in special to the suspension members: Vitor Santos, Tiago Martins, André Dinis, Gonçalo Pereira, Diogo Silva, António Bento and Carlos Carvalho.

To André Santos for the review of this work.

To my supervisor from Active Space Technologies, Eng. João Ricardo, for his guidance, advisement, availability and sympathy.

To Active Space Technologies for the internship opportunity.

To my supervisor from Instituto Superior Técnico, Professor Nuno Silvestre, for his confidence, availability and unquestionable support.

To the PhD student Sérgio Gonçalves and Professors Luis Sousa and Virginia Infante for their extensive technical support and availability shown.

To Mechanical Engineering Department (DEM) for the mechanical characterization tests in the Mechanical and Materials tests laboratory (LEM2) and to professor Paulo Fernandes for the 3D printing manufacturing in the Biomechanics of Tissues laboratory.

To Pedro Teixeira and João Vicente from Laboratório de Técnicas Oficinais (LTO) for the precious help with manufacturing and testing.

Resumo

Este trabalho começa por analisar a performance da interface estrutural para ensaios de vibração existente na *Active Space Tecnhologies* de forma a avaliar a sua performance. Visto que a estrutura pode ser melhorada, as diferentes vantagens da aplicação da optimização topológica em conjunto com processos de fabrico aditivo em peças com requisitos estruturais elevados no sector aeroespacial são retratadas.

No sentido de expandir o conhecimento do autor no campo da optimização topológica, vários exemplos de referência são analisados e comparados com os resultados conhecidos da literatura. Com base neste conhecimento, a metodologia do processo de optimização foi desenvolvida e implementada com sucesso. Esta metodologia foi validada através de ensaios experimentais de vibração que serviram de comparação ao modelo numérico desenvolvido. Este processo foi desenvolvido com requerimentos alternativos aos da peça em metal visto que o material utilizado foi um polímero.

O processo de optimização e design da peça final em metal utiliza a metodologia anteriormente validada e apresenta melhoramentos significativos em relação à solução existente na empresa.

Palavras-chave: Análise Modal, Fabrico Aditivo, Optimização Topológica, Optistruct, Redução de Massa

Abstract

This work starts with the analysis of *Active Space Technologies* interface structure for vibration tests in order to assess its performance. Since this structure can be improved, the several advantages of Topological Optimization and Additive Manufacturing in components with high requirements in the aerospacial sector are portrayed.

In order to expand the author's knowledge in the Topological Optimization field, several benchmark examples were analysed and compared with literature's known results. Using this base knowledge, the optimization process methodology was developed and implemented with success. This methodology was validated through an experimental vibration activity that was compared with the numerical model's results. This process was developed with different requirements from the metal structure's ones since the used material is a polymer.

The final metal structure optimization and design process is based on the validated methodology and presents significant improvements when compared to the company's current solution.

Keywords: Additive Manufacturing, Mass Reduction , Modal Analysis, Optistruct, Topological Optimization

Contents

List of Tables

List of Figures

Nomenclature

Greek symbols

ν	Poisson's ratio.
ω	Angular frequency.
ρ	Density.
σ	Normal stress.

Other Symbols

$[C]$	Damping matrix.
$[G_i]$	Diagonal matrix with the relations between the rigid elements' degrees of freedom.
$[K]$	Stiffness matrix.
$[M]$	Mass matrix.
$\frac{\partial}{\partial}$	Partial derivative in order to some variable.
$\frac{d}{dt}$	Total derivative in order to time.
ω_i	Natural frequencies vector.
$\{\ddot{u}\}$	Nodal acceleration vector.
$\{\dot{u}\}$	Nodal velocity vector.
$\{F\}$	Nodal force vector.
$\{u\}$	Nodal displacement vector.
x, y, z	Cartesian components.

Lower case letters - u(x),k(x),v(x),c Vector convention.

Upper case letters - U(x),K(x),M(x),F Matrix convention.

Roman symbols

$\sum$	Sum.

A Cross-sectional area.

a Acceleration.

C Compliance.

E Young's modulus.

F Force.

f Volume fraction.

g Inequality constraint.

h Equality constraint.

m Mass.

R Radius.

T Kinetic energy.

t Time.

V Potential energy.

v Volume.

x Design variable - Relative density distribution.

Subscripts

0 Initial.

Al L-shape structure's aluminum characteristics.

$allowable$ Allowable.

$applied$ Applied/present.

e Element.

$fatigue$ Fatigue.

g, h, i, j, k, n, N Computational indexes.

max Maximum.

min Minimum.

$polymer$ Polymer model's characteristics.

uts Ultimate/Tensile.

VM Von Mises.

y Yield.

Superscripts

new Most recent value.

old Value before the most recent one.

p Penalization power.

L Lower.

T Transpose.

U Upper.

Glossary

3DP 3D Printing.

AM Additive Manufacturing.

ASTM American Society for Testing and Materials.

AVE Advanced Video Extensometer.

BESO Bi-directional Evolutionary Structural Optimization.

CAD Computer-Aided Design.

CEN European Committee for Standardization.

CNC Computer Numerical Control.

CoG Center of Gravity.

Conv.Val Convergence value.

CPU Central Process Unit.

DED Directed Energy Deposition.

DMLS Direct Metal Laser Sintering.

DoF Degrees of Freedom.

EBM Electron Beam Melting.

ECSS European Cooperation for Space Standardization.

ESO Evolutionary Structural Optimization.

FAA Federal Aviation Administration.

FEA Finite Element Analysis.

FEM Finite Element Method.

FoS Factor of Safety.

GE General Electric.

GUI Graphical User Interface.

ISO International Organization for Standardization.

IST Instituto Superior Técnico.

Iter.num Current iteration number.

LENS Laser Engineered Net Shaping.

LOM Laminated Object Manufacturing.

Max.iter.num Maximum allowable iterations.

MBB Messerschmidt-Bölkow-Blohm.

MIT Massachusetts Institute of Technology.

MoS Margin of Safety.

NVH Noise, Vibration and Harshness.

OBJ Objective function value.

OC Optimality Criteria.

PBF Powder Bed Fusion.

pres. freq. Present frequency.

PSDO Partner Standards Developing Organization.

req. freq. Required minimum frequency.

Shaker Vibration Test System.

SIMP Solid Isotropic Material with Penalty.

SLM Selective Laser Melting.

SLS Selective Laser Sintering.

STEP Standard for the Exchange of Product Data.

STL Stereolithography.

Tetra Tetrahedral.

TO Topological Optimization.

UAM Ultrasonic Additive Manufacturing.

UC Ultrasonic Consolidation.

UV Ultraviolet.

Chapter 1

Introduction

1.1 Motivation

Recently, with 4.0 industry era, the Additive Manufacturing (AM) technologies for metallic materials have been deeply researched and consequently developed. The production of metal end-use products is already a reality that has the potential to expand significantly the engineers' design possibilities. Topological optimization (TO) is a very old (1904 Michell [1]) and known structural optimization technique that typically enables significant weight reductions. However, due to limitations from subtractive manufacturing, this technology has never been used to its most. Now, with the design freedom that AM can offer, TO can be further explored.

In the aerospace industry, one of the biggest challenges is ensuring very tight structural requirements with the lowest possible mass. The combination of TO with AM can significantly improve the design of aerospace structures with the already known materials such as aluminum or titanium alloys. Typically, the structural requirements are related with the component's stiffness which can be easily increased through very refined and complex structures that are common in TO.

Aligning the constant need of weight reduction from this industry with the author's desire of expanding his knowledge in the AM and structural optimization fields, a new opportunity with an internship on *Active Space Technologies* emerged.

1.2 Problem Overview

In order to guarantee the performance of the hardware systems in space, a vibration test is done to the satellites' hardware parts to ensure their safety during the launch [2]. This test recreates and assesses the dynamic response of the hardware system. For these experiments, it is necessary to use an interface structure between the Vibration Test System (Shaker) and the hardware part that needs to be tested.

The interface structure vibration mode must not influence the hardware system dynamic response. Therefore, to avoid resonance, a minimum value of 2500Hz for the first mode frequency is required since the experiments values can be in a range of 5Hz to 2000Hz. Besides, the shaker is only capable

of producing a load case of 22KN so, if a roughly approximation for the force calculation as in equation 1.1 is used, the acceleration value for the test is constrained by the mass value. For this reason, the minimization of mass is very important. At the same time, as for every mechanical system, its structural integrity shall be ensured with special attention to fatigue behaviour since it will be regularly excited in high frequency conditions which can lead to high cycle fatigue failures. The company'scurrent solution is made of an aluminum alloy since these ones can present very high ratios of mechanical properties compared to their densities. So, the company demands that this new design shall also be done with an aluminum alloy.

$$F = ma \tag{1.1}$$

This thesis aims to present a final design solution for the interface structure with a better performance than *Active Space Technologies* current solution (figure 1.1). Since this current solution was designed for a specific hardware system test, this thesis will also use this specific hardware system for the development of a feasible topological optimization process that can be used in this type of structures or in real satellites' support structures with similar working conditions and requirements. Apart from all the referred requirements, this structure shall also be designed to increase the assembly's (interface structure/real satellite support structure and hardware system) first mode frequency as high as possible to increase the hardware system's safety.

Structure's requirements summary:

- Minimum of 2500Hz as first mode frequency;
- Reduce the structure's mass;
- Structural integrity with special attention to fatigue;
- Using an aluminum alloy as material;
- Not a requirement but an advantage - Assembly's first mode frequency higher than the current one.

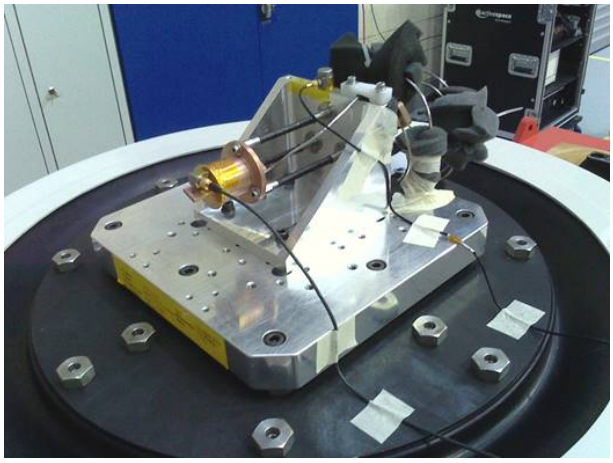

Figure 1.1: *Active Space Technologies* current solution.

1.3 Thesis Outline

The present thesis is divided into six chapters. The first chapter presents the author's motivation and this work's objectives. The second chapter starts with the finite element method fundamentals and continues with the current solution from *Active Space Technologies* analysis in order to assess its performance.

The state of the art of TO and AM is presented in chapter three with special focus on the TO and AM benefits and influence on the aerospace industry. Besides, the basic necessary technical background in TO to follow this thesis work is also presented.

On chapter four, the author's TO knowledge is expanded through a series of comparisons between well known benchmark examples and the author's numerical models' results. These comparisons provides the foundations to the software choice and topological optimization approach for the final structure. This chapter continues with the validation of this approach which is composed by the numerical model development, the experimental material's characterization, the structure's optimization and design cycle and by a final experimental activity to validate the results.

Following chapter's fourth approach, the final metal structure optimization and design process is developed in chapter five. Chapter six is the last chapter of this thesis where the final conclusions and some future suggestions are presented.

Chapter 2

Current solution

Active Space Technologies current solution is an aluminum part with 2175.81g that was produced with a Computer Numerical Control (CNC) machine. The structure has a L-shape geometry and it is linked to the hardware system by 3 carbon fiber tubes glued to aluminum inserts as shown in figure 2.1. For more detailed information about the structure's geometry, its technical drawing is in figure A.1 at appendix A.

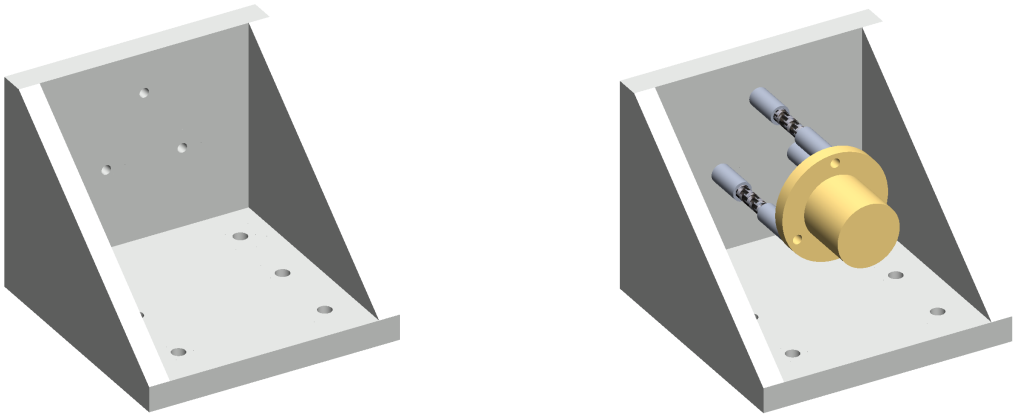

(a) L-shape. (b) L-shape assembly.

Figure 2.1: Current solution.

An analysis to the current L-shape solution shall be made in order to assess its performance and to better understand the problem. The objective of this is to know if this structure fulfills the company's requirements and how it compares with the optimized structure results.

This analysis will be performed with the Finite Element Method (FEM) technique which will be explained in section 2.1. This section is based on the work of Silvestre and Araújo [3], J. N. Reddy [4] and Moreira [5].

2.1 Finite Element Method

The finite element method is a numerical method that discretizes a continuous geometry (domain) in a mesh of elements (subdomain) with a finite size (figure 2.2). The reason to discretize a continuous ge-

ometry is to seek an approximate solution on the collection of the subdomains. It is easier to represent a complex function as a collection of simple polynomials than by an unique function. So, an approximation of the governing equation of each subdomain is done by any of the traditional variational methods to solve the differential equations that represent the physics of the problem.

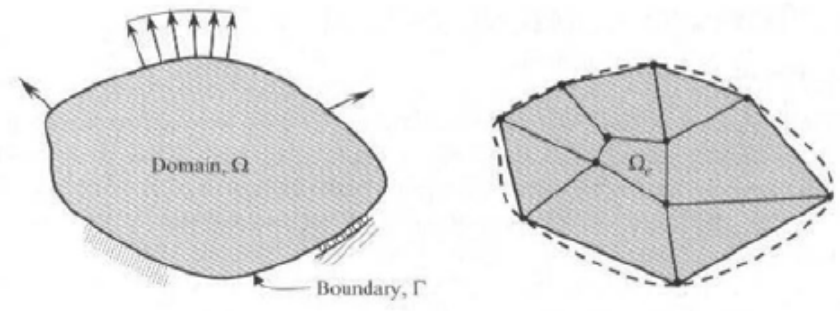

Figure 2.2: Representation of a discretized domain, [4].

The governing equations of each finite element are developed as well as the relations between different elements. These relations obey to compatibility conditions as equal displacement for a shared node. However, to determine the values in the borders between the nodes, interpolation functions are applied in a way that the boundary conditions are satisfied. For the discretized domain, the global system of equations can be found by assembling the equations of all the finite elements. This system of equations is expected to be solved when the boundary conditions of the problem are imposed and it is usually represented in a system of matrices form.

This method allows the study of very complex structures and it is a powerful tool in real world application problems. To better understand the method, reference [4] must be seen.

There are 6 different elements present in this thesis that will be briefly characterized. All the information about them is based on Altair Engineering [6], MSC Software [7] and Siemens [8].

2.1.1 1D elements - Rigid, CBAR and mass elements

The rigid elements create dependency (links) between the Degrees of Freedom (DoF) of the different nodes to avoid any change in the structure's stiffness matrix. If a structural element with significant higher mechanical properties values (when compared to the analyzed structure) is used instead of a rigid one, the stiffness matrix would have differences in the order of magnitude of its values which can lead to numerical problems or wrong results. Equation 2.1 relates the DoF of the rigid elements's mesh.

$$[G_i]\{u_i\} = 0 \tag{2.1}$$

This equation uses a linear relation so, rigid elements should only be used in analysis with small displacements. In this thesis, only the RBE2 element will be used although there is RBE3 element available too. Both should be very well understood since they have the same formulation, but they will create different results. The difference in the modelling of the dependent and independent nodes explain the different results.

A dependent node will have its displacement as a consequence of the independent node. So, depending on the used element, the independent(s) node(s) will control the dependent(s) node(s) displacement(s).

In the element RBE2, there is only one independent node and one or several dependent ones. This will allow the modelling of a rigid structure. The displacement of all the present nodes will be controlled by one node which will force all the nodes and elements to always have the same relative distance to that node. Although this element does not directly change the structure's stiffness matrix, it will artificially increase its stiffness since it constrains the dependent nodes displacements.

In the element RBE3, there is only one dependent node and one or more independent ones. This will allow a flexible structure model since the dependent node's displacement will be an average of the independent nodes' displacement. This enables a changing in the elements' length which will avoid an imposed stiffness by them. This element is typically used to transfer loads to the structure.

The reason to use only RBE2 will be further explained in the numerical model part in section 2.2.

The CBAR element available in Optistruct is a specific type of the CBEAM element and uses the formulation of a simple beam with constant properties along its length (symmetrical and constant cross-section) with 6 DoF per node. However, this element can only be used in closed sections since it assumes that its coordinates system's origin is coincident with the shear center of the cross-section (shear center and neutral axis coincide).

A mass element will be used to simulate the Center of Gravity (CoG) of the hardware system assembly. This element enables the user to simulate the presence of a mass in a point without a body. The type of mass element used is "CONM2" since it is a concentrated mass element with rigid body form that will not add any inertia properties – Non-structural mass.

2.1.2 2D elements - Shell elements

Shell elements are used when one dimension is significantly smaller when compared to the other two. This type of element enables good quality of results with less computational time when compared to 3D elements. These elements have 6 DoF in each node and they can use bilinear or biquadratic interpolation depending on the number of used nodes. Besides, shell elements can be formulated with one of two different theories: Kirchhoff-Love or Reissner-Mindlin. More information about the element type can be found on Silvestre and Araújo [3] and J. N. Reddy [4].

During this thesis, only rectangle elements with 4 nodes (bilinear interpolation) will be used in order to compare MSC Nastran SOL200 and Altair Optistruct with Matlab results. This element is known as "CQUAD4" element with a "PSHELL" property in both commercial softwares.

2.1.3 3D elements - Brick and tetrahedral elements

3D elements are used when the dimensional magnitude is similar in the 3 directions. These elements have 3 DoF in each node and they can use linear or quadratic interpolation depending on the number of nodes used.

Typically, in TO works, Tetrahedral (Tetra) elements are used because they are easier to adapt to complex geometries and the optimization is just to take out a design concept. However, in order to achieve an accurate result with a good balance with the computational cost, Brick (or Hex) and tetrahedral elements will be used in different sections of this work. Both the Brick (8 nodes) and Tetrahedral (4 nodes) elements use linear interpolation. These elements are used with "PSOLID" properties in both softwares.

It is of great importance to have a good mesh quality and there are 3 parameters of full importance to have into account. However, since 2D elements are only used in the 2D benchmark examples (section 4.1.1) and there are not complex geometries that could cause any problem with the mesh quality, the next parameters shown are already adapted to 3D elements:

- Mesh size:
  - More than one element along every structure's parts thickness is mandatory but at least 4 are recommended to achieve good accuracy;
  - Global or local mesh refinement until convergence is achieve in the variable of interest, e.g. displacement.
- Jacobian:
  - Measure of the element deviation from its ideal shape;
  - Acceptable values between 0.5 and 1 (ideal).
- Aspect ratio:
  - Ratio between the biggest and smallest edge length;
  - Acceptable values between 1(ideal) and 5.

2.1.4 Dynamic, Vibration and Static analysis

Using FEM, a dynamic analysis can be performed where the differential system of equations applied is represented by equation 2.2.

$$[M]\{\ddot{u}\} + [C]\{\dot{u}\} + [K]\{u\} = \{F\} \tag{2.2}$$

where $[M]$ is the mass matrix, $\{\ddot{u}\}$ is the nodal acceleration vector, $[C]$ is the damping matrix, $\{\dot{u}\}$ is the nodal velocity vector, $[K]$ is the stiffness matrix, $\{u\}$ is the nodal displacement vector and $\{F\}$ is the nodal forces vector.

For the final structure, a modal analysis will be performed. In order to get the undamped natural frequencies of a structure in free vibration, the modal structural finite element analysis is obtained from the Lagrange's equation 2.3.

$$\frac{d}{dt}\left(\frac{\partial T}{\partial \ddot{u}}\right) - \frac{\partial T}{\partial u} + \frac{\partial V}{\partial u} = 0 \tag{2.3}$$

where t is the time, T is the kinetic energy and V is the potential energy defined by equations 2.4a and 2.4b, respectively.

$$T = \frac{1}{2}\{\dot{u}\}^T[M]\{\dot{u}\} \tag{2.4a}$$

$$V = \frac{1}{2}\{u\}^T[K]\{u\} \tag{2.4b}$$

This originates the reduced system of equations shown by equation 2.5.

$$[M]\{\ddot{u}\} + [K]\{u\} = \{0\} \tag{2.5}$$

For free vibrations, a harmonic response is assumed in the form of equation 2.6.

$$\{u\} = \{\Phi\}\epsilon^{i\omega t} \tag{2.6}$$

Introducing equation 2.6 in 2.5, an eigenvalues problem is obtained and it is represented in equation 2.7. The eigenvalues correspond to the natural frequencies (ω_i) and the eigenvectors to the corresponding mode shapes ($\{\Phi\}^i$) obtained by solving the following eigenvalue/eigenvector problem (equation 2.7).

$$([K] - \omega_i^2[M])\{\Phi\}^i = \{0\} \tag{2.7}$$

A simpler analysis that comes from the dynamic analysis when the time dependency is not taken into account is the static analysis. Besides, this analysis can also be called linear static analysis if only small displacements are considered since a linear relation is used between the applied load and the system response. A linear static problem is solved through equation 2.8 where $[K]$ is the stiffness matrix, $\{u\}$ is the nodal displacement vector and $\{F\}$ is the nodal forces vector.

$$[K]\{u\} = \{F\} \tag{2.8}$$

2.1.5 Failure criterion

An accurate failure criterion is essential to correctly design any mechanical component. In applications where isotropic and ductile materials are used, it is common to use a yield criterion such as Von Mises. The distortion-energy theory predicts that yielding occurs when the distortion strain energy per unit volume reaches or exceeds the distortion strain energy per unit volume for yield in simple tension or compression of the same material, Budynas-Nisbett [9]. The critical distortional energy equation is defined in equation 2.9.

$$\frac{1}{2}[(\sigma_{11} - \sigma_{22})^2 + (\sigma_{22} - \sigma_{33})^2 + (\sigma_{33} - \sigma_{11})^2 + 6(\sigma_{23}^2 + \sigma_{31}^2 + \sigma_{12}^2)] = \sigma_{VM}^2 \tag{2.9}$$

However, for this thesis application, this criterion by itself is not enough to predict the failure of the mechanism since the target structure will be repeatedly used in test conditions characterized by high frequency loads which can cause a fatigue failure. Fatigue can be described as a continuous process with fluctuating stresses (dynamic loads) that even though these ones are smaller than the ultimate strength of the material, the failure of the mechanism will occur after a number of cycles in this loading conditions. The number of cycles to failure typically ranges from 10^3 to 10^7, Tinga [10].

2.1.6 Margin of Safety

The company follows ECSS-E-ST-32C Rev. 1 [11] standard from the European Cooperation for Space Standardization (ECSS) for all the engineering works. This is a standard for structural engineering in the mechanical field of space where for every part, a Margin of Safety (MoS) must be positive or at least, equal to zero. The margin of safety can be calculated through equation 2.10.

$$MoS = \frac{\sigma_{allowable}}{\sigma_{applied} \cdot FoS} - 1 \tag{2.10}$$

where $\sigma_{allowable}$ is the defined allowable stress limit, $\sigma_{applied}$ is the present stress and the FoS is the Factor of Safety defined by the same standard as 2 for yield strength and 3 for tensile strength.

2.2 L-shape numerical modelling

The model uses the same geometry as the L-shape shown before on figure 2.1 and its material is an Aluminum alloy 6082-T651 with the properties depicted in table 2.1.

Table 2.1: AL 6082-T651 properties.

ρ [Kg/m^3]	2700
E [GPa]	70
σ_y [MPa]	255
σ_{uts} [MPa]	300
$\sigma_{fatigue}$ [MPa]	95
ν	0.33

In this model, 4 types of elements are used as can be seen in figure 2.3: 3D Hex, 3D Tetra, CBAR and RBE2.

- 3D Hex element mesh is used in the interface structure part;
- 3D Tetra element mesh is used in the hardware structure part (figure 2.4a);
- CBAR to simulate the linkage tubes that connect the L-shape structure and the rigid body (figure 2.4a). This element is used to transfer the load between the hardware system and the structure. The usage of rigid elements for the tubes does not make sense since the tubes stiffness is in the same order of magnitude of the structure's stiffness;

- RBE2 instead of RBE3 to simulate the screws in the joints since the screws increase the stiffness in that part due to the pre-load. Moreover, they also distribute the force and moments equally along the washer's area (figure 2.4b). The washer's outside diameter is the double of the screw diameter.

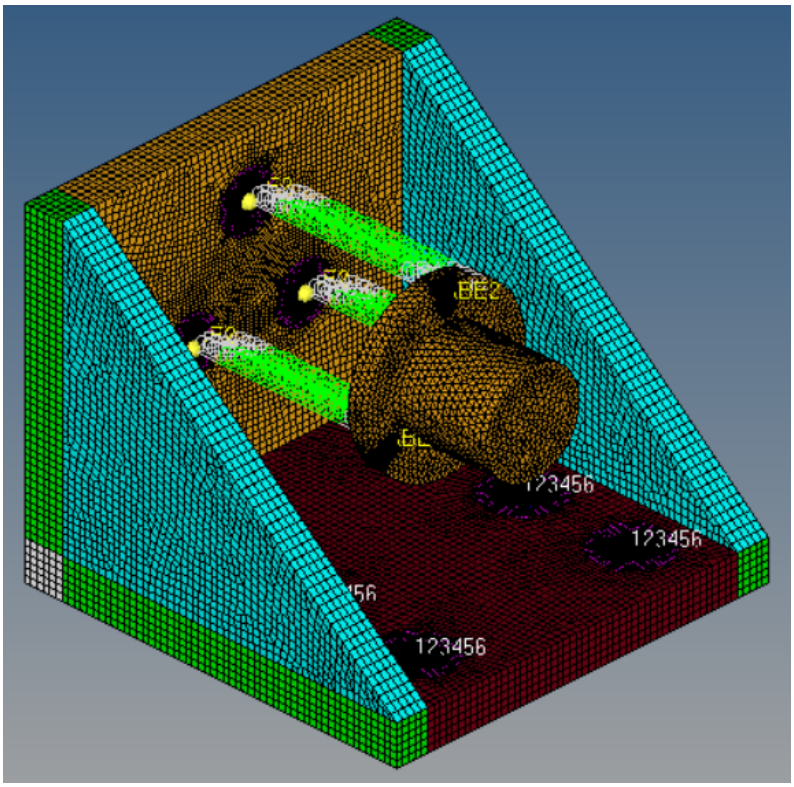

Figure 2.3: L-shape's assembly numerical model.

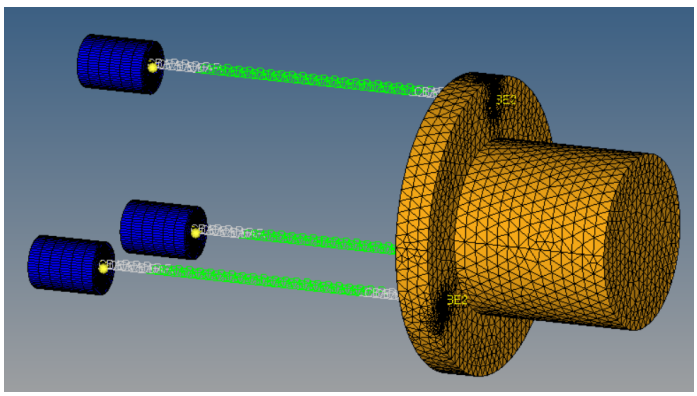

(a) Hardware system model.

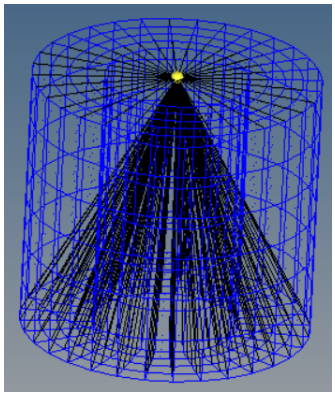

(b) Screw joint model.

Figure 2.4: Some of the model's parts.

To develop a model with good mesh quality and to keep mesh congruency and integrity, the structure was divided into several "subparts" as shown in figure 2.5.

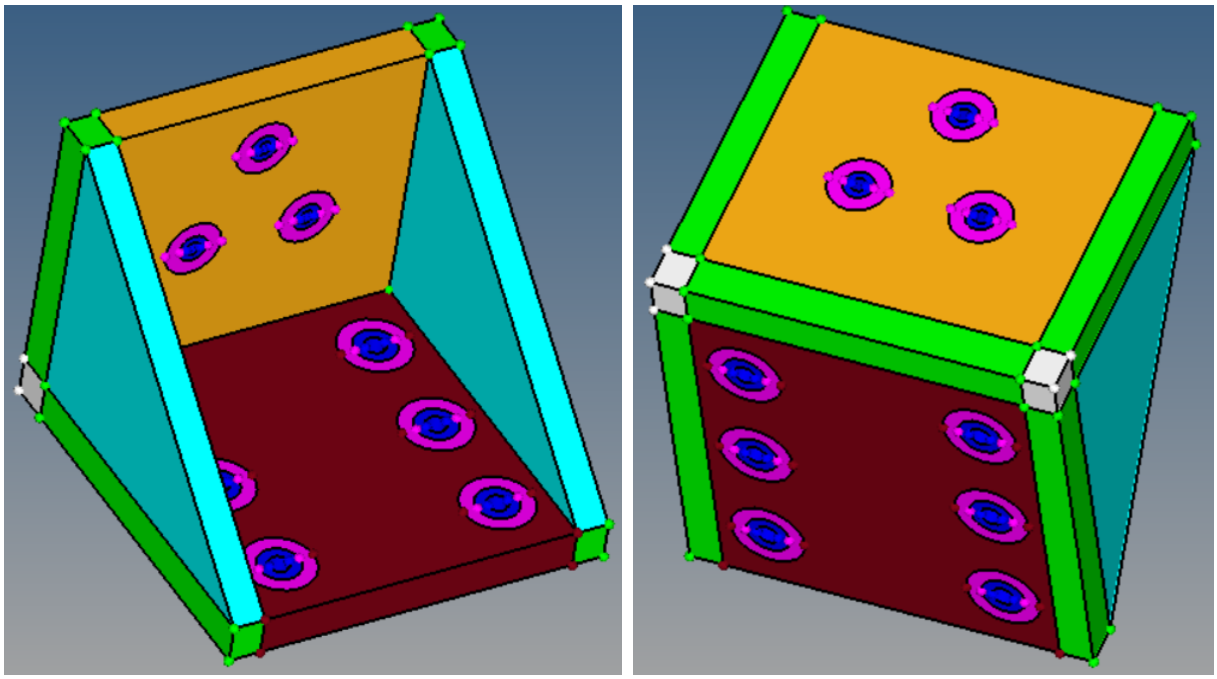

(a) (b)

Figure 2.5: L-shape in subparts.

In Finite Element Analysis (FEA), the mesh model and its quality are of extreme importance since it can largely influence the results. So, the mesh was developed with the following guidelines:

1. At least 4 elements along the washer's radial distance (blue part) and the transition area (purple part) to ensure accurate results in the joints which are potentially critical areas due to stress concentrations (figure 2.6a);

2. Ensure that the joints nodes are connected to the rest of the model (figure 2.6b);

3. Ensure the connection between the rest of the model nodes – between the several subparts (figure 2.7).

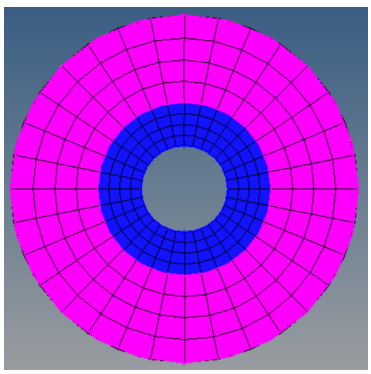

(a) Joint mesh with 4 elements along its radial distance.

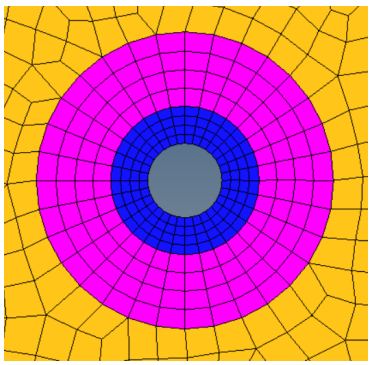

(b) Joint mesh with smooth transition to the rest of the model.

Figure 2.6: Joints 3D Hex mesh model.

(a) (b)

Figure 2.7: Nodes connections between several model's subparts.

Then, by trying to use the biggest element size as possible while the 3 points of the guideline and the quality criteria explained in section 2.1.3 are fulfilled, a global element size of 4mm was achieved as starting point. At this point, with a total of 30719 elements, the mesh quality characteristics are:

Joints:

- Nodes' density: 32 nodes per circle's edge;
- Worst jacobian: 0.87;
- Worst aspect ratio: 4.53.

The remaining of the mesh:

- Global element's size: 4mm;
- Worst jacobian: 0.42 in 72 of 18047 elements which is meaningless ($\approx$ 0.4%);
- Worst aspect ratio: 3.67.

Before any different analysis, a "Free-Free" modal analysis is performed to verify the model's mesh integrity. A "Free-Free" analysis means free constraints and free loads. Therefore, this analysis is done without the hardware system part and without any boundary condition. So, to validate the mesh connection between the nodes (mesh integrity), the results should present six, and only six rigid body modes with frequencies near 0.0Hz. If this does not happen is because the FEM model is not "fully" connected [12].

The eigenvalue problem can be solved in Optistruct using three algorithms where two of them can also be used for normal modes analysis: **Lanczos** or **AMSES**. Although **Lanczos** is slow for large problems, it will be the used method in this thesis since the problem is not large and the eigenvalues and associated mode shapes are calculated exactly while in **AMSES** they are approximated to be faster. Typically, **AMSES** is used over **Lanczos** when a large quantity of modes is necessary and not an accurate full shape as in an Noise, Vibration and Harshness (NVH) analysis. Detailed information about these methods can be found in [6].

The results from the "Free-Free" modal analysis are shown in table 2.2

Table 2.2: ”Free-Free” modal analysis to L-shape model results.

Modes	Results [Hz]
1st	2.6158e-4
2nd	2.6235e-4
3rd	2.7183e-4
4th	2.7506e-4
5th	2.8056e-4
6th	2.8073e-4
7th	1669.57

The first 6 frequencies are around zero and the author has verified in the animation mode the 3 translations and 3 rotations approximately. So, the mesh is validated in quality and integrity. Further on, a convergence analysis will be developed having always these two key points in mind.

For the boundary conditions, the structure has the 6 DoF fixed in the screws' heads nodes that fix the structure's base to the shaker (figure 2.8) and several load cases. One load case is related with the modal analysis while the other 8 are related with a static analysis. These 8 load cases have as base an inertial acceleration of 60G of magnitude in the 3 principal axis directions with the axis orientation combination as shown on table 2.3.

Table 2.3: Load cases orientation - combination matrix.

Load cases			
	x	**y**	**z**
1st load case	+	+	+
2nd load case	+	-	+
3rd load case	+	+	-
4th load case	+	-	-
5th load case	-	+	+
6th load case	-	-	+
7th load case	-	+	-
8th load case	-	-	-

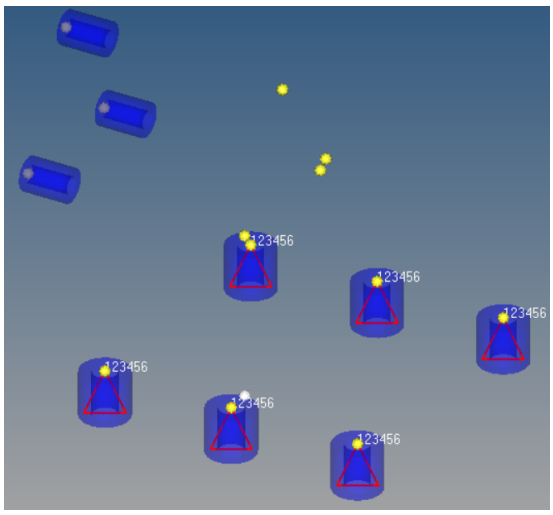

Figure 2.8: Structure's constraints.

2.3 Static and modal analysis

The FEM model with the initial mesh characteristics is shown in figure 2.3. As stated before, by using this model with different mesh sizes, a convergence analysis will be developed with the displacement and frequency values as variables of interest. The stress values will not be used since they are a consequence of the displacement. The initial mesh results are presented in table 2.4 and 2.5.

Table 2.4: Initial mesh static analysis results.

Load cases	Maximum displacement [mm]
1st	7.37e-03
2nd	1.02e-02
3rd	7.37e-03
4th	1.02e-02
5th	1.02e-02
6th	7.37e-03
7th	1.02e-02
8th	7.37e-03

Table 2.5: Initial mesh modal analysis results.

Modes	Frequency [Hz]
1st	553.75
2nd	606.41
3rd	2639.88

In order to see the evolution of the results, several analyses were done with the different mesh sizes shown in table 2.6. Besides, the mesh relative difference between the several meshes results is also shown in table 2.7. Although there are fluctuations in the results, it is possible to see that there are only slight differences which enables the use of any of them without significant accuracy loss. A balance between accuracy and the Central Process Unit (CPU) time cost should be made. So, the author will proceed with the mesh size number 2 for the current solution analysis and further optimization phase of this thesis since number 3 and 4 require too much computational time when compared to the others. This computational cost will be much higher during the optimization.

Table 2.6: Mesh sizes.

Size	Global element size [mm]	Node's density in joints	Total number of elements	CPU time [hh:mm:ss]
1	4	32	30 719	00:00:40
2	2	64	101 002	00:03:06
3	1.5	88	246 136	00:15:16
4	1.2	128	491 440	00:44:57

Table 2.7: Relative difference in the mesh convergence study with the smaller size as reference.

		1 to 2	2 to 3	3 to 4
Modal analysis: Frequency [Hz]	*1st Mode*	0.32%	0.67%	0.06%
	2nd Mode	0.43%	0.70%	0.31%
	3rd Mode	0.46%	0.81%	0.24%
Static analysis: Displacement [mm]	*1st Load case*	1.05%	1.31%	0.83%
	2nd Load case	0.78%	1.16%	0.19%
	3rd Load case	1.07%	1.00%	1.05%
	4th Load case	0.78%	1.06%	0.29%
	5th Load case	0.78%	1.06%	0.29%
	6th Load case	1.07%	1.00%	1.05%
	7th Load case	0.78%	1.16%	0.19%
	8th Load case	1.05%	1.31%	0.83%

The analysis results with the final mesh size are depicted in table 2.8 and 2.9 where it's possible to see that the displacement and stress results for the structure are equal for the symmetrical load cases as expected since the structure is also symmetric. Besides, the displacements are very small which justifies the linear static analysis. As expected, the frequency results obtained are also very low since the hardware system assembly is attached to the structure. By analyzing the L-shape structure alone with the same mesh and boundary conditions imposed, its first mode frequency value is 2423.14Hz which almost fulfills the minimum of 2500Hz. The L-shape's first mode shape can be seen in figure 2.9.

Table 2.8: Final L-shape mesh static analysis results.

Load cases	Maximum Displacement [mm]	Maximum stress [MPa]
1st	7.45e-03	11.59
2nd	1.02e-02	7.54
3rd	7.45e-03	11.58
4th	1.02e-02	7.61
5th	1.02e-02	7.61
6th	7.45e-03	11.58
7th	1.02e-02	7.54
8th	7.45e-03	11.59

Table 2.9: Final L-shape mesh modal analysis results.

Modes	Frequency [Hz]
1st	419.51
2nd	424.06
3rd	1808.14

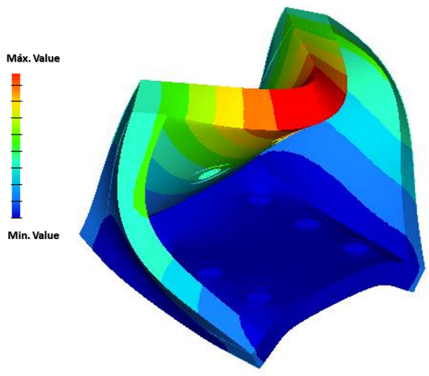

Figure 2.9: L-shape's first mode shape.

With a total of 101002 elements, the L-shape's final mesh quality characteristics are:
Joints:

- Nodes' density: 64 nodes per circle's edge;
- Worst jacobian: 0.77;
- Worst aspect ratio: 9.06 in 9216 of 40320 (≈2.86%) .

The remaining of the mesh:

- Global element's size: 2mm;
- Worst jacobian: 0.51;
- Worst aspect ratio: 5.45 in 36 of 60682 which is meaningless (≈0.06%).

The final mesh elements with the bad aspect ratio in the joints are the ones that are under the washer's interior half pressure area in the carbon tubes joints as shown with a grey color in figure 2.10. This happens because a very small element is present there to ensure a smooth transition and good quality along the plan while the 3D extrusion of the element complies with the global element size. This would result in a bad aspect ratio value by its definition as explained in section 2.1.3. However, the critical areas in terms of stress are the last ring of elements in the washer's area (outside blue one) and the rest of them along the purple area. It is normal that the elements that are closer to the transition between the washer's pressure and the rest of the model suffer more stress due to concentration factors. So, this bad value will be neglected since these elements always present very low stress values, as expected.

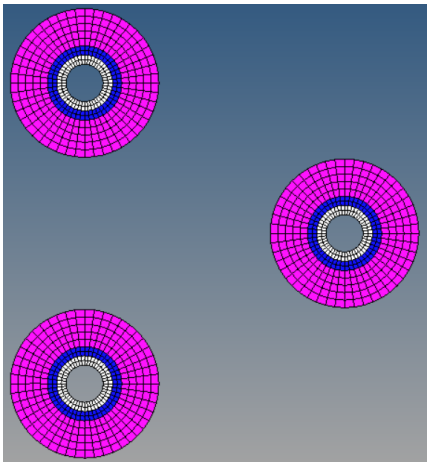

Figure 2.10: Elements with bad aspect ratio.

Using table 2.8 results and equation 2.10, table 2.10 presents the MoS of the L-shape structure. The results from this table show that the structure can be further optimized to achieve a MoS equal to 0 or some positive value near it. Besides, the large amounts of relatively unstressed material depicted in figure 2.11, indicates an inefficient use of the material which also induce the possibility of an optimization implementation to improve the design mass in a feasible domain. However, in terms of the first mode,

the frequency value is still not enough for the design requirements. This means that the TO needs to increase the stiffness of the structure while it should also increase the present stress values and reduce the structure's mass.

This analysis suggests that the active constraint during the TO will probably be the frequency value and not the stress value. This means that for the material choice, the stiffness will be more important than the strength. Another important thing to conclude is that the modelling of the bolt's pre-load is not necessary since the maximum stress value in that area is far below its limit.

Table 2.10: Final L-shape mesh static analysis results.

Load cases	MoS_y	$MoS_{fatigue}$
1st	10.00	3.1
2nd	15.91	5.3
3rd	10.01	3.1
4th	15.75	5.24
5th	15.75	5.24
6th	10.01	3.1
7th	15.91	5.3
8th	10	3.1

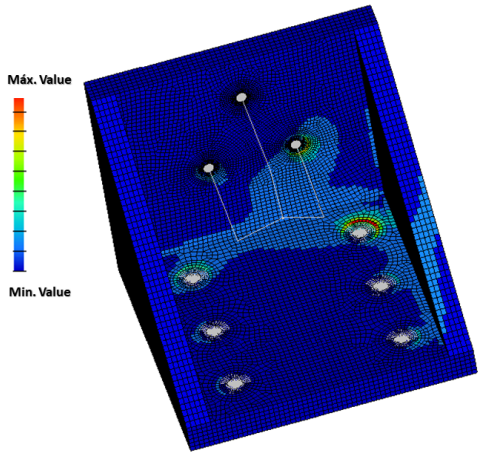

(a) 1st load case.

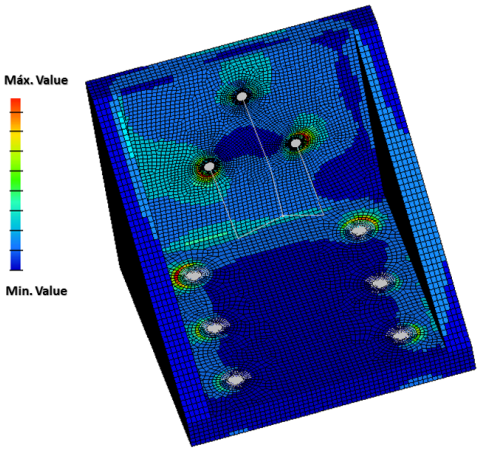

(b) 2nd load case.

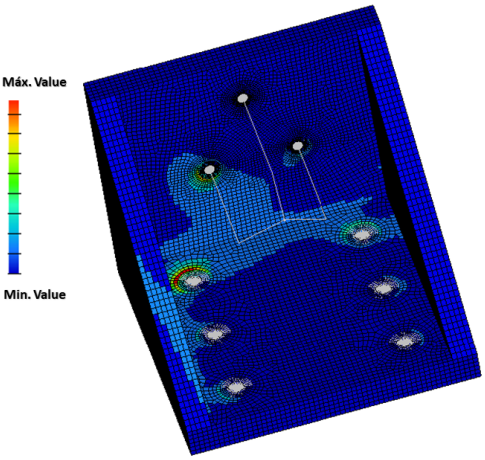

(c) 3rd load case.

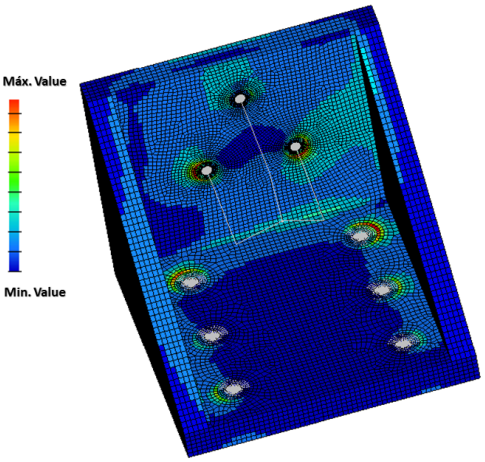

(d) 4th load case.

Figure 2.11: Stress values in the first 4 load cases of the static analysis - pictures without the hardware structure to facilitate the stress distribution visualization.

Chapter 3

Optimization and Additive Manufacturing fundamentals

3.1 Optimization

Optimization is a very useful tool in several phases of the development of a product in order to make it as good as possible. For structural purposes, this tool is usually used after the conceptual phase with the concept, objectives and constraints already defined. Structural optimization techniques are very well studied in the literature, such as Christensen and Klarbring [13] and Rao [14] and a structural optimization problem can be generally formulated as 3.1.

$$
\begin{aligned}
&\text{Find x to minimize} \\
&\text{F(x) is the objective function subject to :} \\
&g_j(x) \leq 0, \quad j = 1, ..., n_g \qquad \text{inequality constraint} \\
&h_k(x) = 0, \quad k = 1, ..., n_h \qquad \text{equality constraint} \\
&x_i^L \leq x_i \leq x_i^U, \quad i = 1, ..., n \qquad \text{side constraint} \\
&x = \{x_1, x_2, ...x_n\} \qquad \text{design variables}
\end{aligned}
\tag{3.1}
$$

Structural optimization can be classified in 3 categories, i.e. size, shape and topology optimization, Christensen and Klarbring [13] and Johnson et al. [15].

- **Size** - The optimal design is found by changing the size variables such as the cross-sectional dimensions of trusses and frames, or the thicknesses of plates. This is the easiest and earliest approach to improve structural performance. A size optimization problem for a truss structure is shown in figure 3.1a.
- **Shape** - The optimum design is mainly performed on continuum structures by modifying the predetermined boundaries to achieve optimal designs. For example, for a truss, the location of

nodes is defined as design variables. A shape optimization problem for a truss structure is shown in figure 3.1b.

- **Topology** - The optimum design is mainly performed on continuum structures by manipulating the material's distribution in the design region. This is by far the most challenging technically and at the same time the most rewarding one. A TO problem for a truss structure is shown in figure 3.1c.

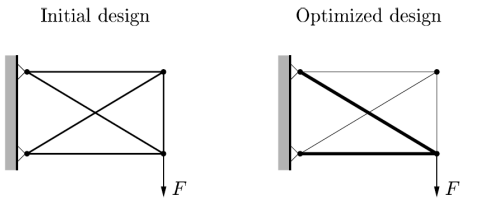

(a) A size optimization problem formulated by optimizing the cross-section.

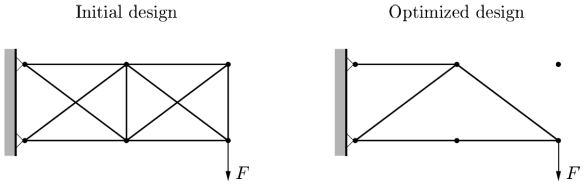

(b) A shape optimization problem formulated by optimizing the location of the trusses' nodes.

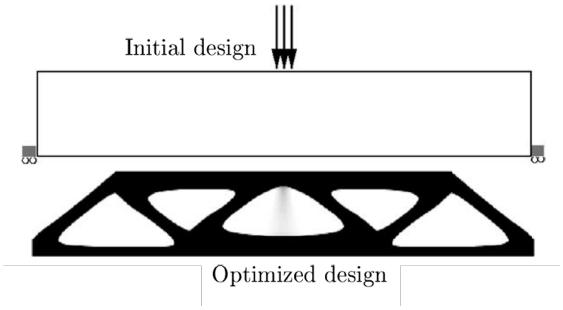

(c) A TO problem formulated by optimizing the location of the trusses' material.

Figure 3.1: Structural optimization categories examples, adapted from [13].

Topology optimization intends to find an optimal structural configuration within a given design domain for specified objectives, constraints, boundary conditions and loads where its biggest advantage over sizing or shape optimizations lies in the fact that no specified initial structural topology needs to be presumed. Due to this key advantage, TO had remarkable developments over the last decades in both theoretical studies and practical applications in several industries, [16–20]. Although the first paper on TO was published over a century ago by Michell [1] who derived optimality criteria for the least weight layout of trusses, the significant landmark for TO was in 1988 with the work of Bendsøe and Kikuchi [21]. In this work, the homogenization-based approach was proposed where an optimization is done to the global performance in terms of density variables which are linked to a specified micro-structure model at a separated lower scale, as shown in figure 3.2.

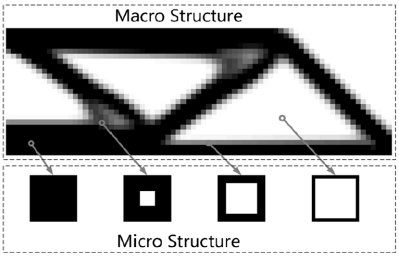

Figure 3.2: Topology optimization using homogenized micro-structures, [22].

The mathematical complexity of the homogenization approach does not allow a widespread application. Soon after the homogenization approach, Bendsøe [23] proposed another density-based approach with a significant simplified assumption. Instead of homogenization, it proceeds by penalizing exponentially isotropic material in terms of element density variables with a power law scheme that helps to avoid grey solutions. This approach is also known as Solid Isotropic Material with Penalty (SIMP) [24, 25] and it has become the most popular and successful method in TO due to its simplicity in both conception and numerical implementation [18, 26].

Another popular approach, named Evolutionary Structural Optimization (ESO), was developed by Xie and Steven [26] based on a heuristic element removal strategy. For its conceptual simplicity, the ESO method was well accepted and developed for various mechanical design problems [27]. However, despite its popularity, the ESO-type methods were also largely argued [28] and criticized [29] mainly because the method lacks a restitution mechanism for the removed elements, which may lead to failures in designs. To correct these deficiencies, later on, bi-directional ESO (BESO) [30, 31] and soft killing BESO versions [18, 32] were developed, which allow both material removal and addition. It has been demonstrated that the latest version of ESO method [32] is capable of circumventing all previously raised unsatisfactory issues. ESO-type methods have shown a robust and efficient performance in material micro-structural designs as compared to SIMP method [33–35]. Moreover, the discrete nature of ESO-type methods makes it also preferable in multi-scale structural designs [36, 37]. Sigmund [38], suggested to categorize ESO-type methods as the discrete form of density-based approach for its similarities with SIMP method.

Both continuous and discontinuous density-based approaches have numerical difficulties such as mesh dependency, checkerboard patterns, and local minima [17]. The checkerboard pattern is due to the finite element approximation or design optimization criteria [39]. To mitigate these numerical instabilities, Sigmund and Petersson [40] proposed the so-called sensitivity filtering scheme by smoothing the sensitivity of the chosen element and its neighbouring element sensitivities. Later on, Bruns and Tortorelli [41] proposed a density filtering scheme to improve the reliability and convergence of the optimization, where the filtering is performed on element densities rather than sensitivities. Sigmund [38] further improved the density filter by introducing a new class of morphology-based restriction schemes. Jang et al. [42] presented that using non-conforming four-node finite elements can completely suppress the checkerboard patterns, because the stiffness of the non-conforming element exhibits correct limiting behaviour. Haber et al. [43] proposed the perimeter control method to control the checkerboard pattern and some complex structures between solid and void elements. Zhang and Duysinx [44] also proposed a quadratic form of the improved perimeter control with the dual approach. Some detailed discussions of checkerboard control in the framework of ESO/BESO can be found in [45, 46]. With these technical achievements, topology optimization has become one of the most active topics in numerical computational optimization.

Apart from density-based approaches, there exist several alternative approaches such as the bubble method [47], topological derivative [48], level-set method [49–51] and phase filed method [52]. Among which, level-set method, describing structural topology as the level-set of a higher dimensional function

which has attracted quite a lot of research attention in the recent years [53]. Despite its distinct advantage in representing complex geometries, there's however still a long way before reaching the stage of regular industrial applications [54].

3.2 Additive manufacturing

Referred to in short as AM, the principle of this technology is that a model, initially generated using a three-dimensional Computer-Aided Design (3D CAD) system, can be fabricated almost directly by layers of material that when added to each other, a 3D printed part is created [55]. American Society for Testing and Materials (ASTM) had formed in 2009 the ASTM F-42 committee in order to standardize AM technologies [56]. According to their first standard, [57], AM is defined as:

"The process of joining materials to make objects from 3D model data, usually layer upon layer, as opposed to subtractive manufacturing technologies."

Obviously, in the physical world, each layer must have a finite thickness and so, the resulting part will be an approximation of the original data, as illustrated by figure 3.3. The thinner each layer is, the closer the final part will be to the original model.

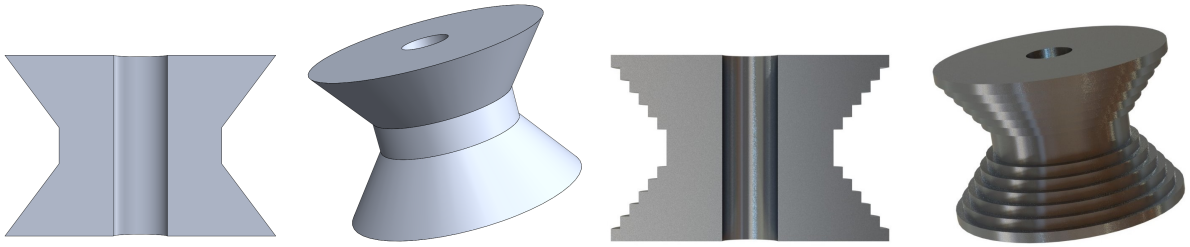

(a) CAD model cross section. (b) CAD model 3D view. (c) Real part cross section. (d) Real part 3D view.

Figure 3.3: CAD model VS Real part.

There are many related terms used to describe AM and common synonyms related with the evolving states of this technology through the years since initially only prototypes could be developed with this technology while now, final use structures can also be built. Some of these terms include [55, 58, 59]: Rapid prototyping, rapid manufacturing, layered manufacturing, additive fabrication, additive layer manufacturing, additive techniques, additive processes, additive manufacturing, free form fabrication and 3D printing.

3.2.1 Benefits of AM

AM technology significantly simplifies the process of producing complex 3D objects directly from CAD data when compared with other typical manufacturing processes that require a careful and detailed analysis of the part geometry to determine things like the order in which different features can be fabricated, what tools and processes must be used, and what additional fixtures may be required to complete the

part. In contrast, AM only needs some basic dimensional details and a small amount of understanding about how the AM machine works and the materials that are used to build the part which can significantly increase the process chain speed. The typical AM steps from the virtual CAD description to the physical resultant part are summarized in figure 3.4. However, for metals, this process requires a deeper knowledge from AM technologies by the user when compared to polymers or ceramics. The significant changes are in the post-processing phase and some of its typical extra steps are:

- Thermal treatment to relief residual stresses and uniformize the grains;
- Separation between parts and build plan;
- Machining and surface finishing with sandblasting.

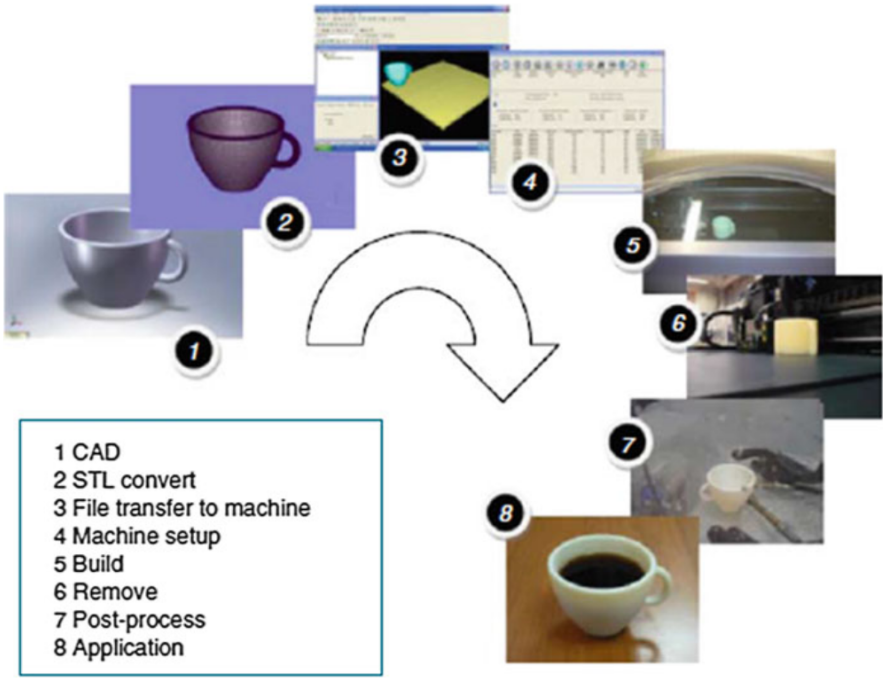

Figure 3.4: AM process flow, [55].

It is possible to build almost any shape which enables geometry optimization without constraints in complex geometries. This will produce lighter structures which is equivalent to less fuel consumption in industries as aircraft and automotive, for instance. In terms of material, since it is not a subtractive method, the waste is significantly lower when compared to other processes thus supporting green manufacturing. Besides, materials can be processed one point, or one layer at a time, enabling the manufacture of parts with complex material compositions and designed property gradients as well as fully functional assemblies and mechanisms.

The lower waste of material and the possibility to produce very complex geometries, composite structures and assemblies and mechanisms products without an increase in the production cost, makes AM technologies also very attractive in terms of economics.

3.2.2 Seven categories of AM processes

Although ASTM only recognizes six processes as AM technologies: Material extrusion, Vat photopolymerization, Material jetting, Binder jetting, Powder Bed Fusion (PBF) and Direct Energy Deposition (DED) [60], among the scientific community, there are seven recognized. The seventh one is Sheet lamination which is a hybrid process.

The rest of this section, 3.2.2, is based on the work of Gibson et al. [55], Loughborough University [61], Wong and Hernandez [62] and Vaneker [58] and consists of a brief introduction to the seven categories of AM processes.

Material Extrusion

Material extrusion technologies (figure 3.5) are characterized by using a reservoir with material that is forced out through a nozzle when pressure is applied. The material that is being extruded must be in a semi-solid state when it comes out of the nozzle. This material must fully solidify while remaining in that shape. Furthermore, the material must bond to material that has already been extruded so that a solid structure can result.

Only polymers can be used in this process, but some machines are capable of using two different kinds at the same time, so the support material can be different of the structural one and easier to take off in the end.

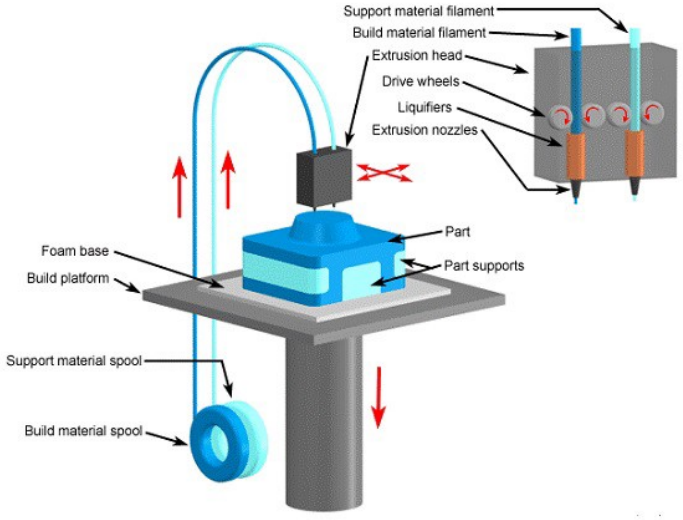

Figure 3.5: Example of a material extrusion schematics, [58].

Vat Photopolymerization

Photopolymerization processes (figure 3.6) make use of liquid, radiation-curable resins, or photopolymers, as their primary materials. Most photopolymers react to radiation in the ultraviolet (UV) range of wavelengths, but some visible light systems are used as well. Upon irradiation, these materials undergo a chemical reaction to become solid. This reaction is called photopolymerization, and is typically com-

plex, involving many chemical participants. Several types of radiation may be used to cure commercial photopolymers, including gamma rays, X-rays, electron beams, UV, and in some cases, visible light.

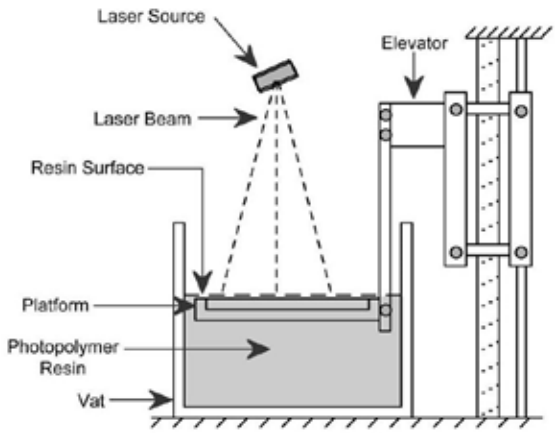

Figure 3.6: Example of a vat photopolymerization schematics, [58].

Material Jetting

Material Jetting process (figure 3.7) is very similar to a 2D ink jet printer. The inkjet head moves along the platform, depositing a photopolymer (with or without support material) which is cured by a UV lamp after each layer is finished.

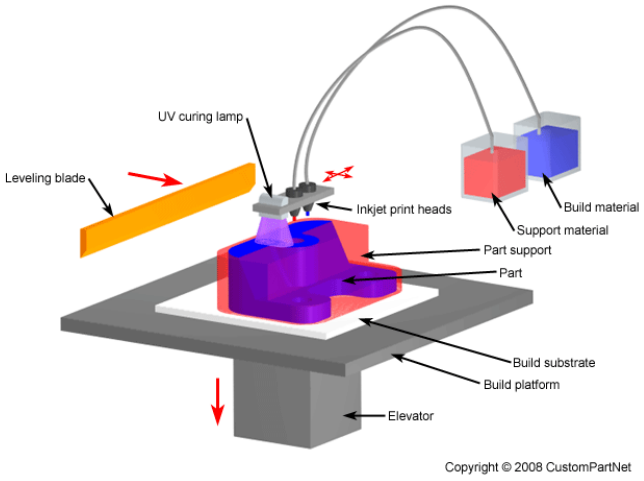

Figure 3.7: Example of a material jetting schematics, [58].

Binder Jetting

Binder jetting methods (figure 3.8) were developed in the early 1990s, primarily at Massachusetts Institute of Technology (MIT). They developed what they called the 3D Printing (3DP) process in which a binder is printed onto a powder bed to form cross sections. This concept can be contrasted with PBF, where a laser melts powder particles to define a cross section. A wide range of polymer composite,

metals, and ceramic materials have been demonstrated, but only a subset of these are commercially available. Some binder jetting machines contain nozzles that print color, not binder, enabling the fabrication of parts with many colors. Several companies licensed the 3DP technology from MIT and became successful machine developers, including ExOne and ZCorp (purchased by 3D Systems in 2011). A novel continuous printing technology was being developed recently by Voxeljet that can, in principle, fabricate parts of unlimited length.

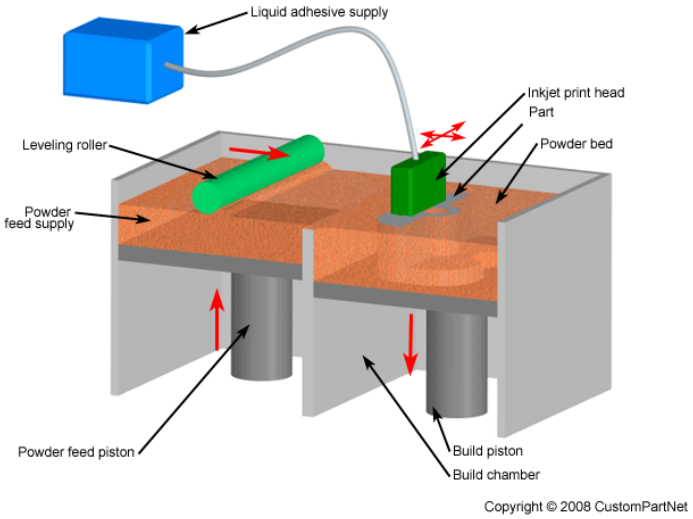

Figure 3.8: Example of binder jetting schematics, [58].

Sheet Lamination

One of the first commercialized (1991) additive manufacturing techniques was Laminated Object Manufacturing (LOM). LOM involved layer-by-layer lamination of paper material sheets that are cut with a CO_2 laser. Each sheet represent one cross- sectional layer of the CAD model of the part. In LOM, the portion of the paper sheet which is not contained within the final part is sliced into cubes of material using a crosshatch cutting operation. A schematic of the LOM process can be seen in figure 3.9.

Ultrasonic Additive Manufacturing (UAM), also known as Ultrasonic Consolidation (UC), is a hybrid sheet lamination process combining ultrasonic metal seam welding and Computer Numerical Control (CNC) milling. This process was commercialized by Solidica Inc. (USA) in 2000, and subsequently licensed to Fabrisonics (USA). In UAM, the object is built up on a rigidly held base plate bolted onto a heated platen, with temperatures ranging from room temperature to approximately 200^o C. Parts are built from bottom to top, and each layer is composed of several metal foils laid side by side and then trimmed using CNC milling. During UAM, a rotating sonotrode travels along the length of a thin metal foil. The foil is held closely in contact with the base plate or previous layer by applying a normal force via the rotating sonotrode, as shown schematically in figure 3.10. After depositing a foil, another foil is deposited adjacent to it.

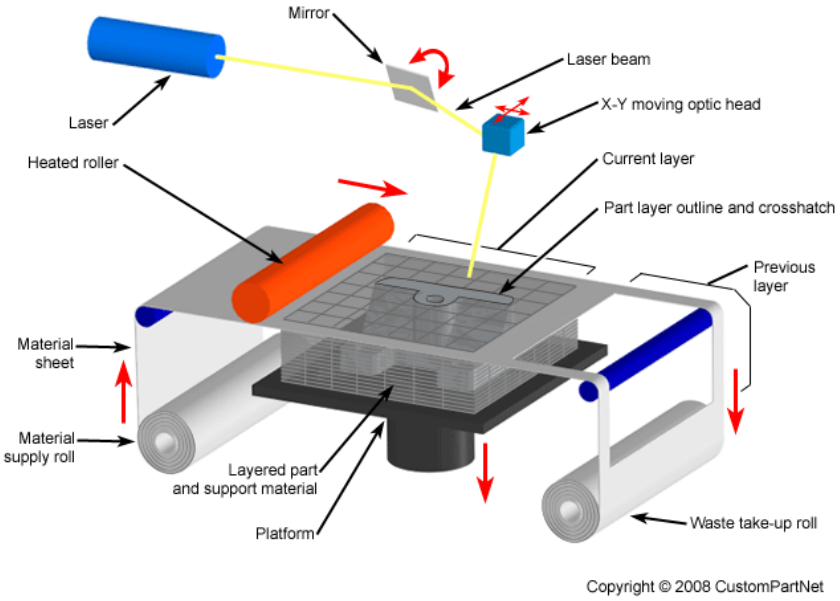

Figure 3.9: Example of LOM schematics, [55].

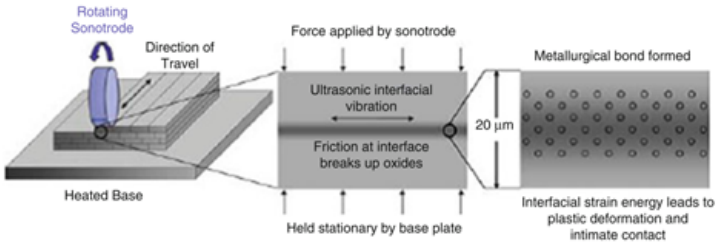

Figure 3.10: Example of UAM schematics, [55].

Directed Energy Deposition

DED processes (figure 3.11) enable the creation of parts by melting material as it is being deposited. This makes metals that are easy to weld an option to this process. This processes direct energy into a narrow, focused region to heat a substrate, melting the substrate and simultaneously melting the material that is being deposited into the substrate's melt pool. DED processes include the use of a laser or electron beam to melt powders or wires.

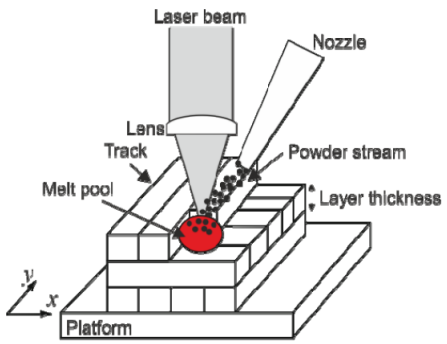

Figure 3.11: Example of DED schematics, [58].

Powder Bed Fusion

PBF processes were among the first commercialized AM processes. Developed at the University of Texas at Austin, USA, Selective Laser Sintering (SLS) was the first commercialized PBF process. Its basic method of operation is schematically shown in figure figure 3.12 and all other PBF processes modify this basic approach in one or more ways to enhance machine productivity, enable different materials to be processed, and/or to avoid specific patented features.

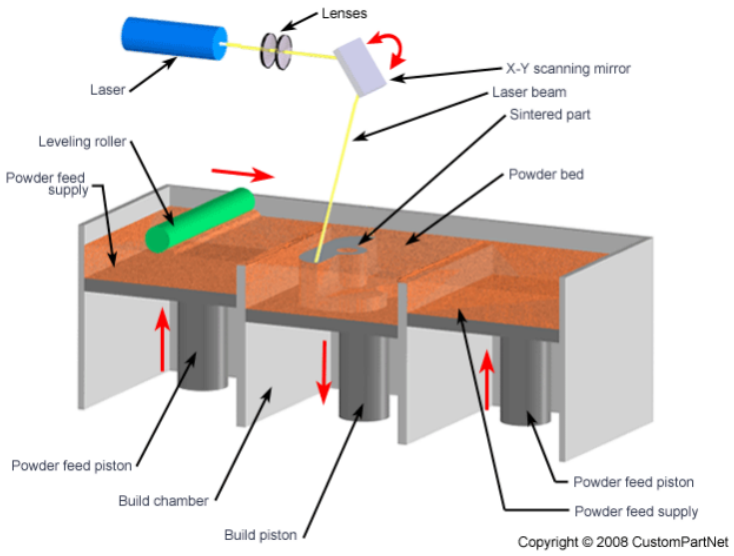

Figure 3.12: Example of PBF schematics, [58].

All PBF processes share a basic set of characteristics. These include one or more thermal sources for inducing fusion between powder particles, a method for controlling powder fusion to a prescribed region of each layer and mechanisms for adding and smoothing powder layers. PBF processes were originally developed to produce plastic prototypes using a point-wise laser scanning technique where only lasers were used as thermal source. Nowadays, although lasers are mostly used, additional thermal sources like electron beam were developed. This process was developed at Chalmers University of Technology, Sweden, and was commercialized by Arcam AB, Sweden, in 2001. As a result, PBF processes are widely used worldwide, have a broad range of materials including polymers, metals, ceramics and composites which can be used and are increasingly being used for direct manufacturing of end-use products, as the material properties are comparable to many engineering-grade polymers, metals, and ceramics.

The most common PBF methods are: Direct Metal Laser Sintering (DMLS), Electron Beam Melting (EBM), Selective Laser Melting (SLM) and SLS. EBM uses an electron beam to perform the melting and requires vacuum. It uses metals and alloys to make functional parts. One of the future uses of this technique may be the application in space since it requires vacuum environment. SLS and SLM use the same process with just one difference. While SLS as the name suggest, uses a sintering technique, the other as the name also suggests, completely melt the material. Besides, the difference between DMLS and SLS is that DMLS uses metals and alloys while SLS uses polymers and ceramics.

3.2.3 AM in aerospace industry

The aerospace industry started to use AM since the very beginning of this technology. Due to the high amount of money available they were able to go for the most advanced technology with the best machines and process settings. However, even with all the available budget, AM is still a relatively new technology under development in order to produce parts with good quality in a consistent way [63]. The main problem is that the processes are not yet fully matured since many variables are involved. According to the Federal Aviation Administration (FAA) [64] more than 150 variables may need to be controlled for a given AM machine to produce stable and repeatable parts. The official report from FAA specifically mention that it presents a risk to the aerospace industry due to the lack of adequate standards. Also, a big problem is the lack of cooperation. Since the testing of materials and machines is very expensive, companies keep the results for themselves. A specialist on AM affirms that some of the leading aerospace companies have done extensive research, and they have extensive data about the heating and cooling rates and how the structure is formed, but since this information is expensive to obtain, it is not shared [65].

In order to help the industries improving their knowledge in a quicker way and to create standards suitable for everyone, ASTM is using 8 committees (F07, F39, E07, F44, F04, B09, D20 and F38) to help the AM technologies specialized committee (F-42) in their activity. Additionally, since 2011, a Partner Standards Developing Organization (PSDO) agreement between ASTM international and the International Organization for Standardization (ISO) is taking place where the biggest synergy is between F-42 and TC 261 (ISO's committee specialized in AM technologies). These two organizations are also working in close cooperation with European Committee for Standardization (CEN) with several plans and activities to improve AM technologies [60].

PSDO work already created 5 active standards and they also have 14 under development where CEN also took part in 3 of the active ones [66, 67]. Besides the 5 previously mentioned, ASTM has 2 active standards and 7 waiting for approval for testing activities, 3 waiting for approval for design purposes, 11 active and 9 waiting for approval in the Materials and Processes fields and 1 waiting for approval on Environment, Health and Safety fields [63, 68]. ISO also has 3 active standards of their own [66, 67].

Benefits of AM in aerospace industry

AM has presented many advantages for the aerospace industry, one of the biggest ones is saving weight, as this is a major concern since all the weight of the structure needs to be lifted. This weight saving can be achieved using complex geometries that are not achievable, or far more expensive to produce using conventional methods. One example of weight saving that was demonstrated by General Electric (GE) in the design of their fuel nozzle, is the capability of combining many parts in one, reducing assembly and integration issues. GE claims that their fuel nozzle has combined 20 parts into a single unit (figure 3.13a) that weight 25% less than an ordinary nozzle and is five times more durable [69]. Another way to save weight is through the use of TO which produces complex geometrical parts if used to its full potential. One example of TO for AM is a nacelle hinge bracket from an Airbus A320. By optimizing the

part, it was possible to reduce the mass from 918g to 326g which represents a 64% mass reduction. The optimized design retained the same characteristics in terms of stiffness and bolt loading, while reducing the stresses on the part. The figure 3.13b shows the part before and after optimization [70, 71].

Aerospace parts can have a bad buy to fly ratio, sometimes 95% of the material is wasted due to a lot of machining, known as subtractive manufacturing. Since in AM, the material is deposited where it is needed, a much better buy to fly ratio is possible to be achieved. Another great advantage of AM for this industry in the economical field is that there is no difference in the cost of a part production if a company produces 10000 or 1 part. This has a significant impact since, for instance, the production of only 1 unit of each part is common for satellites structures.

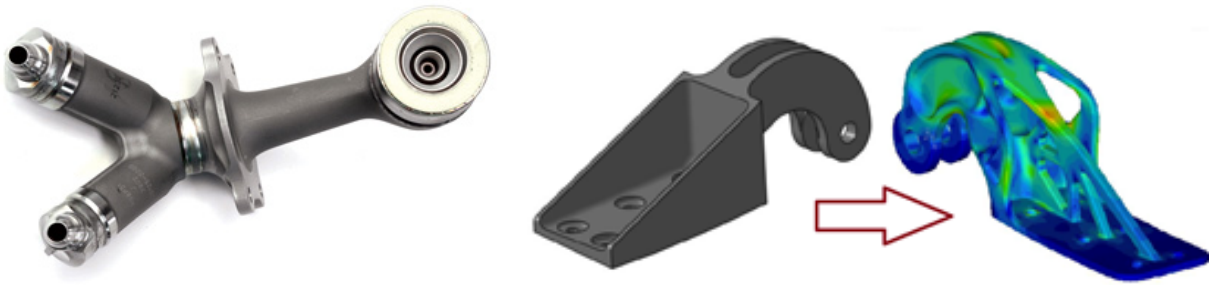

(a) GE printed fuel nozzle, [69].

(b) Original and topological optimized A320 hinge, adapted from [70].

Figure 3.13: Examples of successful application of AM in aerospace industry.

3.2.4 Topology Optimization and Additive Manufacturing

As stated before, it is possible to achieve significant savings in weight using TO at its fullest. Although it is hard to reproduce such a complex geometry as shown in figure 3.13 or even worse geometries with conventional methods, it is much simpler with AM technologies. The recent developments in AM enables the potential of TO to be further used, turning this in a perfect combination. This will allow the production of very complex structures without wasting material and without increasing the number of necessary steps until the final product which usually is very time consuming and expensive. In fact, sometimes the cost can decrease with the increasing of the complexity due to reduced support structure requirements. As pointed out in a paper by Sigmund [72], optimal stiffness design favours very fine micro-structure, which is inherently very complex.

Since AM allows the full exploration of TO, there is no reason to use sub-optimal components due to manufacturing constraints as before, but this will lead to some difficulties when TO is being implemented. The optimum topology can only be determined if the mesh allows the representation of it. It is well known that as the mesh is refined, a different and more detailed problem emerges, and the optimality of the topology change (typically improves). For topology optimization, it is usual for each finite element within the design domain to be defined as a design variable, allowing a variation in its density, for instance, in the case of SIMP. The minimum feature sizes commonly achievable with AM means that a very high number of design variables are needed to represent the topology of maximum complexity. Currently, this is prohibitive to achieve a non-sub-optimal solution although these are better than the ones obtained with

conventional manufacturing processes. So, it is no longer the manufacturing stage that is the limiting factor in the realization of optimal designs in terms of topology complexity and detail, it is the design stage [73]. There are several actions being developed to solve this problem where the most researched approach is an iterative re-meshing thereby only refining where required and coarsening where a fine mesh is no longer needed. Several implementations of this approach in 2D and 3D can be found in the literature [74–82].

Even though the AM technologies produce good structural components and have less constraints than conventional methods, they still have some restrictions that should be considered during the design and production of the structure. During the design phase, special considerations should be taken with overhanging structures, small and fragile details, long and narrow channels, internal cavities, removal of supports or machining access in post processing (if applicable), small holes, minimal clearance, build accuracy, surface finish and material's mechanical properties, specially in z-direction (direction perpendicular to the plane of material addition) [55, 58].

Some of these problems can be solved with methods that were not develop for AM but can be adapted. An example of this is the minimum member thickness constraint [83–85] which is applicable to the minimum feature size constraint for the AM processes. This constraint is commonly found in commercial software such as Optistruct by Altair Engineering [85] and Nastran by MSC Software [86]. Some research has been conducted to implement methods that can improve TO for AM. For instance, Brackett et al. [73] tries to develop a method to avoid the necessity of support structures through the manipulation of the relation between the angle of the two edges/faces and the horizontal distance of the upper edge/face in order to self-support itself.

3.3 Topological Optimization with SIMP approach

This section is based on the work of Bendsøe and Sigmund [17], Sigmund [28, 87], Andreassen et al. [88], Liu and Tovar [89] and Fernandes [90] and explain the basic essential technical knowledge about TO that will be used in this thesis.

The SIMP method is based on an equivalent element Young's modulus (E_e) as function of the relative element density (x_e) and the solid material Young's modulus (E_0). This function is given by equation 3.2.

$$E_e(x_e) = x_e^p E_0, \quad 0 < x_{min} \leq x_e \leq 1 \tag{3.2}$$

where p is a penalization power that should be higher than 1, usually 3 ($1< p <7$). x_{min} is the relative element density of the void material, which is higher than zero to avoid singularity of the finite element stiffness matrix, that occurs if all material is removed. So, a hole is represented by elements with density of x_{min} or near.

A modified SIMP approach given by equation 3.3 can be used where Young's modulus of the "void" or weak material is defined as E_{min}. This is a non-zero value to avoid singularity of the finite element stiffness matrix as explained before.

$$E_e(x_e) = E_{min} + x_e^p(E_0 - E_{min}), \quad x_e \in [0, 1] \tag{3.3}$$

Using the finite element analysis theory, the global stiffness matrix (K) is defined by equation 3.4a and the element stiffness matrix (K_e) defined by equation 3.4b.

$$K(x) = \sum_{e=1}^{N} K_e(x_e) \tag{3.4a}$$

$$K_e(x_e) = E_e(x_e)k_e^0 \tag{3.4b}$$

where k_e^0 is the element stiffness matrix for an element with an unitary Young's modulus, which implies that this matrix is independent of the elastic modulus, and therefore independent of x_e. The k_e^0 matrix depends on the element type and the Poisson's ratio (ν).

Optimization problem formulation

There are two topology optimization problems in this work. Firstly, the minimum compliance problem that minimizes the structure's deformation and secondly, the minimum mass problem that minimizes the structure's mass. Both are solved under the prescribed constraints, loading and boundary conditions where the objective is to find the design variables, i.e. the density distribution (x) that satisfies the problem conditions.

The compliance ($C(x)$) can be defined as in equation 3.5a, obtained by the inverse of the stiffness ($K(x)$) while the mass ($M(x)$) can be defined as in equation 3.5b, obtained through the product of the material's density vector ($\rho(x)$) and the structure's available volume vector ($V(x)$).

$$C(x) = F^T U(x) \tag{3.5a}$$

$$M(x) = \rho(x)V(x) \tag{3.5b}$$

where F is the vector of nodal force and $U(x)$ is the vector of nodal displacement. Problem formulation 3.6a and 3.6b shows the minimum compliance problem and minimum mass problem formulations, respectively, for the non-modified SIMP approach.

$$Min: \ C(x) = F^T U(x)$$

$$Subject\ to: \begin{cases} \frac{V(x)}{V_0} = f, & equality\ constraint \\ F = K(x)U(x), & state\ equation \\ 0 < x_{min} \leq x_e \leq 1, & side\ constraint \end{cases} \tag{3.6a}$$

$$Min:\ M(x) = \rho(x)V(x)$$

$$Subject\ to: \begin{cases} \sigma_{VM-applied} - \sigma_{VM-max} \leq 0, & inequality\ constraint \\ req.freq. - pres.\ freq. \leq 0, & inequality\ constraint \\ 0 < x_{min} \leq x_e \leq 1, & side\ constraint \end{cases} \tag{3.6b}$$

where V_0 is the volume of the design domain and f is the prescribed volume fraction. $F = K(x)U(x)$ is the state equation, but numerically it can be more efficient to use $C(x) = F^T U(x)$. The $\sigma_{VM-applied}$ is the present Von Mises stress in the structure while σ_{VM-max} is the maximum allowable Von Mises stress. The $req.freq.$ is the required minimum frequency for the first mode and $pres.freq.$ is the present frequency.

By developing the compliance equation with the definition of nodal force, equation 3.7 is obtained.

$$C(x) = F^T U(x) \xrightarrow{F=K(x)U(x)} C(x) = U(x)^T K(x) U(x) \tag{3.7}$$

The global compliance can be decomposed in the sum of the elements compliance (c_e) as in equation 3.8a, where N is the number of elements used to discretize the design domain and u_e is the element displacement vector. In the same way, the global mass is represented in equation 3.8b where m_e is the element mass, ρ is the material's density and v_e is the element volume.

$$C(x) = \sum_{e=1}^{N} c_e = \sum_{e=1}^{N} u_e^T(x) K_e(x) u_e(x) \tag{3.8a}$$

$$M(x) = \sum_{e=1}^{N} m_e = \rho \sum_{e=1}^{N} x_e v_e(x) \tag{3.8b}$$

Termination criterion

The termination criterion is defined as the required condition to stop the optimization. In this thesis, 4 different criteria are used: Absolute difference between the objective function (equation 3.9a), relative difference between the objective function (equation 3.9b), absolute difference between the design variables (equation 3.9c) and maximum allowable iterations (equation 3.9d).

$$|OBJ^{new} - OBJ^{old}| \leq Conv.Val \tag{3.9a}$$

$$|\frac{OBJ^{new} - OBJ^{old}}{OBJ^{old}}| \leq Conv.Val \tag{3.9b}$$

$$|x_e^{new} - x_e^{old}| \leq Conv.Val \tag{3.9c}$$

$$Iter.num \leq Max.iter.num \tag{3.9d}$$

where OBJ is the objective function value, Conv.Val is the convergence value, Iter.num is the current iteration number and Max.iter.num is the maximum allowable iterations.

Filter functions

In order to ensure existence of solutions to the topology optimization problem and to avoid the formation of checkerboard patterns, some filters techniques were developed that are usually applied to the sensitivities or densities. Several filtering techniques are available in literature as Yan et al. [37]. This checkerboard effect is defined as regions with alternating void and solid elements ordered in a checkerboard-like fashion and it is demonstrated in figure 3.14 on a topology optimization analysis of a MBB-Beam.

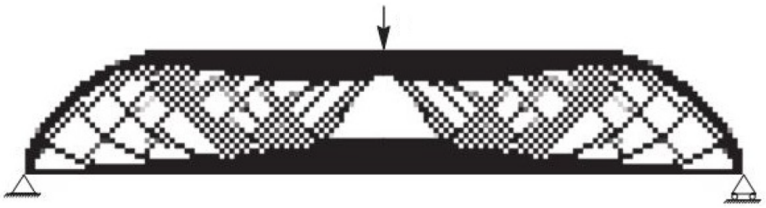

Figure 3.14: Checkerboards Effect on a MBB-Beam topology optimization analysis, adapted from [91].

3.3.1 Softwares

Nowadays, several commercial softwares are available for topological optimization. In this thesis, the chosen softwares are MSC Nastran with SOL 200 as solver (student version 2017.1) and Altair Hypermesh with Optistruct as solver (student version 13.0) since both have been and are being used in aerospace industry, and are in *Active Space Technologies* company's interests due to their reliable results. Both softwares results will be compared to decide which is more suitable for this application but before, in order to get more knowledge and sensitivity to the TO parameters, these softwares results will be compared with the available benchmark examples in the literature through TopOpt2D - Andreassen et al. [88] and TopOpt3D - Liu and Tovar [89]. Table 3.1 is a summary of the main characteristics of each software which will help to make some conclusions during their comparison.

Table 3.1: Softwares' basics characteristics for TO.

	Optistruct	**SOL 200**	**TopOpt2D**	**TopOpt3D**
TO method	SIMP	SIMP	Modified SIMP	Modified SIMP
Optimization algorithm	Dual method with multiple starting points	Sequential Unconstrained Minimization Technique	OC method	OC method
Sensitivity method	Adjoint method	Direct method	Adjoint method	Adjoint method
Convergence criterion	- Absolute changes in the objective function - Absolute changes in the design variables	- Absolute or relative changes in the objective function - Maximum allowable iterations	- Absolute changes in design variables	- Absolute changes in design variables - Maximum allowable iterations
Filters	- Minimum and maximum element size	- Checkerboard - Minimum element size	- Sensitivity - Density	- Density

More detailed information about table 3.1 contents is available in several documents as [7, 14, 15, 28, 88, 89, 92].

Chapter 4

Topology Optimization

4.1 Benchmark problems

In this section, two classical topology optimization problems - 2D Messerschmidt-Bölkow-Blohm (MBB) beam and 3D Cantilevered beam are used to improve the author's knowledge in this field. The objective is to gain sensitivity to the several TO parameters influence during the optimization process. This will be achieved through the comparison of the used commercial softwares with the already known Matlab's codes. Both benchmark problems use as objective function the minimization of compliance with a constraint in the volume fraction. Furthermore, these examples will also be used to perform a comparison between Altair Optistruct and MSC Nastran SOL200 softwares in order to choose the most suitable for the interface structure optimization.

The Messerschmidt-Bölkow-Blohm (MBB) beam is one of the most common studied cases for topology optimization. It is composed of a beam with a force – F of 1 Newton in its upper-middle section and a fixed and pinned constrain on the lower corners. Due to symmetry properties in static case, this model can be decomposed in the middle, with a pinned constrain, as depicted in figure 4.1.

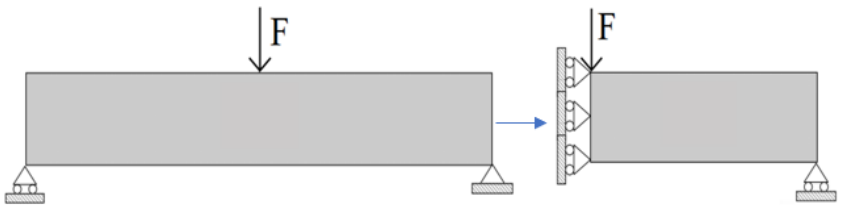

Figure 4.1: MBB Beam Model (Left) and MBB Beam Model simplification (right) with static boundary conditions, adapted from [28].

Another classic case for the topology optimization analysis is the Cantilever-Beam. This is composed of a beam with a clamped constrain on one side and a distributed force – F of 1 Newton on the other side in the lower edge of the beam, as depicted in figure 4.2.

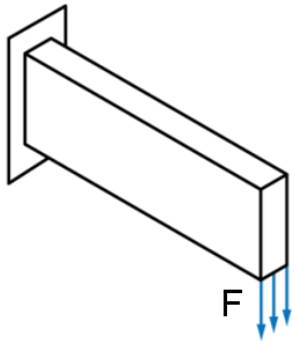

Figure 4.2: Cantilever Beam with distributed force, adapted from [89].

4.1.1 Literature verification - Matlab comparisons

The objective is to reproduce the several designs obtained through Matlab code so, some of the values used for the numerical model in each software were already defined and are presented in table 4.1. Matlab code uses the modified SIMP approach and that's why it uses an E_{min} value while SOL200 and Optistruct uses the x_{min} as explained in section 3.3. As shown before on table 3.1 the softwares have different convergence criteria as well as filters functions. In the case of Matlab, a density filter is used with a constant radius of action R_{min}. Detailed information about this can be found on [28]. Differently from the checkerboard filter used by SOL200, Optistruct uses a minimum dimension constraint to avoid checkerboard effect as described by Altair Engineering [92] and verified by the author. Since Matlab and Optistruct uses absolute differences for the convergence criteria and the differences in the objective function values are not significant to use relative differences, SOL200 will also be used with its hard convergence method – absolute difference in the objective function.

Table 4.1: TO model parameters for the several softwares.

	SOL200	Optistruct	Matlab
2D	- E_0=1 Pa - x_{min}=0.001 Kg/m^3 - ν=0.3 - $OBJ^{new} - OBJ^{old}$<0.01 - $Max.iter.num$<500 - Checkerboard filter - F=1 N - $x_{initial}$ = "f" in Kg/m^3	- E_0=1 Pa - x_{min}=0.001 Kg/m^3 - ν=0.3 - $x_e^{new} - x_e^{old}$<0.01 or $OBJ^{new} - OBJ^{old}$<0.01 - F=1 N - Minimum dimension constraint with size= 0.5 mm	- E_0=1 Pa - E_{min}=1e-9 Pa - ν=0.3 - $x_e^{new} - x_e^{old}$<0.01 - Density filter - F=1 N - R_{min}=1.5 mm
3D	- E_0=1 Pa - x_{min}=0.001 Kg/m^3 - ν=0.3 - $OBJ^{new} - OBJ^{old}$<0.01 -$Max.iter.num$<500 - Checkerboard filter - F=1 N - $x_{initial}$ = "f" in Kg/m^3	- E_0=1 Pa - x_{min}=0.001 Kg/m^3 - ν=0.3 - $x_e^{new} - x_e^{old}$<0.01 or $OBJ^{new} - OBJ^{old}$<0.01 - F=1 N - Minimum dimension constraint with size=0.5 mm	- E_0=1 Pa - E_{min}=1e-9 Pa - ν=0.3 - $x_e^{new} - x_e^{old}$<0.01 -$Max.iter.num$<500 - Density filter - F=1 N - R_{min}=1.5 mm

In SOL200 and Optistruct, by following the Matlab finite element code, for 2D analysis a quad element with 4 nodes and PSHELL properties with 1mm of thickness is used and for 3D analysis, the used element is a Brick/Hex with 8 nodes and PSOLID properties. The PSHELL element property is used

because the thickness dimension is very small when compared with the others. Besides, the problems are in a plane stress state. The PSOLID element property is generally suited for linear analysis. Furthermore , quad elements with four nodes and Brick elements with 8 nodes are a good balance between accuracy and computational cost.

In order to study the three biggest variables of interest in TO, 3 models variations for each variable were developed as shown in table 4.2. Firstly, for the volume fraction "f" values, the objective was to use regular intervals (0.2 between each) that could make some difference and at the same time don't be near to the extreme values (0 and 1) since values like 0.1 or 0.9 will hardly be used in the final product. Secondly, for the mesh influence, the bigger model – size 3 was developed based on the mesh size used in the papers [88] and [89] with small adaptations and after that, for the size 2 and size 1, the number of elements were typically reduced by a scale factor of 2. In the case of y component in the 3D model, the dimension was not changed to keep a reasonable number of elements in y direction, otherwise, it would end up in a 2D problem since in these problems the number of elements it's equal to the respective part length. Lastly, the penalization power values were chosen to see the "non-penalized solution" with "$p = 1$", the solution with the most recommended value by literature – "$p = 3$" and a very penalized solution within the recommended boundaries – "$p = 6$".

As explained, in these examples the size of the problem is equal to the mesh dimensions so, there is a relative mesh refinement since the size of the element compared to the size of the model is smaller than in the other model. However, this can influence the results if the problem is size dependent which is very common.

Table 4.2: Benchmark examples analysis combination.

		No. of elements in x	No. of elements in y	No. of elements in z	p – penalization factor	f – volume fraction
MBB beam - 2D	*f influence*	120	60	-	3	0.3
		120	60	-	3	0.5
		120	60	-	3	0.7
	Mesh influence	30	15	-	3	0.5
		60	30	-	3	0.5
		120	60	-	3	0.5
	p influence	120	60	-	1	0.5
		120	60	-	3	0.5
		120	60	-	6	0.5
Cantilevered beam - 3D	*f influence*	60	4	20	3	0.3
		60	4	20	3	0.5
		60	4	20	3	0.7
	Mesh influence	15	4	6	3	0.5
		30	4	10	3	0.5
		60	4	20	3	0.5
	p influence	60	4	20	1	0.5
		60	4	20	3	0.5
		60	4	20	6	0.5

All the obtained solutions are represented in figures B.1 and B.2 in appendix B. They are presented with the elements with a relative density equal or higher than 0.5 and without the use of smoothing tools in the post-processing phase. Some of the results can also be seen in figure 4.3 and 4.4.

As expected, the geometric results from Matlab, SOL200 and Optistruct are similar in their core. However, the Optistruct and Matlab results have more similarities. This can be justified by the sofwares sensitivity method that are the same as shown before in table 3.1. In the 2D and 3D optimization, SOL200 typically has a more “grey solution” when compared with the others.

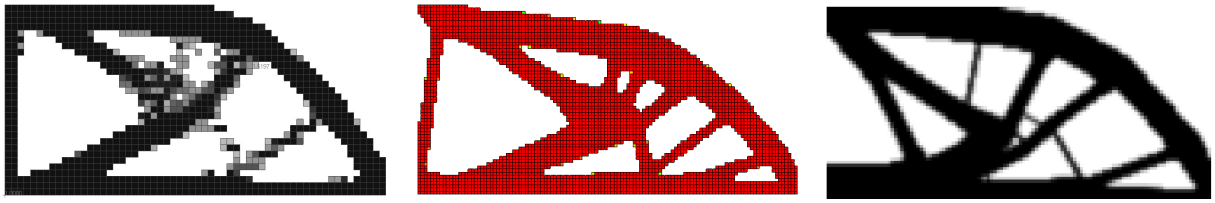

(a) SOL200. (b) Optistruct. (c) Matlab.

Figure 4.3: 2D problem with p=3 during p influence study.

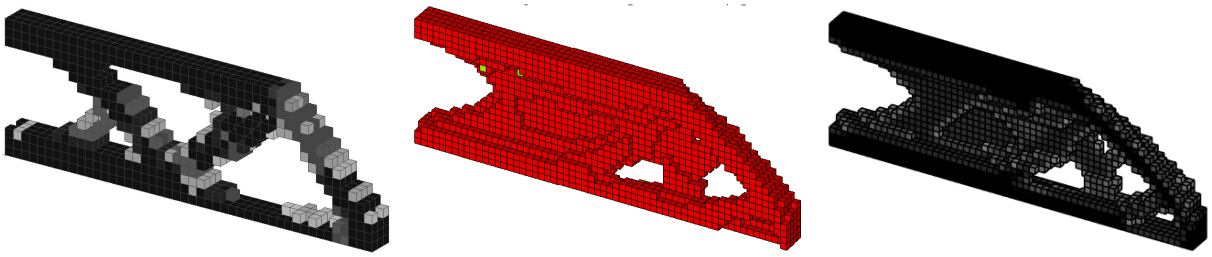

(a) SOL200. (b) Optistruct. (c) Matlab.

Figure 4.4: 3D problem with f=0.5 during f influence study.

Matlab needs more iterations to converge when compared to the other two softwares which suggests that the optimization algorithm is not as good as the others for this applications, at least. For the compliance values, Optistruct shows the best results with an average value of the 2D optimization equal to 68.0% and 48.6% from the compliance values of Matlab and SOL200, respectively and an average value of the 3D optimization equal to 37.1% and 31.1% from the compliance values of Matlab and SOL200, respectively. All this comparisons can be seen in table 4.3 and figures 4.5, 4.6, 4.7 and 4.8.

Table 4.3: Benchmark examples optimization values.

		Matlab		SOL200		Optistruct		
		No. of iterations for convergence	Compliance [Nm]	No. of iterations for convergence	Compliance [Nm]	No. of iterations for convergence	Compliance [Nm]	Parameter
MBB beam - 2D	*f influence*	418	140.06	27	214.61	37	85.78	*f=0.3*
		389	82.28	17	112.78	23	59.23	*f=0.5*
		345	61.67	13	93.43	14	50.32	*f=0.7*
	Mesh influence	94	94.06	30	120.70	31	48.40	*size 1*
		260	85.32	21	108.57	26	53.19	*size 2*
		389	82.28	17	112.78	23	59.23	*size 3*
	p influence	49	69.21	18	114.63	22	58.97	*p=1*
		389	82.28	17	112.78	23	59.23	*p=3*
		222	95.77	19	118.86	24	64.84	*p=6*
Cantilever beam - 3D	*f influence*	487	96.69	46	165.46	33	38.68	*f=0.3*
		341	73.27	30	56.56	26	22.19	*f=0.5*
		162	36.71	25	38.30	18	17.31	*f=0.7*
	Mesh influence	56	42.49	38	49.11	33	15.03	*size 1*
		114	56.28	30	83.19	33	22.67	*size 2*
		341	73.27	30	56.56	26	22.19	*size 3*
	p influence	38	39.86	24	70.31	27	21.60	*p=1*
		341	73.27	30	56.56	26	22.19	*p=3*
		211	59.83	17	83.10	24	22.84	*p=6*

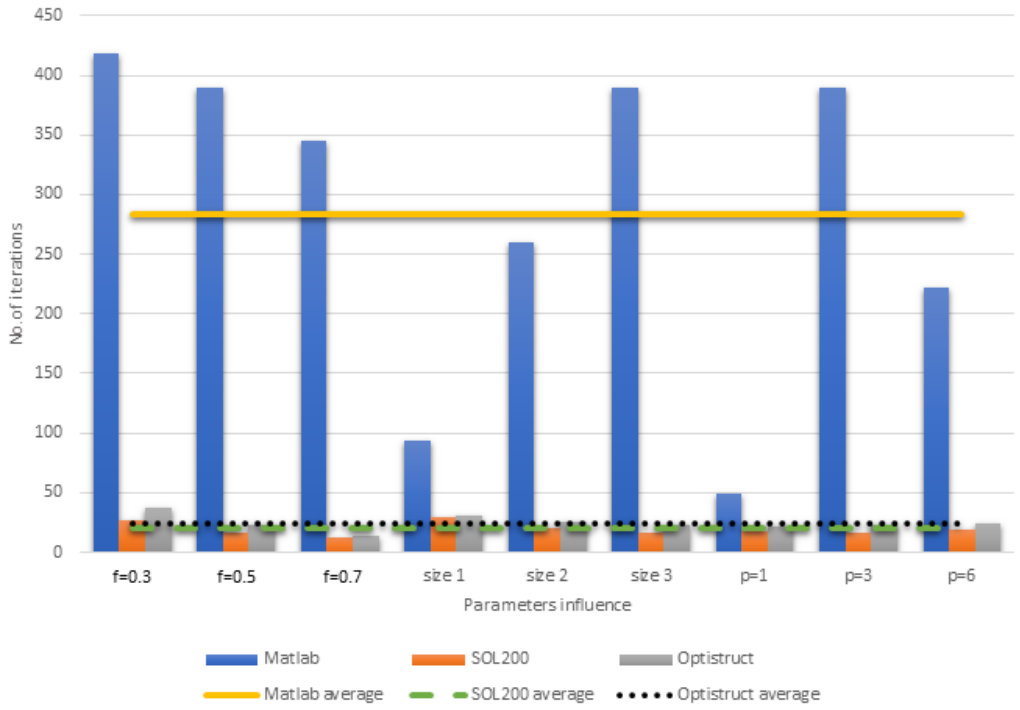

Figure 4.5: No. of iterations for convergence - 2D.

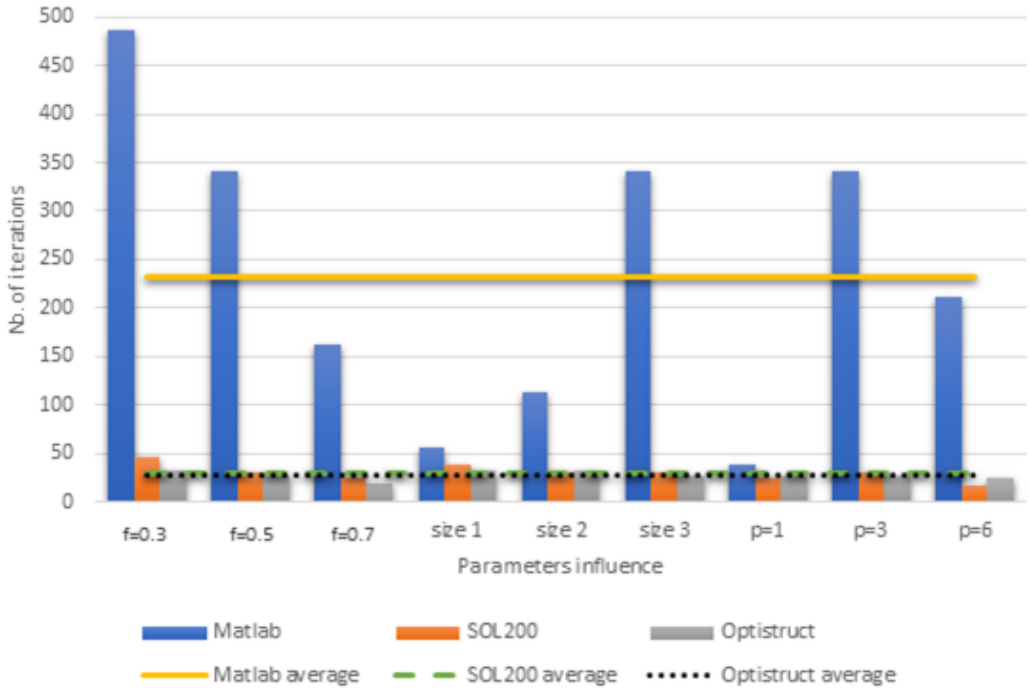

Figure 4.6: No. of iterations for convergence - 3D.

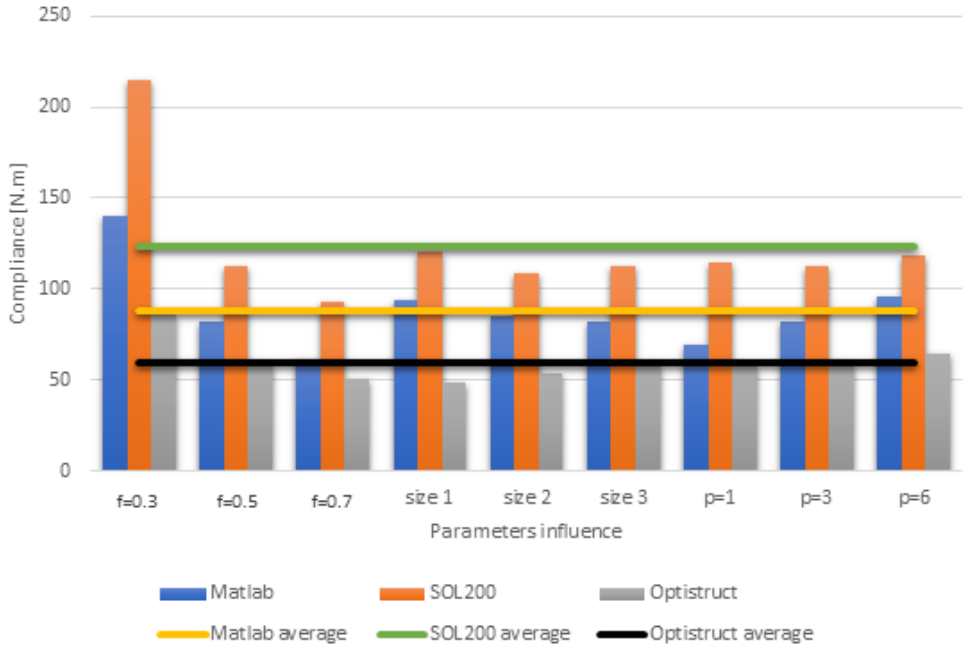

Figure 4.7: Compliance values - 2D.

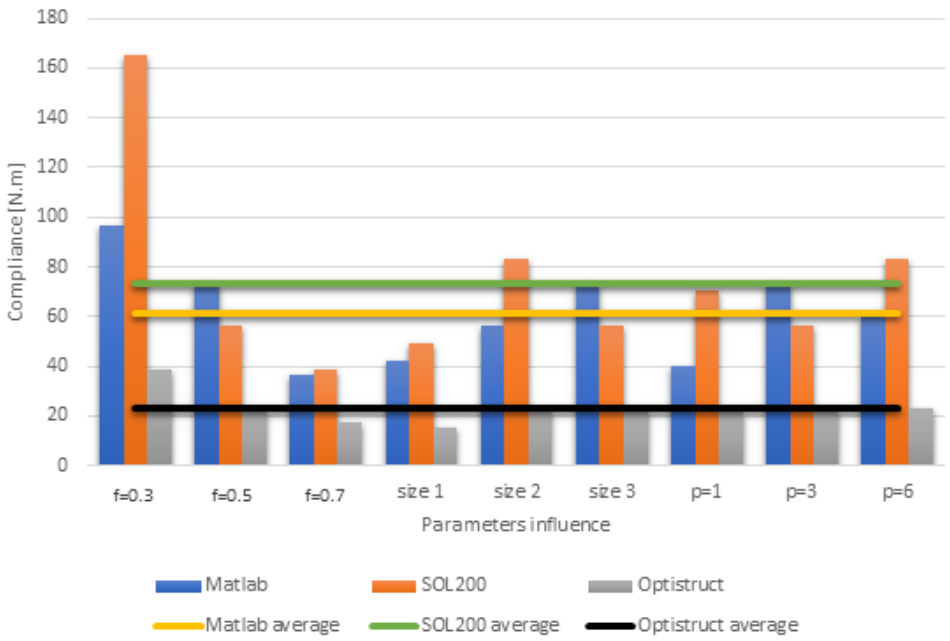

Figure 4.8: Compliance values - 3D.

Volume fraction - f influence

As expected, this parameter has a considerable influence in the optimized design results. With the decreasing of the volume fraction value, the number of iterations to converge increases as well as the compliance of the structure since this corresponds to use a higher constraint – lighter solution. Besides, it is possible to see in figure 4.9 and 4.10 that with a lower volume fraction value a more complex geometry is achieved.

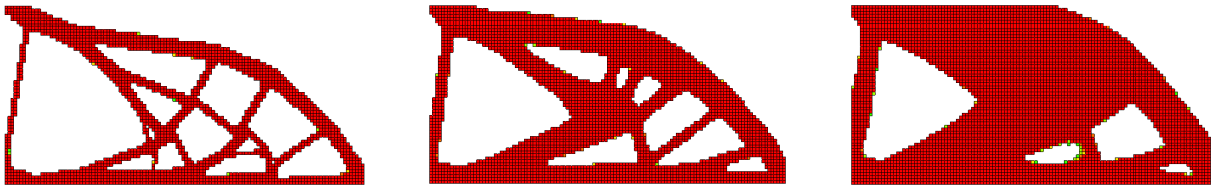

(a) f=0.3. (b) f=0.5. (c) f=0.7.

Figure 4.9: 2D problem with Optistruct during f influence study.

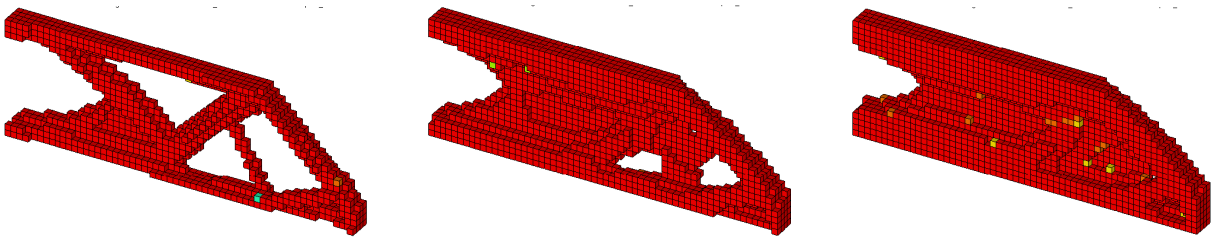

(a) f=0.3. (b) f=0.5. (c) f=0.7.

Figure 4.10: 3D problem with Optistruct during f influence study.

Mesh size influence

It was expected that with the mesh refinement, a more detailed solution would be achieved. Besides, it is also expected that the number of iterations for convergence would increase while the compliance value should decrease. However, it is possible to verify that this does not happen regularly. In some cases, like Matlab 2D optimization, it happens, but in others it does not, as in Optistruct 3D. This occurs due to the increasing size of the model with the refinement of the mesh which ends up creating different solutions. One regular result of this effect in the two comercial softwares (SOL200 and Optistruct) is the increasing compliance value from the 3D size 1 mesh to the size 2 while it decreases from size 2 to size 3. The cantilever beam is size dependent because in mesh size 1, the length is short enough to make the bending moment small and a very stiff structure giving a lower value for its compliance when compared to mesh size 2 or 3. So, from mesh size 1 to size 2, the “active controller” of the optimization was the size of the problem and not the mesh refinement as supposed initially. The decreasing effect in the compliance value from size 2 to size 3 is a consequence of a refined mesh relative to the problem size which is the “active controller”. Based on this, the different solutions cannot be compared with the previous ones but should be compared with the same model result in a different software. In that case, in their core, all solutions present a similar geometry as shown in figure 4.11 and 4.12.

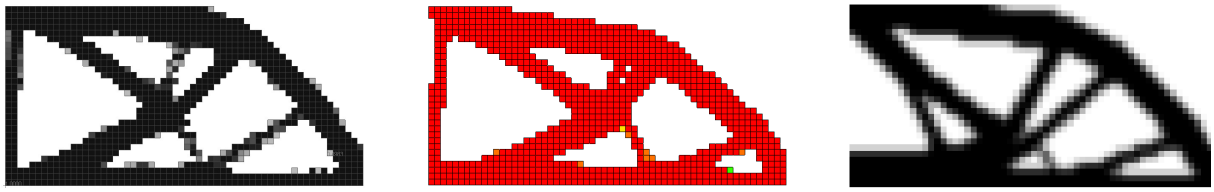

(a) SOL200. (b) Optistruct. (c) Matlab.

Figure 4.11: 2D problem with mesh size during mesh size influence study.

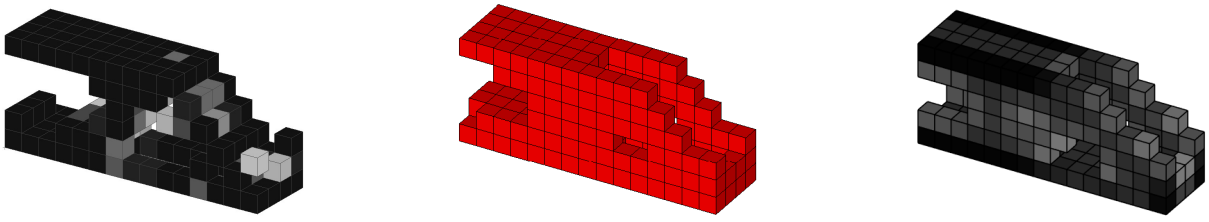

(a) SOL200. (b) Optistruct. (c) Matlab.

Figure 4.12: 3D problem with mesh size during mesh size influence study.

Penalization factor - p influence

The variation of the number of iterations does not have a significant variation with p value except for Matlab. Besides, it is possible to conclude that for Matlab results, p equal to 3 is not the best option as the literature recommends. However, by looking at SOL200 and Optistruct results, the compliance values with p equal to 3 are the lower ones or similar to the lowest one. These differences in the results are justified by the different softwares' optimization algorithms and filters techniques. The two most interesting things to learn from this analysis are: Firstly, the penalization factor really allows the

engineer to avoid grey solutions and achieve more detailed ones (figure 4.13 and 4.14). Therefore, theoretically, increasing the p value as high as possible should give the most detailed and easier solution for post-processing. Secondly, as verified, the highest p value is not the best option numerically and that's also why there are a range of values recommended for TO. So, the penalization factor value is problem dependent and should be chosen based on experience or experimentation for the specific design problem.

(a) p=1. (b) p=3. (c) p=6.

Figure 4.13: 2D problem with Matlab during p influence study.

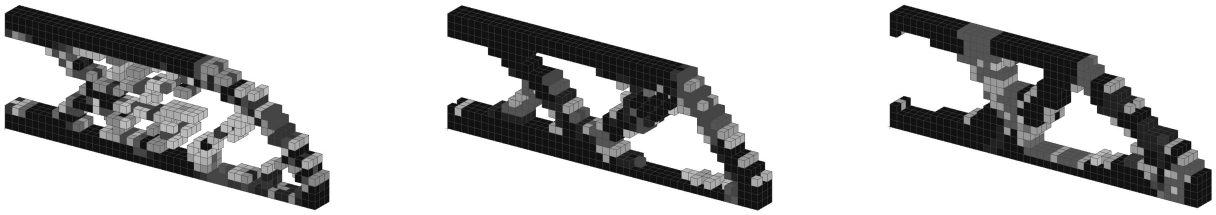

(a) p=1. (b) p=3. (c) p=6.

Figure 4.14: 3D problem with SOL200 during p influence study.

Post-processing

From the author's knowledge, MSC Nastran SOL200 only has one simple feature that allows the smoothing of the new geometry while Optistruct has 4 different ones which gives more freedom to the engineer. Besides, Optistruct has an improved smoothing tool called "OSSmooth". This tool can be used to achieve complex smoothed geometries quickly, even though it depends on the size of the element used in the analysis. Furthermore, Optistruct also allows the re-analysis of the new smoothed geometry which will save a lot of time.

4.1.2 Benchmark examples remarks - software choice

During this section (4.1) it is noteworthy to mention the success of the TO implementation and the achieved conclusions about some of its several parameters. It is also important to refer the comparisons between Altair Optistruct and MSC Nastran SOL200 where the overall best performance during the iterations and compliance results in the 2D and 3D examples was achieved by Optistruct. Another key factor for Optistruct in terms of quality and time/cost is the improved tools for the smoothing working and re-analysis of the final geometry. Moreover, in the author's opinion, Optistruct's Graphical User Interface (GUI) is easier to use when compared to SOL200. So, the software that will be used for the interface structure optimization is Altair Optistruct.

4.2 Topological optimization problem's formulation

Following the target structure requirements, the structure needs to be light, to have a minimum value of first mode frequency and to endure a high number of working cycles. A very known way to solve this kind of problems with TO is similar to the one used in the previous benchmark examples: Minimize compliance and constraint the volume fraction. By minimizing compliance, the structure will be stiffer and consequently, the first mode frequency will be higher since this value is a consequence of the balance between the mass and the stiffness of the structure. By constraining the volume fraction and selecting the threshold values of element densities in the post-processing, a reduction in the structure mass will be achieved and it is possible to manipulate the final present stresses for fatigue calculations.

The problem formulation that will be used in this thesis will be different from the previously explained. Based on the target structure's requirements and the achieved findings in the benchmark examples analysis, it would be wise to use an objective function that minimizes the mass to avoid the usage of a volume fraction constraint since it has a considerable influence in the optimized results. This option would lead to a multi-objective optimization, but this will not be the case because the minimum value for the first mode frequency is known. So, this value shall be used as constraint. To avoid fatigue issues, a maximum allowable stress constraint equal to the material's fatigue stress limit shall be used too. These two constraints make the use of the compliance objective function meaningless for the problem.

The author thinks that this formulation is more suitable for the specific problem since it can ensure the frequency requirement, the fatigue behaviour and within these limits it will reduce the mass as much as possible while in the other formulation the final values for frequency and stresses could be too much conservative which would end up in a heavier solution. Furthermore, it would be more time expensive due to the amount of volume fraction constraint iterations.

To make sure that a reliable structure will be designed, an experimental work will be developed to validate this optimization approach technique.

4.3 Numerical modelling - general initial model

The problem's model for the optimization validation is similar to the one explained in section 2.2. However, it has some noteworthy different characteristics:

- The material that will be used for this problem is the *VisiJet M3 Crystal* polymer [93] that is used on *ProJet MJP 3600* [94] from *3D Systems* [95]. This material was chosen since it was the one available at Instituto Superior Técnico (IST) in a machine with good accuracy for the afterwards experimental specimen production. Ideally, this would be done with a metal part but it was not possible due to economic issues as well as all the complexity in post-processing phase as referred before;
- Since the polymer is weaker than the aluminum, the base acceleration value for the load cases is 1G instead of 60Gs. This value was achieved from a simple proportionality between the materials Young's modulus as shown by equation 4.1. The Young's modulus was chosen instead of the

strength (equation 4.2) because the material's stiffness will have more influence over the optimization than the strength as explained before. Besides, from equation 4.1 and 4.2, the proportionality with the Young's modulus gives the lower acceleration value;

$$a_{polymer} = \frac{\sigma_{y-polymer} \cdot a_{Al}}{\sigma_{y-Al}} = \frac{1442.67 \cdot 60}{70000} \approx 1.24Gs \tag{4.1}$$

$$a_{polymer} = \frac{\sigma_{y-polymer} \cdot a_{Al}}{\sigma_{y-Al}} = \frac{20.63 \cdot 60}{255} \approx 4.85Gs \tag{4.2}$$

- The structure will be divided into two regions:
  - Non-design space (figure 4.15a) – Essential parts for the structures as the connections points for the screws. These parts instead of having 12mm of thickness as before, they only have 10mm;
  - Design space (figure 4.15b) – All the rest of the volume with some assembly constraints. The objective of this design region is to use the outside dimensions of the L-shape structure at their limit to expand the geometric freedom for the TO. So, a solid rectangular prism with 120mmx120mmx100mm as dimensions is used with some empty spaces to allow the mounting of the hardware system assembly and some of its movement during the experiment. The space for the hardware system is characterized by three holes for the connection tubes and a prism volume cut that allows the hardware system (figure 4.15c). Further on, an optimization cycle will be presented where some changes will be applied to this general design space based on results conclusions;

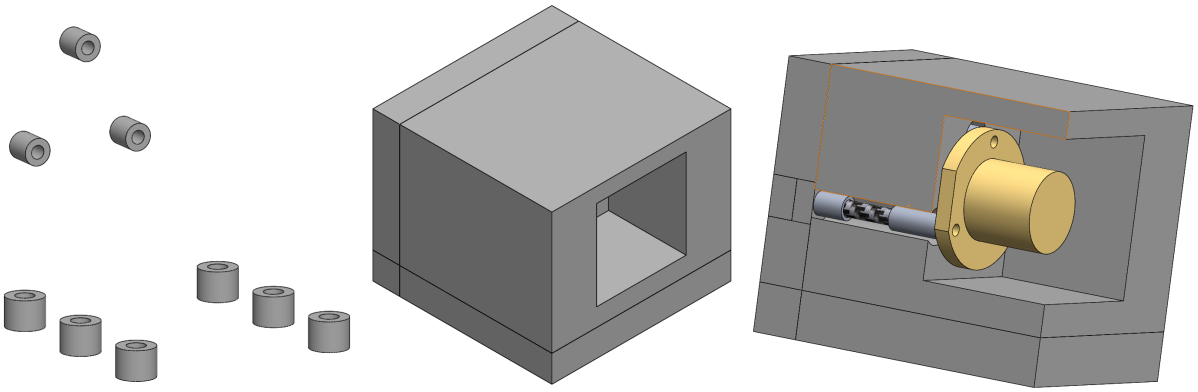

(a) Non-design space. (b) Design space. (c) Hardware system assembly's free space.

Figure 4.15: General initial model.

- RBE2 elements were used instead of the CBAR for the connection tubes. This is done to increase the speed of the optimization and to make the first mode of the assembly as close as possible of the interface structure mode shape. Although it could lead to excessive stresses in the structure, that will not be a problem since the stress values are low, as stated before. Besides, the stiffness of the assembly will be higher which would increase "artificially" the frequency of the system but

that is not a problem too since the frequency requirement is for the interface structure individually and the optimization is just to get a design concept;

- CONM2 element were used instead of the hardware system structure in order to increase the optimization speed. This element simulates the CoG of the hardware system (figure 4.16);

- RBE2 elements were used to simulate the structure of the hardware system by linking the three joint points between them and the CoG. The reason to use this element is because it will not change the element length which will make the artificial hardware system to work with a rigid body motion (figure 4.16);

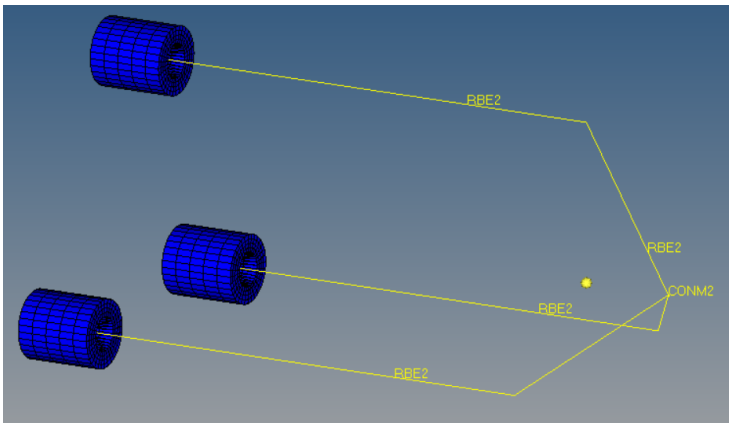

Figure 4.16: Hardware system simplified model.

- Tetra elements with the same element size as the Hex elements were used in this analysis since it has a complex geometry to model with Hex elements. In order to ensure that tetra elements with 2mm as global element size is a good choice, an analysis to the L-shape model with Tetra elements instead of Hex elements was done. The relative difference between the results of the Hex and Tetra meshes with element size of 2mm can be seen in table 4.4. These differences suggest that the Tetra elements can be used without significant accuracy loss.

Tetra mesh characteristics for the L-shape model re-analysis:

- Total number of elements: 452360;

- Global element size: 2mm;

- Worst jacobian: 0.88;

- Worst aspect ratio: 4.53.

Table 4.4: Relative difference between Hex and Tetra mesh results.

		Hex to Tetra
Modal analysis: Frequency	*1st Mode*	0.05%
	2nd Mode	0.21%
	3rd Mode	1.15%
Static analysis: Displacement [mm]	*1st Load case*	3.54%
	2nd Load case	1.17%
	3rd Load case	3.54%
	4th Load case	1.17%
	5th Load case	1.17%
	6th Load case	3.54%
	7th Load case	1.17%
	8th Load case	3.54%

Tetra mesh characteristics for the general inital model (figure 4.17):

- Total number of elements: 1222022;
- Global element size: 2mm;
- Worst jacobian: 0.48 in 27 of 1222022 which is meaningless (≈0.00%);
- Worst aspect ratio: 4.53.

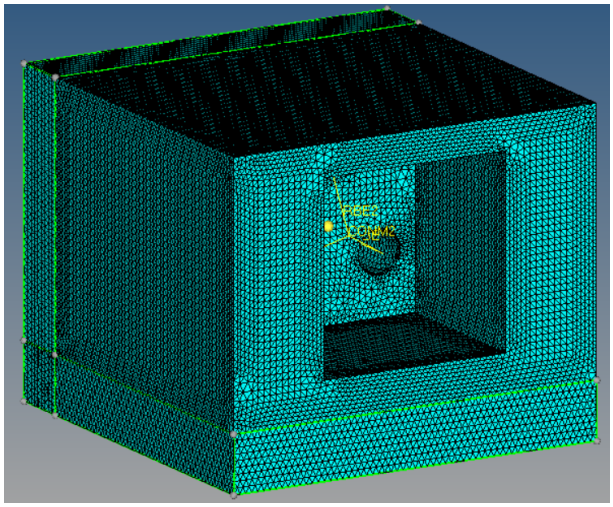

Figure 4.17: General initial model mesh.

The constraint values defined before are suitable for the metal design. However, in this polymer model, the constraints values should be properly chosen. So, in order to choose some of the optimization parameters and constraints values, an analysis to the general initial model will be made to assess its current performance and based on that, define the optimization constraints. However, before the numerical analysis, it is important to verify the material's properties that are present in its datasheet as well as characterize others that are not. All the experimental characterization process can be seen in detail in appendix C where the most important things to retain is the material's isotropic behaviour in the elastic region and its properties that are depicted in table C.6.

4.4 Numerical analysis

To use as base for the constraints, a static (figure 4.18a) and modal analysis (figure 4.18b) are performed to know the stress values for the 8 load cases and the 3 first frequencies, respectively. Using the FEM model explained in section 4.3, the analysis results can be seen in table 4.5 and 4.6.

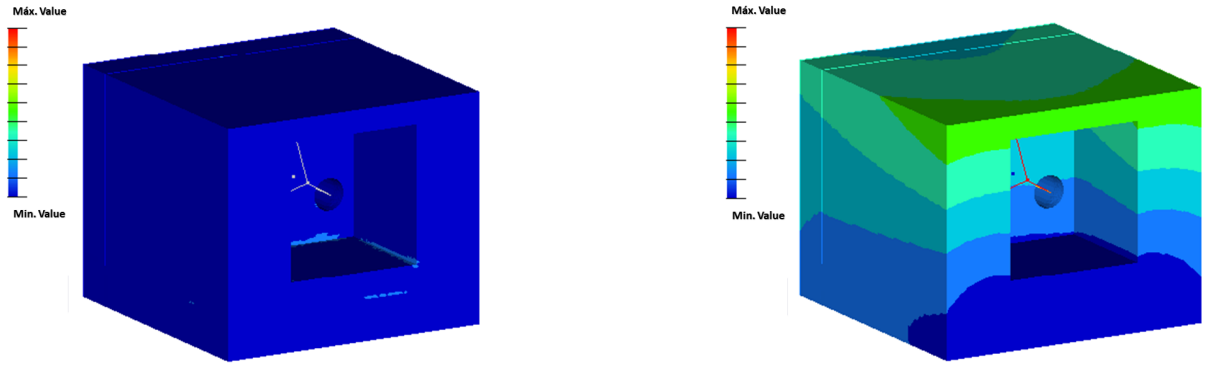

(a) Static analysis 1st load case.

(b) Modal analysis 1st mode.

Figure 4.18: General initial model analysis.

Table 4.5: Initial general model static analysis - stress results.

Load cases	Maximum stress [MPa]
1st	7.52e-02
2nd	7.40e-02
3rd	6.21e-02
4th	5.87e-02
5th	5.87e-02
6th	6.21e-02
7th	7.40e-02
8th	7.52e-02

Table 4.6: Initial general model modal analysis - frequency results.

Modes	Frequency [Hz]
1st	569.50
2nd	612.31
3rd	701.74

As expected, the stress values are low when compared to the material's yield strength. During the optimization phase, the active constraint will probably be the frequency value but the stress constraint will also be calculated through equation 4.3 for yield and not fatigue stress values. The frequency constraint was decided to be 350Hz just for experimental purposes. This value comes as a reasonable choice since it is relatively below the first mode value found which enables significant TO work but without being too low.

$$MoS_y \geq 0 \Rightarrow \frac{\sigma_{applied} \cdot FoS_y}{\sigma_y} - 1 \geq 0 \Rightarrow \sigma_{applied} \leq \frac{\sigma_y}{FoS_y} = \frac{20.63}{2} \approx 10.32\ MPa \tag{4.3}$$

4.5 Numerical optimization cycle

Based on the benchmark examples optimizations (section 4.1) and the previous analysis, the optimization parameters were defined. The convergence value is changed from 0.01 to 0.005 since it is the one used as default by the program and there is no more necessity to compare it with Matlab's results. The material properties are adapted for the new material used and the minimum initial density value is the same used before. The penalization factor is the recommended since it has also shown good results in section 4.1.1 Besides, the maximum accuracy of the machine is 0.05mm. So, a minimum dimension constraint of one higher order of magnitude will be used: 0.5mm. As stated before, the FEM model that will be used is the initial general model from section 4.3 and the stress and frequency constrains were already defined. The optimization parameters are resumed in table 4.7.

Table 4.7: Optimization model parameters – polymer structure.

E_0	1442.67 MPa
x_{min}	0.001 Kg/m^3
p	3
ν	0.37
Conv.Val	$<$0.005
Dimension constraint	$\geq$ 0.5 mm
Stress constraint	$\leq$ 10.32 MPa
Frequency constraint	$>$350 Hz

The final topology was achieved through an optimization cycle composed by 3 phases that will be described in sections 4.5.1, 4.5.2 and 4.5.3.

4.5.1 Optimization cycle - phase 1

In this phase, the difference in the design space when compared to the initial one described in section 4.3 is the empty spaces for the screws' heads and washers in the base joints (figure 4.19). However, the space to insert the tool to tight them is not pre-defined. The author pretends to assess the optimal topology on that area and using that as base concept to open enough space for the Allen wrench in the second phase.

(a) (b)

Figure 4.19: Screw's head and washer's open space.

After the optimization run, several designs can be seen by using different threshold values for the element densities, that's why TO typically gives a conceptual design. However, by using Optistruct re-analysis method with a defined threshold value, it is possible to know the design that should be used in a brief time. This re-analysis method is one of the reasons that made the author choose Altair Optistruct instead of MSC Nastran SOL200 for the TO as explained before. This tool allows the user to choose the minimum density value for the elements to be considered and then, the software re-analyze the structure with the same mesh and boundary conditions. In the end, Optistruct's results will show if the structure fulfills the TO requirements or not. If the results are not acceptable, the user just needs to try another density value until a feasible design is achieved.

For the first optimization phase, the necessary threshold value is 0.45 and the respective design can be seen in figure 4.20. The maximum present stress value from the 8 load cases is 7.517e-02MPa which is far below the constraint value, as expected. So, from now on, this constraint will not be used. The frequency value achieved is 392.63Hz which meets the requirement.

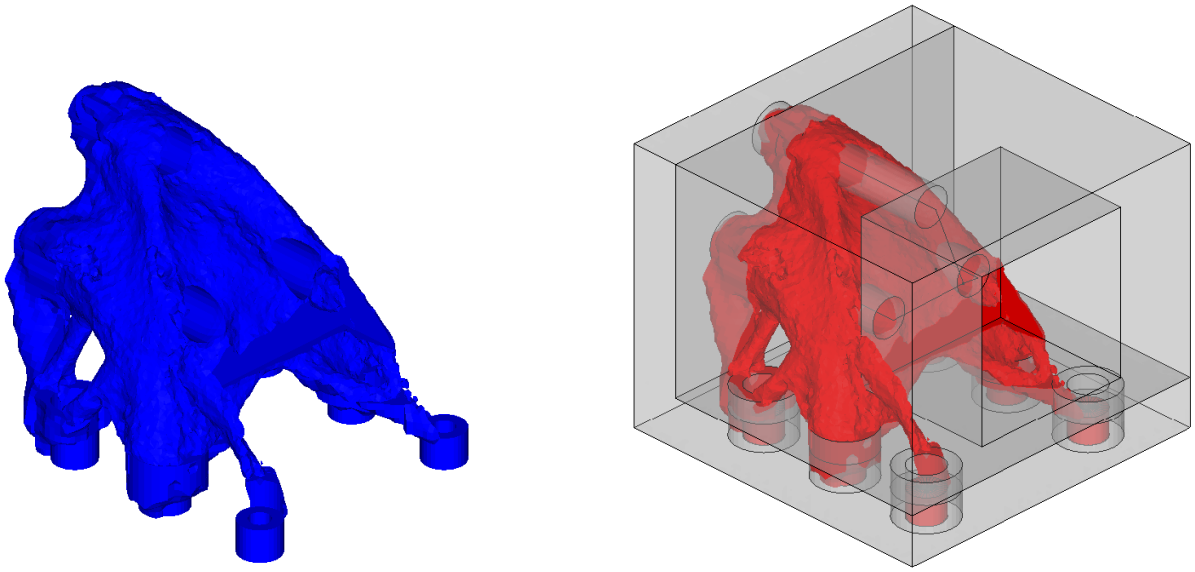

(a) (b)

Figure 4.20: Optimization topology results - phase 1.

From the obtained results, it is possible to conclude that the two front bolts are probably not necessary, but the rest of the geometry makes sense. The 4 rear base bolts are strongly connected to the center of the structure and the 3 bolts that connect the structure to the hardware system. Although it is straightfoward to have a reinforced part to sustain the connections linkage, it is also logical to have it a little closer to the top 3 bolts since these ones suffer the loads from the hardware's system.

4.5.2 Optimization cycle - phase 2

Based in section 4.5.1 results and conclusions, the design space of this phase will be reduced to decrease the computational time and the two front bolts will still be used but as a design space part instead of a non-design space to confirm if they are really necessary or not. The reduction is based in

the material that is quickly removed in the first optimization iterations due its low contribution as shown in animated figure D.1 in appendix D. Besides, the author can now open some space for the Allen wrench in the base bolts region in a smart way: trying to avoid as possible the cut of regions with material in the phase 1 results. The phase 2 design space can be seen in figure 4.21.

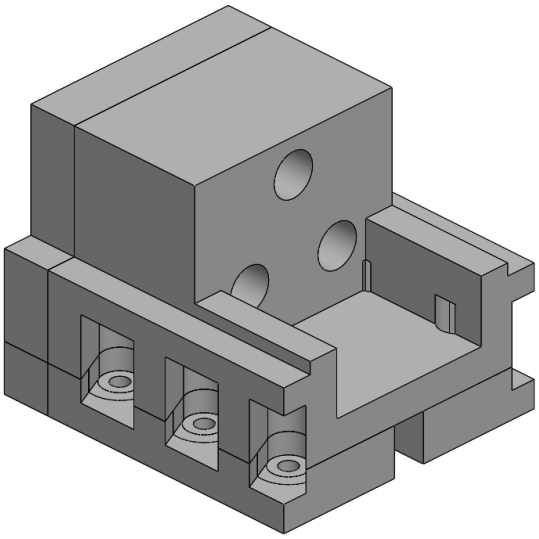

Figure 4.21: Design space - phase 2.

For the second optimization phase, the necessary threshold value is 0.25 and the respective design can be seen in figure 4.22. The frequency value achieved is 373.00Hz which meets the requirement.

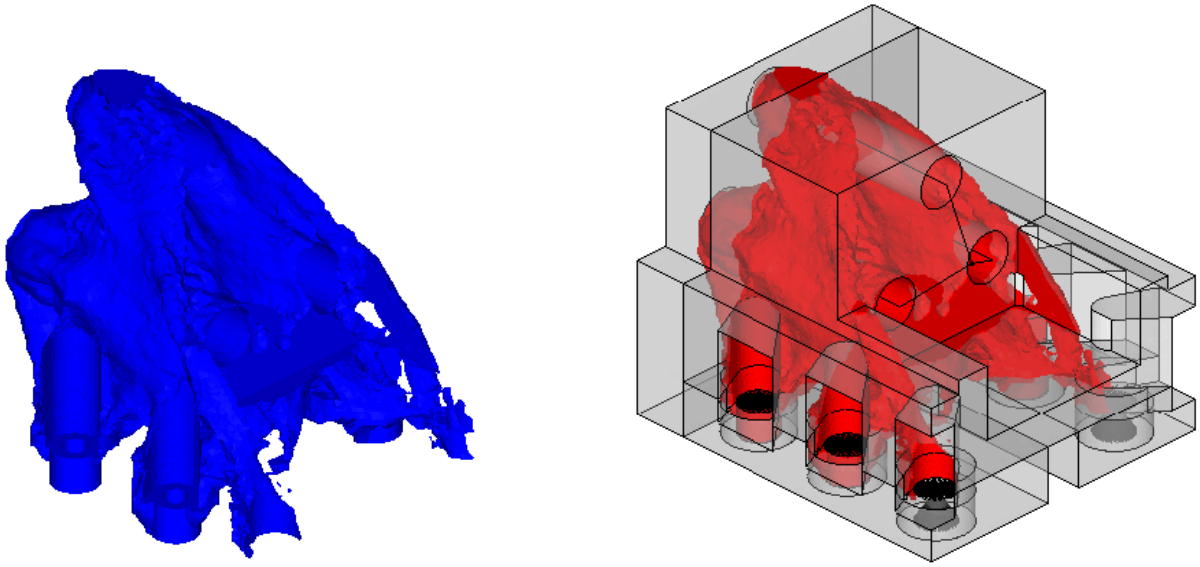

(a) (b)

Figure 4.22: Optimization topology results - phase 2.

From the obtained results, it is possible to conclude that the two front bolts are not necessary since they don't have a significant continuity in the material to the rest of the structure. They are only there due to the boundary conditions. The rest of the geometry continues to make sense and it is similar to the previously obtained which is a positive feedback and suggests consistency in the results.

4.5.3 Optimization cycle - phase 3

Based in section 4.5.2 results and conclusions, the design space of this phase will be readapted due to some excessive cuts and geometry changes as consequence from the Allen wrench opened space effect. Besides, the 2 front bolts will be completely removed to achieve a more compact design. However, in this phase, in order to see the structure evolution if there was not so much available material in the center, a second design space will also be optimized. The choice of taking off some material from the mid region is because that is the region with more material concentrated and this can lead to a better material distribution even if that costs some weight in the final product. The phase 3 design spaces can be seen in figure 4.23.

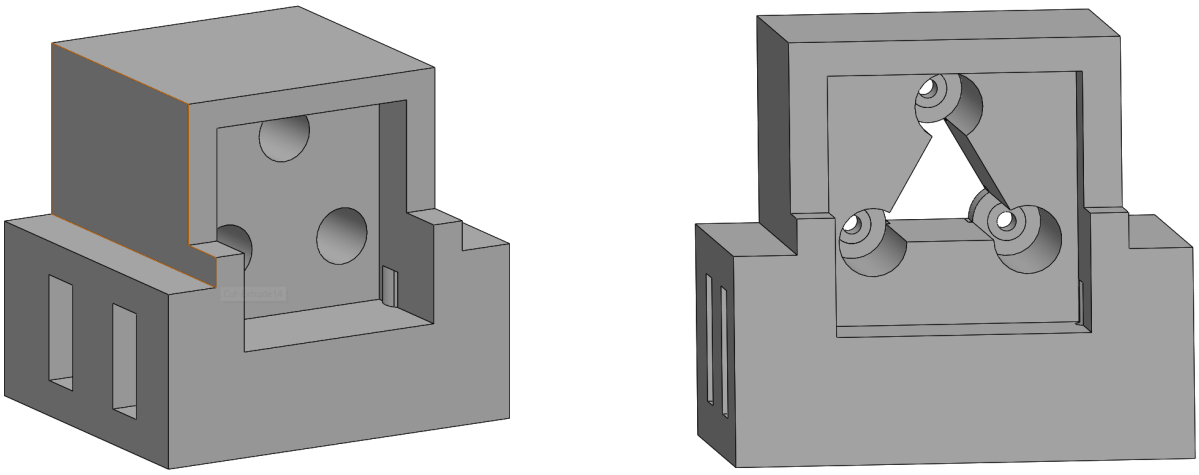

(a) 3a. (b) 3b.

Figure 4.23: Design spaces - phase 3.

For the third optimization phase, the necessary threshold value for design 3a is 0.3 with a frequency value achieved of 359.95Hz while for design 3b the necessary threshold value is 0.25 with a frequency value achieved of 353.78Hz. Both designs meet the requirement and can be seen in figure 4.24 and 4.25, respectively.

In general, both designs present similar topologies to the previously obtained which once more, is a positive feedback and suggests consistency in the results. However, by comparing design 3a and 3b topologies, it is possible to conclude that design 3b does not present any advantage in terms of geometry. Neither by easier assembly mountings nor by better material distribution along the full structure. Instead, design 3b shows significant bigger legs to compensate the lack of material in the middle while 3a presents a compact and continuous material distribution along all linkages.

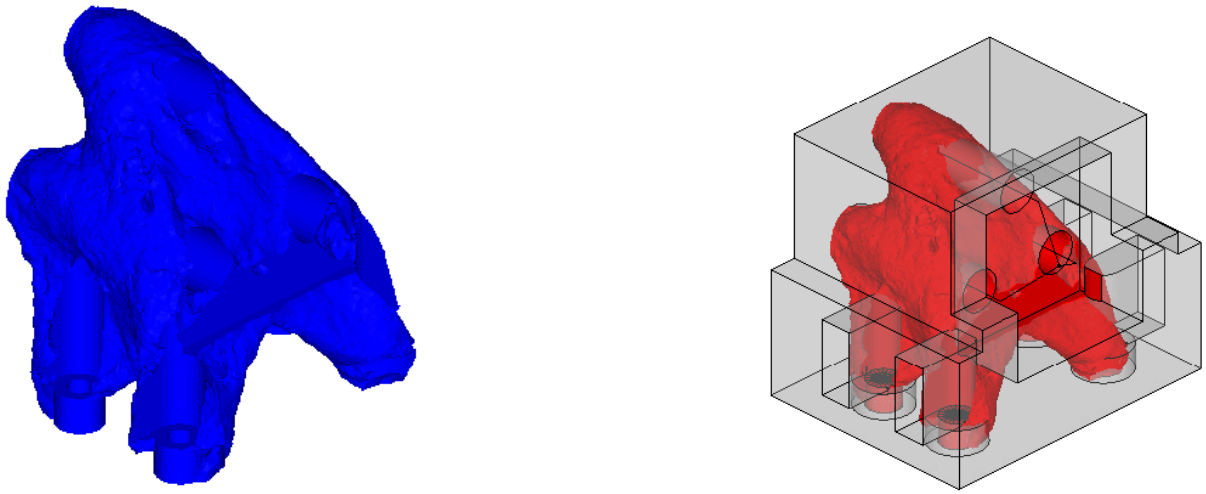

(a) (b)

Figure 4.24: Optimization topology results - phase 3 - design a.

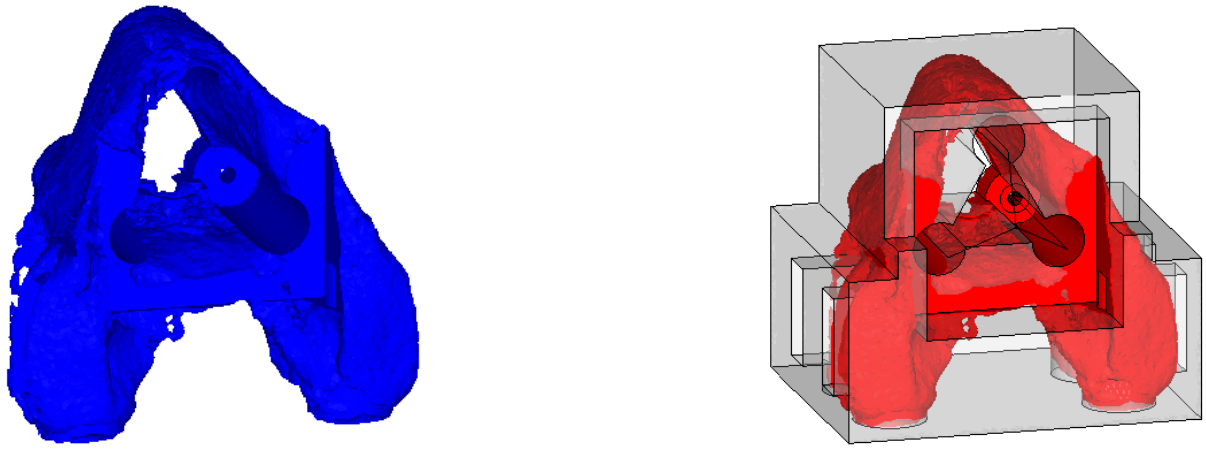

(a) (b)

Figure 4.25: Optimization topology results - phase 3 - design b.

4.5.4 Optimization cycle conclusions

A summary of the optimization cycle characteristics is presented in table 4.8 and the model topology evolution and mass evolution along the optimization cycle is presented in figure 4.26 and 4.27, respectively.

Based on table 4.8 and figure 4.27, it is possible to conclude that the mass of the structure is becoming smaller during the several phases except for the design 3b, as expected. However, as explained in section 4.5.3, this design does not bring any advantage in terms of geometry that could be more valuable than the mass reduction of the structure. So, the final design is the 3a. This design is the lighter one, but it is also fully operational as suggested by the decisions about the design space in section 4.5.3. By analyzing table 4.8, it is also possible to see that the CPU time significantly increases with the number of elements, as expected. However, the number of iterations doesn't appear to have any relation with the other parameters.

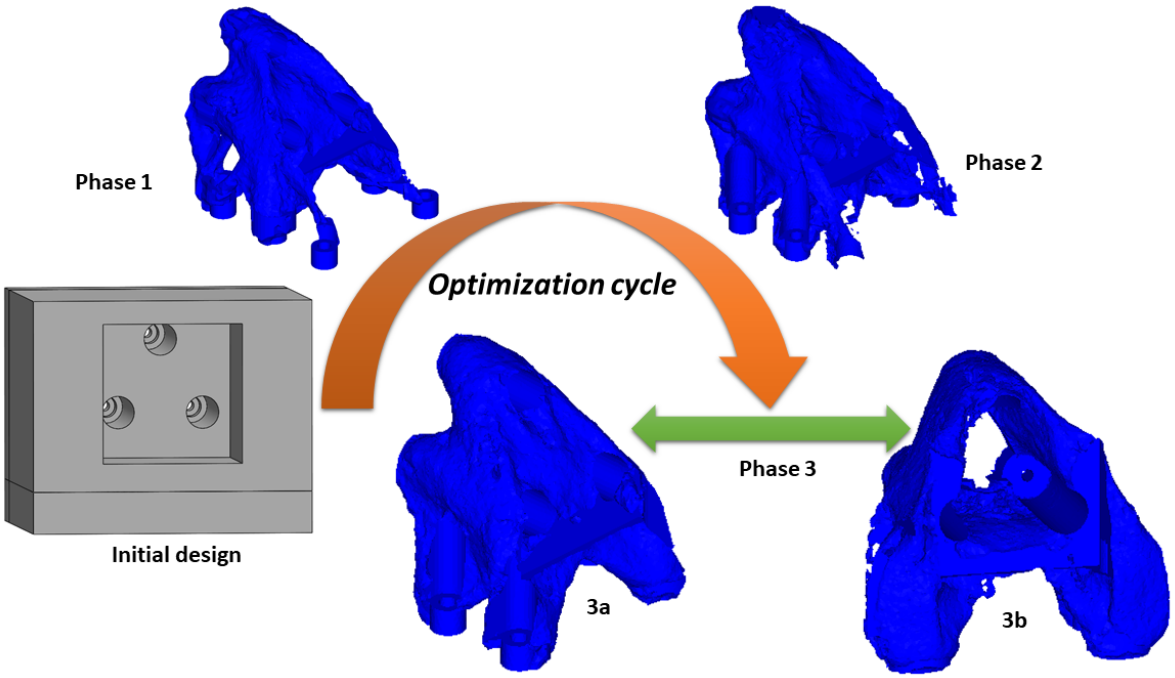

Figure 4.26: Optimization cycle.

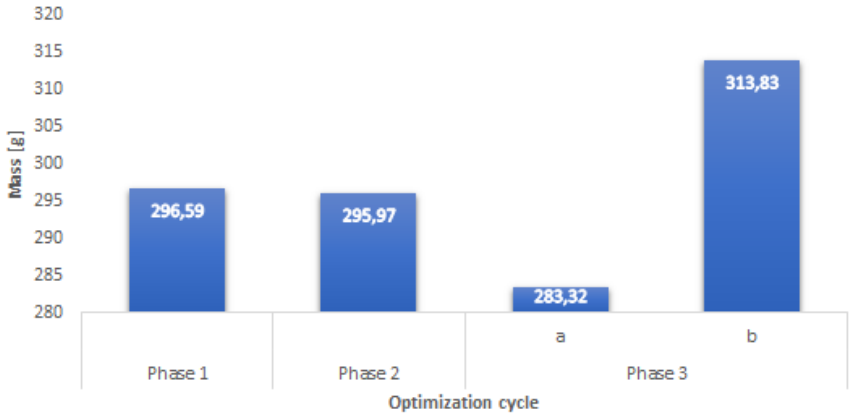

Figure 4.27: Optimized model mass evolution.

Table 4.8: Optimization cycle characteristics.

		No. of elements	No. iterations	CPU time [hh:mm:ss]	Frequency [Hz]	Mass [g]
Phase 1		1222022	142	49:00:16	392.63	296.59
Phase 2		635992	182	12:57:43	373.00	295.97
Phase 3	*a*	1009736	348	46:19:52	359.95	283.32
	b	955885	276	25:00:46	353.78	313.83

4.6 Optimized structure CAD modelling

Optistruct software possess a post processing tool called “OSSmooth” which allows the smoothing and exporting of an optimized design in several formats. So, after the decision about which design shall be used, this tool was used to smooth the geometry and export the 3a design in a “STEP” (Standard for

the Exchange of Product Data) format so it could be imported in Solidworks (student version 2016). The imported structure can be seen in figure 4.28.

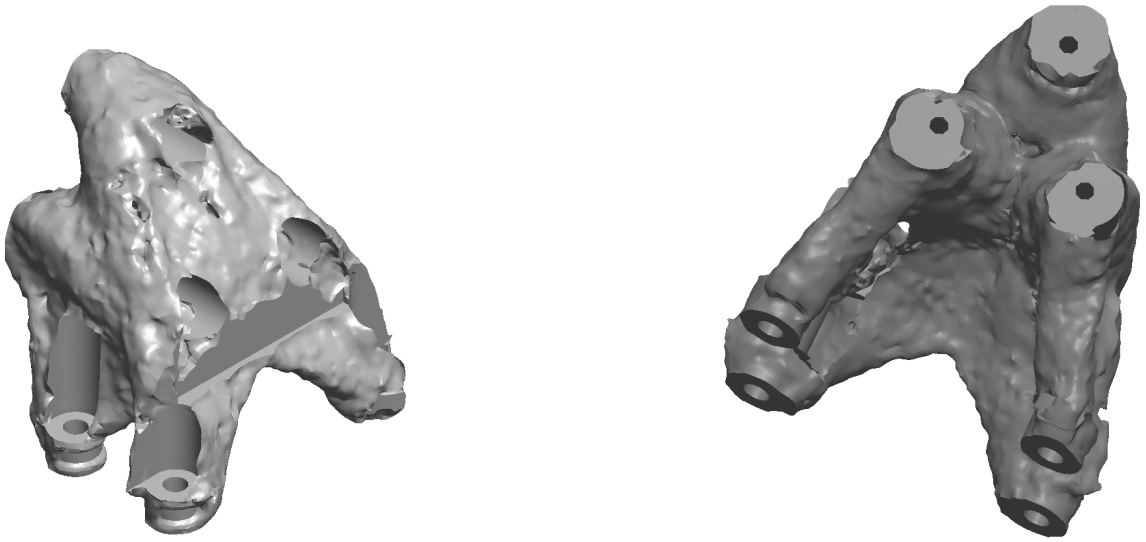

(a) (b)

Figure 4.28: Imported 3a design to Solidworks.

The modelling of the structure was based in the imported design with some adjustments to simplify the geometry. It is important to simplify the geometry since what cames from the optimization is a conceptual design and it needs to be adapted to decrease some post processing dificulties like support structures which can arise from overhangs or to avoid fragile narrow structures. It is also important to simplify the model to create a geometry that could be meshed for the further re-analysis of the structure without using an excessively refined mesh. The obtained geometry can be seen in figure 4.29 where it's possible to see that the structure is very similar to the imported 3a design, as supposed. It is also possible to see, in figure 4.30, that the design is fully operational, as expected.

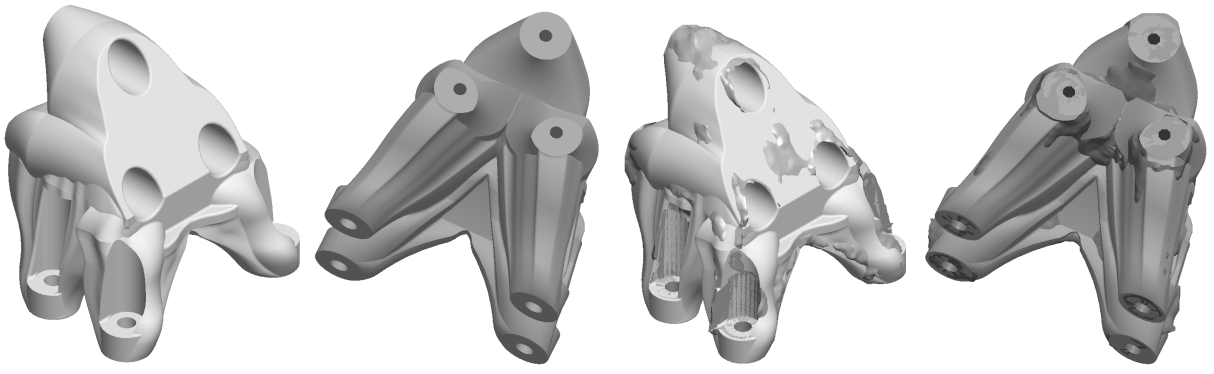

(a) (b) (c) (d)

Figure 4.29: Final polymer design (a and b) vs Final polymer design comparison with 3a imported design (c and d).

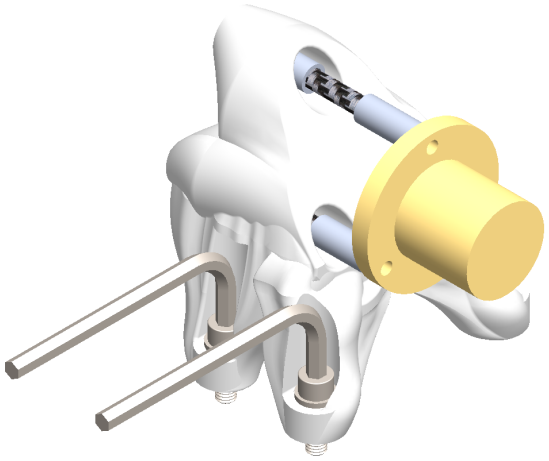

Figure 4.30: Fully operational assembly.

4.7 Optimized structure analysis

To verify that the new polymer model from section 4.6 satisfies the initial requirements, an analysis shall be performed to assess its current performance. The numerical model was developed exactly in the same way as before in section 4.3. The connection tubes were modelled as rigid elements since its materials' Young's modulus values are one order of magnitude higher than the interface structure's material. Tetra mesh characteristics for the model (figure 4.31):

- Total number of elements: 897753
- Global element size: 2mm
- Worst jacobian: 1
- Worst aspect ratio: 5.65 in 573 of 897753 which is meaningless (≈0.00%)

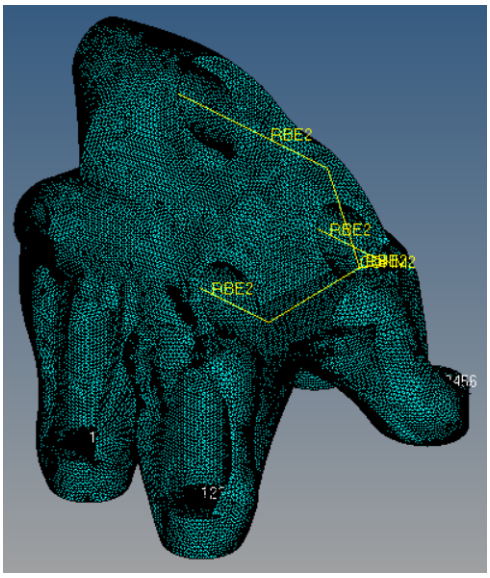

Figure 4.31: Optimized design numerical model.

The analysis results are depicted in table 4.9 and figure 4.32. It is possible to see that the first mode frequency is 400.92Hz which satisfies the optimization constraint of 350Hz. However, this also proves that the structure could be lighter since this frequency value can be reduced. The only way to do this is to iterate the CAD modelling with some slight changes and analyze each one of them until the "true optimum" is achieved. This is not an exact method and therefore, this design was accepted by the author since the main objective of this one is to validate the optimization approach which until now is going as supposed. The maximum present stress value of 0.154MPa is also smaller than the 10.32MPa calculated in section 4.4. Besides, using the same FEM model but without the hardware system, the first mode frequency of the interface structure alone was also calculated with a frequency value of 947.42Hz.

Table 4.9: Optimized polymer design - analysis results.

Variables of interest	Results
1st mode frequency [Hz]	400.92
Maximum present stress [MPa]	1.54e-01

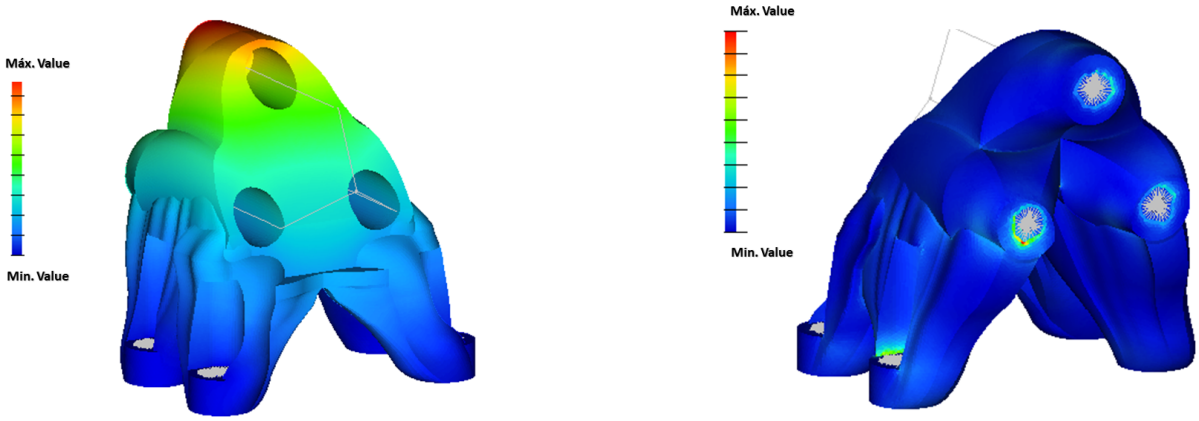

(a) Modal analysis.

(b) Static analysis: Stress results.

Figure 4.32: Optimized polymer design - analysis results.

4.8 Optimized structure experimental validation

4.8.1 Objective

The experimental activity aims to validate the numerical model and with that, validate the optimization approach used in the designed structure. The interface structure's and assembly's first mode frequency will be assessed through an experimental test in a shaker and if the real frequency value is similar to the theoretical one, the model and the optimization approach are validated.

4.8.2 Description

The hardware system was simulated through a CAD model (figure 4.33a) developed by the author with the same characteristics (geometry, materials and weight) in order to avoid the usage of a highly cost

product during the experiments. The real assembly was manufactured by the author and can be seen in figure 4.33b. The aluminum inserts and the brass part were obtained through turning, drilling, threading and milling processes of round profiles while the carbon tubes were bought with tube section and cut. Some pictures from the raw material and their manufacturing are shown in figure 4.34. The carbon tubes were glued to the aluminum inserts with a structural adhesive: *DP 810* from *3M* (figure 4.34d). The aluminum, brass and carbon fiber tubes properties are depicted in table 4.10.

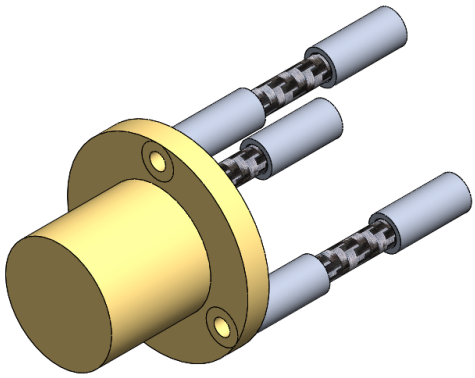

(a) CAD model.

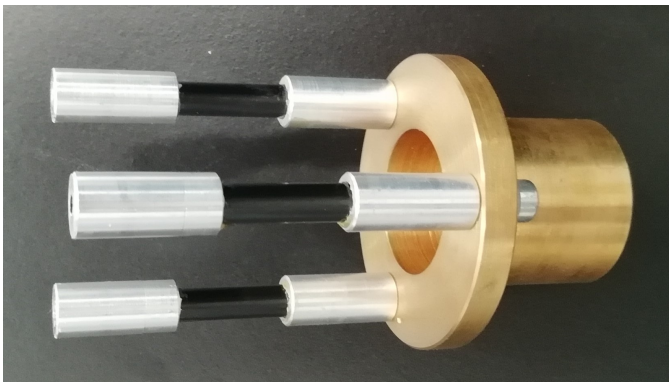

(b) Real model.

Figure 4.33: Hardware system.

(a) Raw material.

(b) Brass part milling.

(c) Tubes in parts.

(d) Structural adhesive.

Figure 4.34: Some pictures from hardware system manufacturing process.

Table 4.10: Material's properties for hardware system.

	Aluminum	Brass	Carbon fiber
σ_y *[MPa]*	255	135	1470
E *[GPa]*	69	96	90
ν	0.33	0.35	0.2
$\rho\,[Kg/m^3]$	2400	8250	1600

The test specimen was produced using the same production process explained in appendix C. However, for this one, its printing orientation was chosen to make the production as quick as possible and to use the minimum possible support material in order reduce its production cost. Figure 4.35 illustrates the specimen orientation and figure 4.36 shows the final product and respective assembly.

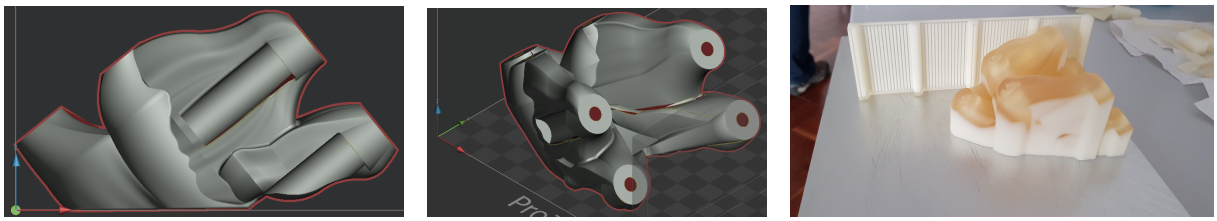

(a) (b) (c)

Figure 4.35: Specimen's printing orientation.

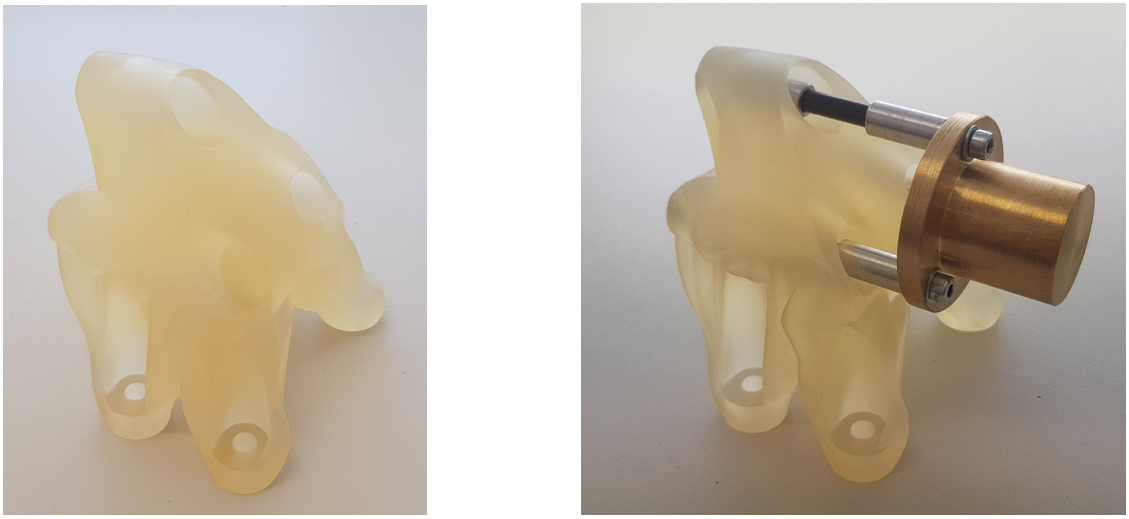

(a) Interface structure - polymer. (b) Assembly - polymer.

Figure 4.36: Final polymer product.

The test specimen is excited in the *Active Space Technologies* facilities shaker with the input function shown in equation 4.4 where a is the acceleration, ω is the angular frequency and t is the time. In order to assess the specimen dynamic response and to control the shaker behaviour, two piezo-electric accelerometers are used: an accelerometer over the specimen (Type 4513-B [96]) and another over the shaker base (Type 4520-001 [96]). The accelerometer in the shaker base only measures data in one direction since it is enough to control its translational input. Both accelerometers are fixed with the same method: A tape is glued to the accelerometer and another tape is glued to the specimen/shaker base and then, a *Loctite* general glue is used to glue one tape to the other. This is a good practice to

avoid any damage from the glue in the accelerometers or in the tested parts as well as all the trouble of cleaning the glue from a sensitive sensor as the accelerometer. In this specific case, the glue could have a significant destructive effect over the polymer in case of direct contact. The experimental setup can be seen in figure 4.37.

$$F(a, \omega, t) = a \cdot \sin(\omega t) \tag{4.4}$$

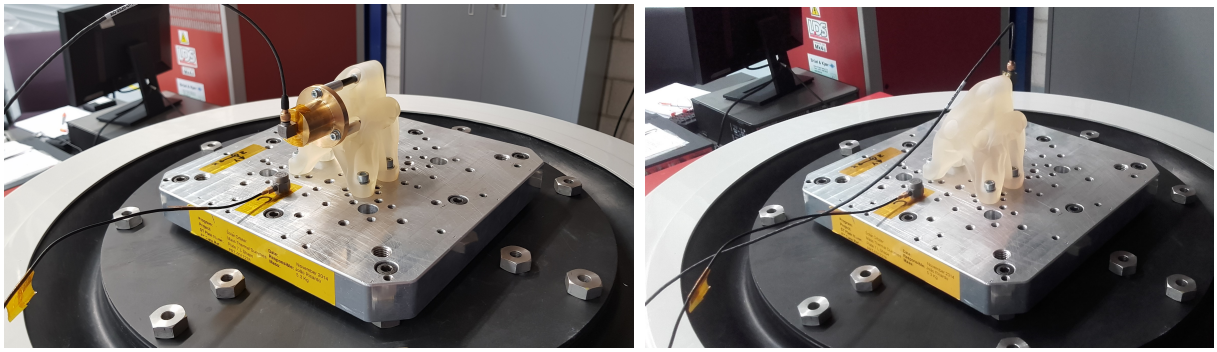

(a) Assembly. (b) Interface structure.

Figure 4.37: Experimental setup.

Software *Shaker Control - version 9.0* is used to monitor, control and acquire the data from the experiment. The obtained results for the assembly and the interface structure alone are shown in figure 4.38 and 4.39, respectively. Both graphics have 5 series of data and use a logarithmic scale for the vertical axis. The **Input profile (F)** is the input function which was already explained before as well as its amplitude value (acceleration). The **Control accelerometer** is the data from the accelerometer on the shaker's base. As expected, its values are almost equal to the ones of the **Input profile (F)** and that's why it is not possible to see both in the graphics. The **Accelerometer_X**, **Accelerometer_Y** and **Accelerometer_Z** are the data from the 3 axis of the accelerometer on the specimen.

The z axis is the perpendicular one to the shaker's base and by knowing that, figure 4.38 shows that the first and third registered mode shapes are highly related with bending in z direction while the second one has bending in two directions being x direction the predominant one (x axis is oriented from the interface structure to the hardware system). This behaviour was also observed by the author in the animated analysis results as shown in the animated figures D.2 and D.3 in appendix D which gives confidence about the numerical model accuracy (the animated figures are already from the corrected model that will be explained further on). However, more modes were observed in the numerical model within this frequency spectrum. The author put the accelerometers in the specimen's zone that have more displacement during the first mode shape in the numerical model in order to achieve an accurate measurement for that one. It is normal that some modes don't appear since they don't have enough energy in that spot. For the interface structure, only one mode was observed in the experiment and that one also coincides with the first mode observed in the numerical model (animated figure D.4).

The relative difference between the experiment and numerical model results for the assembly and interface structure are depicted in table 4.11.

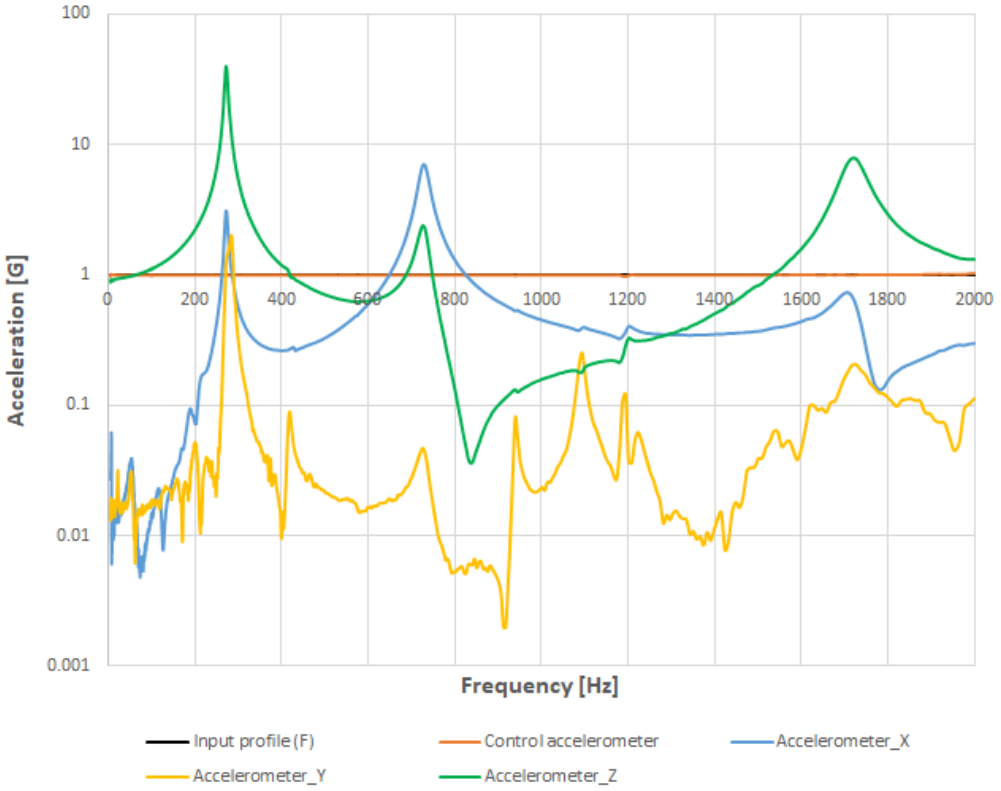

Figure 4.38: Assembly experimental results.

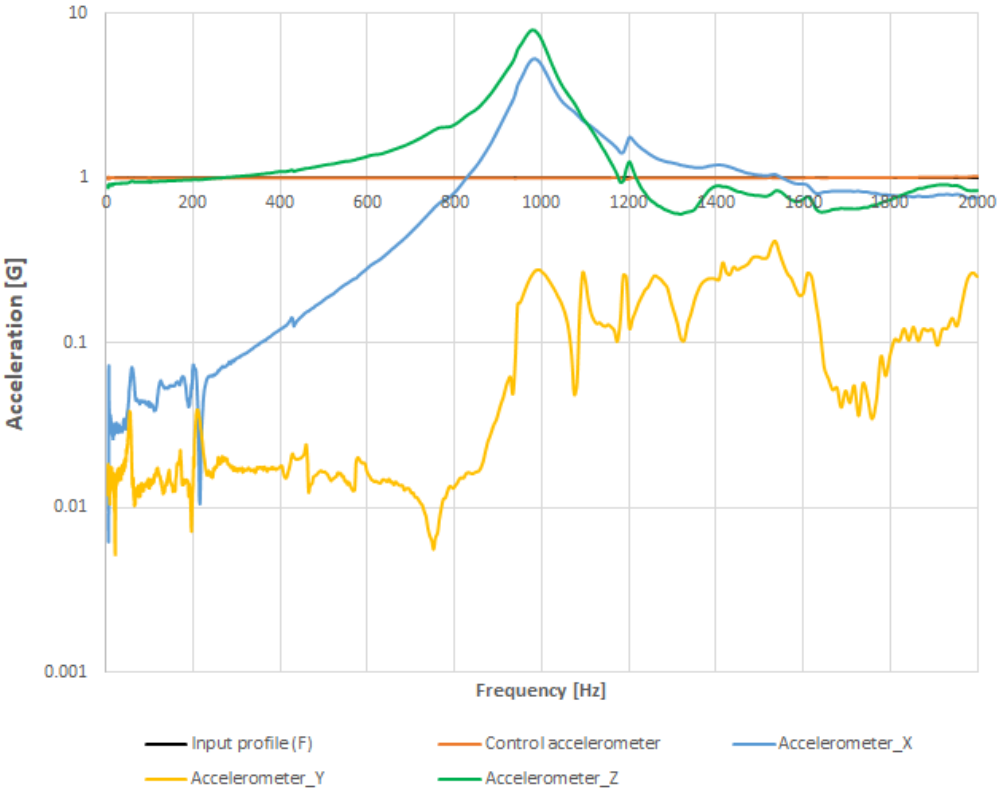

Figure 4.39: Interface structure experimental results.

Table 4.11: Numerical and experimental results comparison.

	Numerical model 1st mode frequency [Hz]	**Experimental test 1st mode frequency [Hz]**	**Relative error**
Assembly	400.92	271.44	47.70%
Interface structure	947.42	978.82	3.21%

The assembly's relative error is almost 50% which shows that there is some error in the numerical model. Since the interface structure results had an acceptable error (smaller than 10%) which confirms the model and the material approach developed before, a direct conclusion is that the problem is in the stiffness of the hardware system part. This one was excessively stiff in the numerical model. By knowing this, a new FEM model was develop using exactly the same approach than the previous model but with two significant changes:

- The linkage tubes are modelled as CBAR elements as done in section 2.2;
- The hardware structure is modelled as a 3D part with Tetra elements (figure 4.40) instead of the CONM2 mass element. This is done to take into account its inertia.

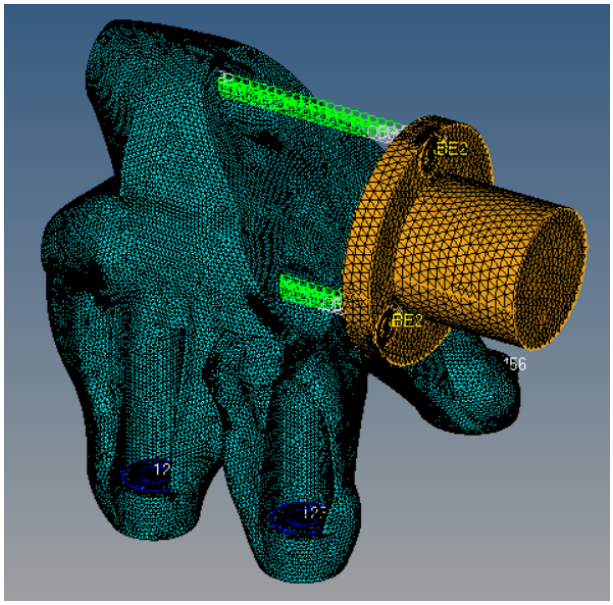

Figure 4.40: Modified FEM model.

The new comparison between the numerical and experimental results for the assembly can be seen in table 4.12. It is possible to see that this implementation was a success since the new error value is also acceptable. The small errors in the assembly and structures results are probably caused by some error during the manufacturing or by the glue's stiffness contribution. However, the author thinks that this simplified model (without the glue) is suitable for the application. Besides, the errors can also be caused by the lack of precision during the bolts tightening since an Allen's wrench was used instead of a torque wrench.

Table 4.12: Numerical and experimental results comparison after correction.

	Numerical model 1st mode frequency [Hz]	Experimental test 1st mode frequency [Hz]	Relative error
Assembly	282.73	271.44	4.16%

A simple sensitivity analysis was develop in order to increase the knowledge about the numerical approximations influence over the results in this problem. An analysis is developed over two more models with the same initial model characteristics but with one significant difference. The 4 used models and respective differences are:

- Model 1 - Initial model with CONM2 and RBE2 elements;
- Model 2 - Similar to initial model but with CBAR elements;
- Model 3 - Similar to initial model but with 3D hardware structure;
- Model 4 - Similar to initial model but with 3D hardware structure and CBAR elements.

As expected, figure 4.41 shows that model 1 is the stiffest one, model 4 is the one with less stiffness and model 2 and 3 are intermediary ones. However, it is also possible to see that model 3 is stiffer than model 2 which induces higher influence from the CBAR elements over the model results than the 3D hardware structure. Besides, the 3D hardware system inertia influence is dependent from the tubes stiffness as shown by the significant decrease in the frequency value of model 4 when compared to model 2 and 3. This make sense due to the increase in the hardware structure's displacement. It is important to mention that even knowing that the CBAR has more influence, both changes have a significant influence in the model's accuracy.

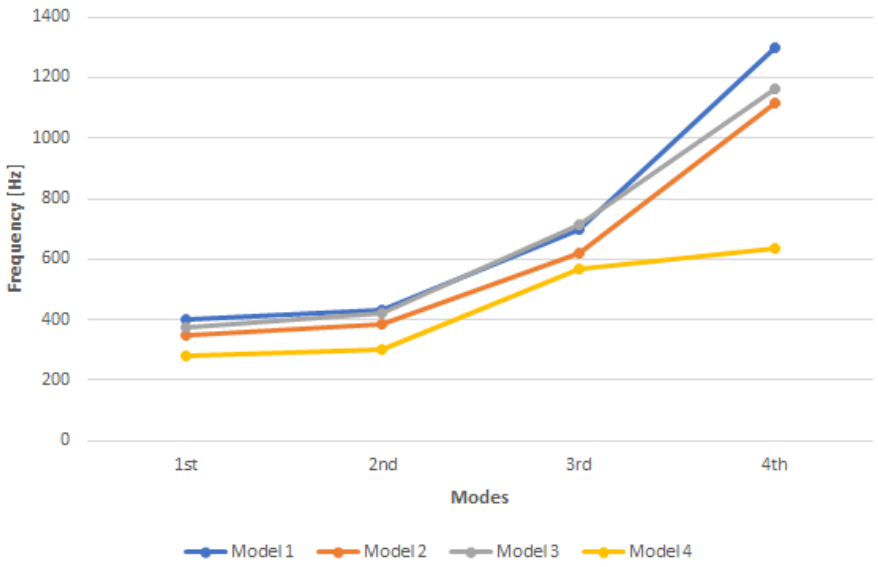

Figure 4.41: Sensitivity analysis.

4.8.3 Experimental validation remarks

In order to correct and validate the numerical model, the experimental activity allowed a correlation between this one and the real one. Due to the correction made to the numerical model, it now complies with the reality which made this activity a success since from now on, the optimization approach and design are validated for this type of problem.

Although the author had used the CBAR elements at section 2.2 for the metal design, his approximation with the RBE2 elements for the polymer design (which is significantly less stiff) was wrong. This shows how much influence the linkage tubes have over the hardware system dynamic response and why they should be designed very carefully. Besides, since the inertia values of the hardware system were 2 orders of magnitude below the inertia values of the interface structure, its values were neglected and a non-structural mass was used instead. This approximation was also too rough and this experiment showed it. This activity was also a success due to the produced knowledge and sensitivity to this type of problems.

Chapter 5

Final metal structure

5.1 Materials and 3D printing technique choice

Now that the optimization approach is validated, the final metal structure design can be developed with this methodology in order to assess the theoretical feasibility of a new interface structure solution developed with TO and AM. For that, the first step is to do a proper choice of the AM process to be used. A qualitative assessment of the principal AM processes in metals is developed in table 5.1.

From table 5.1 it is possible to conclude:

- UAM – Ultrasonic additive manufacturing is not a good choice because it is a hybrid process which will have a significant waste of material due to the subtractive part. Furthermore, the material's properties would be dependent of the lamination orientation – orthotropic material;

- Binder Jetting is not a good choice due to bad mechanical properties and its poor accuracy;

- Laser Engineered Net Shaping (LENS) cannot be used too because it is hard to produce small scale features and complex geometries due to the pre-positioning of the deposition arm during the process. In this interface structure, a relative complex geometry with small scale features is expected from the experience with the polymer case;

- The three PBF methods are valid candidates for the manufacturing process.

Altough the material needs to be an aluminum alloy as defined in the problem requirements in section 1.2, an assessment to the several options will be done to know if an aluminum alloy is the most suitable or not for this problem. Therefore, a market search is performed to evaluate the existing materials offers for these processes as well as their properties. Although it is possible to find several materials already available with this technologies like stainless steels, precious metals, aluminum alloys, nickel alloys, chromium alloys, cobalt alloys, titanium alloys, etc; the ones that could be of interest for the aerospace industry are summarized in table 5.2.

Table 5.1: Qualitative assessment of AM processes in metals, [55, 58, 59] and [62].

		Advantages	Disadvantages
PBF	*EBM*	• Production is under vacuum - no contamination of powder • Density up to 99.9% • Less necessity of support structures • Low thermal gradients - no thermal issues • Fast building rates • Possibility to stack a lot of parts in the build tank	• Not so good accuracy and surface roughness as SLM or DMLS • Limitations for lattice structures due to accuracy
	SLM	• Density up to 99.9% • Good accuracy • Good surface roughness • Possible to use a lot of different metals • Possibility to create very fine lattice structures • Possibility to create inner channels	• Supports to prevent warping and distortion - post processing expensive and time consuming • Thermal treatment for residual stresses • Very slow process
	DMLS	• Density up to 99.9% • Good accuracy • Good surface roughness • Possible to use a lot of different metals • Possibility to create very fine lattice structures • Possibility to create inner channels	• Supports to prevent warping and distortion - post processing expensive and time consuming • Thermal treatment for residual stresses • Very slow process
DED	*LENS*	• Fast building rates • Possibility to use with a lot of different metals • Position and orientation of laser beam to powder stream is independent - same properties in horizontal and vertical directions • If material platform could be tilted - no supports • Suitable for repairing and adding activities	• Cannot produce small scale features • Limited product geometry • Huge surface roughness • Poor accuracy - machining in post processing • Support material - post processing expensive and time consuming • Residual stresses - Heat treatment
Sheet Lamination	*UAM*	• Fast building rates • Doesn't need post processing • Doesn’t need support structures • Doesn't have thermal issues • Very flexible in terms of structure	• Hybrid process - waste of material • Material is directional dependent • Low surface quality
Binder Jetting		• Fast building rates • No thermal problems • Doesn't need supports • Give colors directly • Design and process freedom	• Doesn't guarantee good material properties - low strength • Poor accuracy

Table 5.2: Available materials for each process, [59, 97–101].

	PBF		
	EBM	DMLS	SLM
Titanium	Ti6Al4V grade 2	Ti6Al4V grade 2	Ti6Al4V grade 2
	Ti6Al4V grade 5	Ti6Al4V grade 5	Ti6Al4V grade 5
	Ti6Al4V grade 23	Ti6Al4V grade 23	Ti6Al4V grade 23
Nickel	-	IN 625	IN 625
		IN 718	IN 718
		Hastelloy X	IN 939
		-	Hastelloy X
Aluminum	-	AlSi10Mg	AlSi10Mg
		-	AlSi12
			AlSi7Mg0.6
			AlSi9Cu3

Following the materials' datasheets from the suppliers, table 5.3 was developed to compare the different options through an assessment of the ratio between properties of interest. All the data presented is related with the chosen machine and respective company. Although there is not a significant difference in most of cases, using a different machine from the catalogue of the same company would result in different material's properties. Therefore, the presented data is from the materials with the higher values for Young's modulus and yield strength since the density typically does not change.

The majority of the materials have a slightly difference between their properties in the horizontal direction (2D layer plane) and the vertical direction (deposition direction). So, an average value was used for this comparison. Figure 5.1 presents table 5.3 data in a bar chart to facilitate its analysis from where it's possible to conclude that:

- Ti6Al4V grade 5 and Ti6Al4V grade 23 have significant higher ratios than the other materials in terms of yield strength;
- Ti6Al4V grade 5 and Ti6Al4V grade 23 have higher ratios than the other materials in terms of Young's modulus, except for AlSi10Mg produced with SLM technique;
- Ti6Al4V grade 5 and Ti6Al4V grade 23 show similar ratios for different companies and different techniques which is a valuable feedback in terms of reliability of the results. This reliability was expected, and it is also introduced by literature [102, 103] since these materials have been used by the aerospace industry for a long time and are currently being used by the motorsport industry too;

All these conclusion points suggest a choice between Ti6Al4V grade 5 and Ti6Al4V grade 23. The essential difference between them is the reduction of oxygen content to a maximum of 0.13% in grade 23. This confers improved ductility and fracture toughness with some strength reduction. Although grade 23 has less strength, its improvements are important for fatigue issues which makes it more suitable than grade 5. However, the choice of the most suitable material must also be based in the active constraints of

the optimization cycle. Based in the experience from section 4.5.1, the material's stiffness will have more influence over this design. So, the choice for the material is AlSi10Mg produced with SLM technique from Concept Laser [99]. During section 5.3 this choice will be confirmed due to the low present stress values. The AlSi10Mg properties are shown in table 5.4.

Table 5.3: Materials' properties ratios.

		Density [g/cm^3]	Young's modulus/Density average ratio [GPa.cm^3/g]	Yield Strength/Density average ratio [Mpa.cm^3/g]
EBM	*Ti6Al4V grade 2*	4.51	26.61	119.73
	Ti6Al4V grade 5	4.42	27.15	214.93
	Ti6Al4V grade 23	4.43	27.09	209.93
DMLS	*Ti6Al4V grade 2*	4.50	26.67	124.44
	Ti6Al4V grade 5	4.41	27.21	249.43
	Ti6Al4V grade 23	4.41	27.21	260.77
	IN 625	8.40	18.45	79.76
	IN 718	8.15	20.25	86.75
	Hastelloy X	8.20	22.56	71.65
	AlSi10Mg	2.67	27.15	95.51
SLM	*Ti6Al4V grade 2*	4.51	24.39	121.95
	Ti6Al4V grade 5	4.42	26.02	245.48
	Ti6Al4V grade 23	4.43	26.64	243.79
	IN 625	8.40	23.81	81.79
	IN 718	8.15	24.54	120.12
	IN 939	8.17	21.66	89.96
	Hastelloy X	8.20	19.76	72.56
	AlSi10Mg	2.67	28.09	77.90
	AlSi12	2.65	25.47	103.77
	AlSi7Mg0.6	2.65	22.26	79.62
	AlSi9Cu3	2.75	20.73	85.82

Table 5.4: AlSi10Mg properties.

ρ *[g/cm^3)]*	2.67
ν	0.33
σ_y *[MPa]*	208.00
E *[GPa]*	75.00

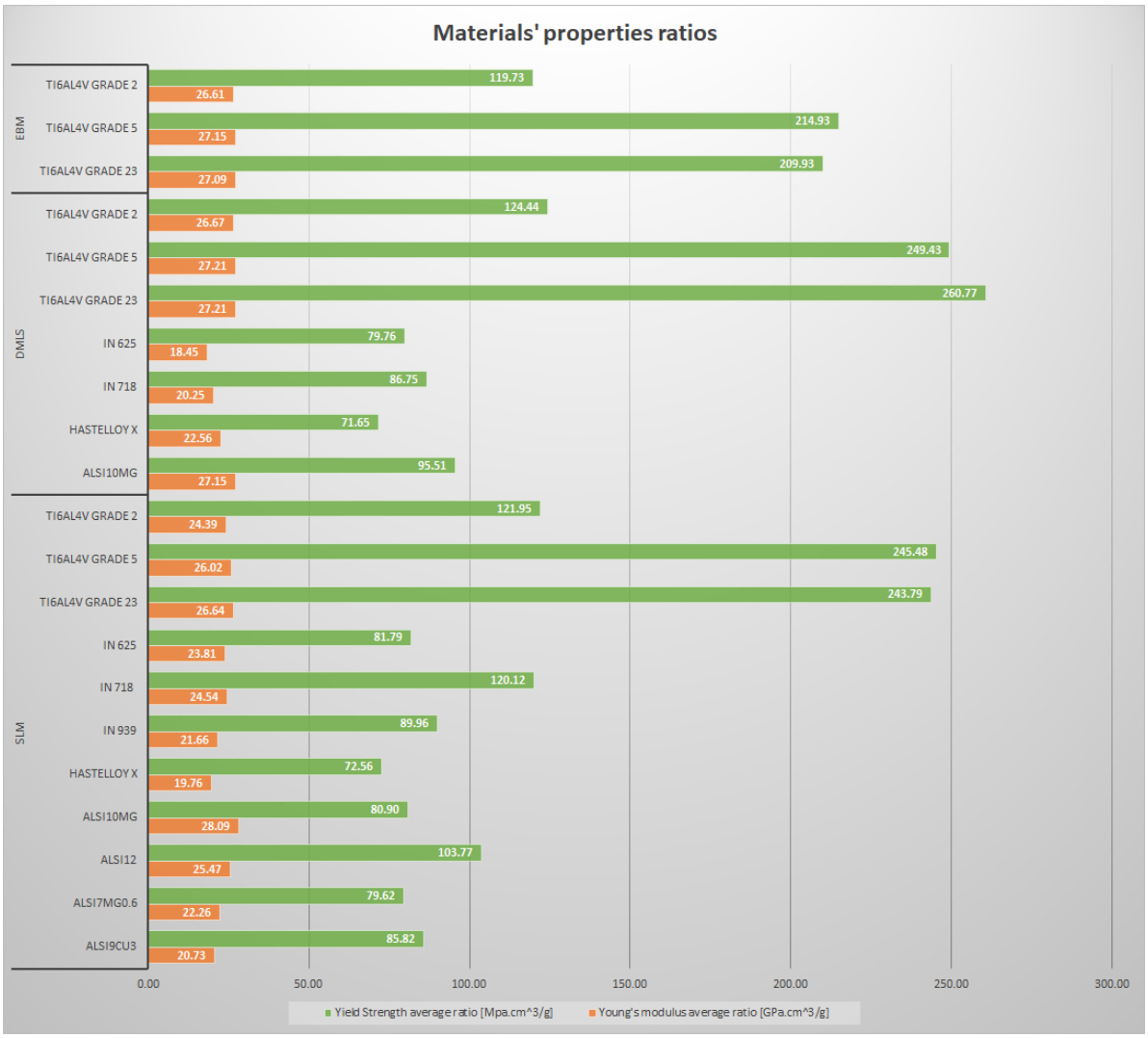

Figure 5.1: Materials' properties ratios.

Crucial factors as the cost of the aluminum alloy powder and titanium alloy powder together with the cost of the post-processing shall be considered as well as the cost of the 3D printing machine and its variability of available working materials. For instance, EBM technique doesn't have so many available materials as SLM or DMLS techniques. All these and others cost and management factors shall be considered by the company although they are out of the scope of this thesis. So, for the material's choice, the only thing that was considered was the most suitable mechanical properties to fulfill the structure's requirements.

5.2 Numerical optimization cycle

Based on the previous optimizations in section 4.5 and the structure requirements, the optimization parameters were defined. The material properties are adapted for the new material used and the minimum initial density, convergence value and penalization factor are the same as used before. Besides, the maximum accuracy of the machine is not known since the supplier does not deliver that data. So, a

minimum dimension constraint of 0.5mm will be used as before. The FEM model that will be used is the same with some differences in the design space that will be explained further. The optimization parameters are resumed in table 5.5. It is also important to mention that now, the base load case value for the static analysis is 60G again as defined in section 2.2.

Table 5.5: Optimization model parameters – final structure.

E_0	75.00 GPa
x_{min}	0.001 Kg/m^3
p	3
ν	0.33
Conv.Val	$<$0.005
Dimension constraint	$\geq$ 0.5 mm
Frequency constraint	$>$2500 Hz

The final topology was achieved through an optimization cycle composed by 2 phases that will be described in section 5.2.1 and 5.2.2.

5.2.1 Optimization cycle - phase 1

Besides the already explained model characteristics, the rest of the FEM model used in this phase is equal to the one in section 4.5.2. The objective was to verify if the metal structure needs the 6 bolts or not. For this phase, the necessary threshold value is 0.95 and the respective design can be seen in figure 5.2. The frequency value achieved is 2585.59Hz which meets the requirement.

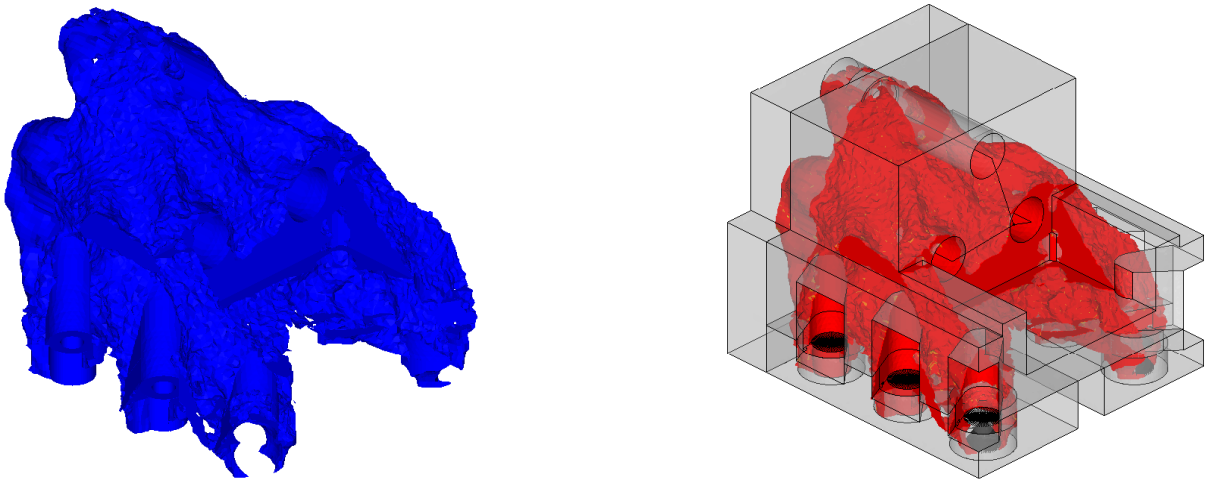

(a) (b)

Figure 5.2: Optimization topology results for the final structure - phase 1.

From the obtained results, it is possible to conclude that the two front bolts are necessary since they have a significant continuity in the material to the rest of the structure. Besides, it is also possible to see some lack of design space freedom. This will be corrected in the next phase. As expected, the topology is similar to the one obtained during the polymer optimization.

5.2.2 Optimization cycle - phase 2

The design space will suffer big changes in this phase. Based in section 5.2.1 results and conclusions and in the mandatory necessity of use a torque wrench in the metal design, the design space needs to be expanded to its maximum outside dimensions as in section 4.3. A significant amount of the design space will be required by the torque wrench. The new design space can be seen in figure 5.3.

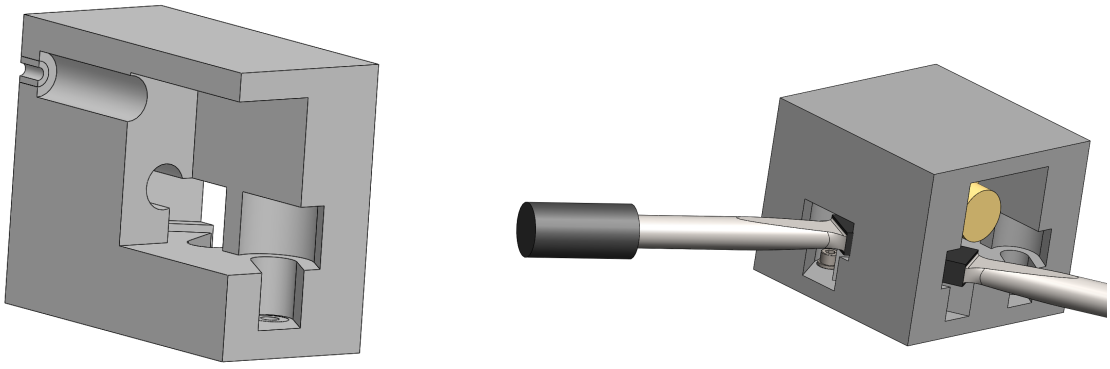

(a) Design space section cut.

(b) Necessary space for torque wrench.

Figure 5.3: Design space for the final structure - phase 2.

The torque wrench and the socket insert were modelled using as base Würth [104, 105]. For the front bolts, the open space for the wrench tries to use the open space for the hardware system mounting to cut the minimum material as possible. Besides, these cuts to the front part also coincide with the areas with less material in the previous optimized results. For the 4 rear bolts, the objective was to unite the tool working space two by two without using the middle part of the structure since it is the one that needs more material. By uniting their open space, it was necessary to cut less material than using individual working spaces.

The design freedom in this model is seriously compromised. So, an analysis to the full design space was developed to assess its current first mode frequency that has a value of 2351.38Hz. This already gives a hint that the optimization process probably won't work since the TO needs to increase the structure's stiffness and reduce its mass with a small "effective" design space available. By "effective" the author means the design space that significantly contributes to the structure's stiffness with a low mass cost.

As expected, in this phase, the optimization converged to an infeasible design. However, a design concept could be extracted as shown in figure 5.4.

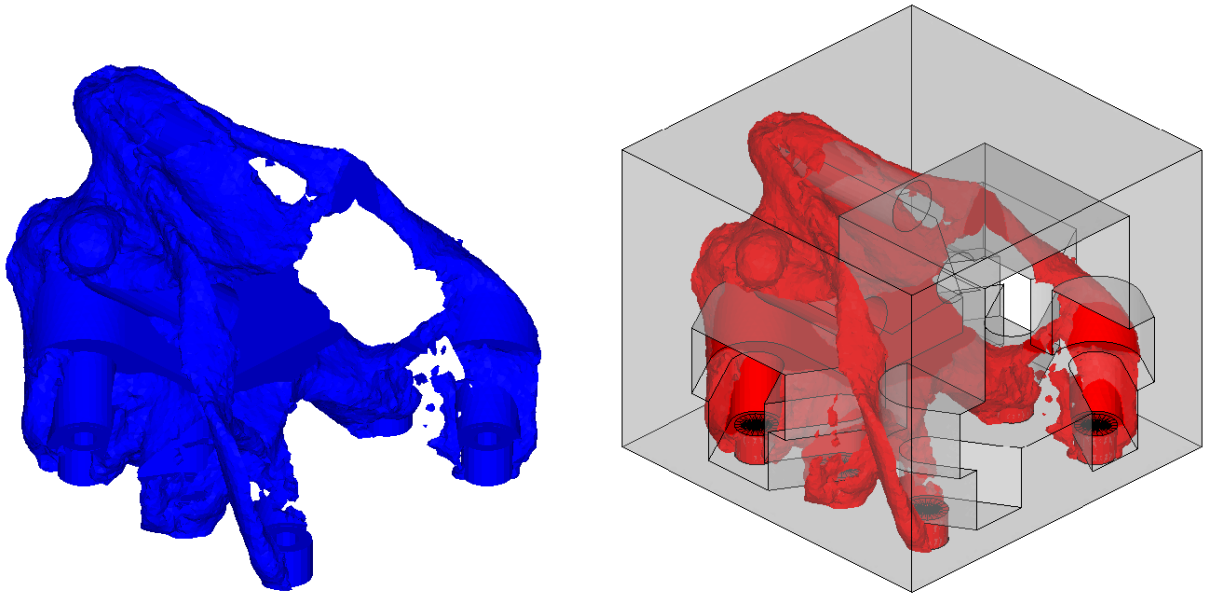

(a) (b)

Figure 5.4: Optimization topology results for the final metal structure - phase 2.

5.2.3 Optimization cycle conclusions

A summary of the optimization cycle characteristics is presented in table 5.6. The frequency value for phase 2 is not shown since the optimization did not converge to a feasible design. However, the topology concept from this phase will be the base of the structure's CAD modelling. It is important to note that during phase 2, the violated constraint is the frequency constraint. But, this constraint of 2500Hz is applied to the assembly's first mode and not to the interface structure. As seen numerically on section 4.7 and experimentally on section 4.8.2, the interface structure first mode frequency is significantly higher than the assembly's one. So, this design concept can achieve the minimum necessary frequency with mass reduction when compared to the L-shape structure (2175.81g) as shown by the mass values in table 5.6.

Table 5.6: Optimization cycle characteristics.

	No. of elements	**No. of iterations**	**Frequency [Hz]**	**Mass [g]**
Phase 1	1222022	556	2585.59	710.72
Phase 2	1454085	181	-	621.31

Using the same process as before (section 4.6), the smoothed geometry was imported to Solidworks and the final structure model was designed. The imported geometry and the final design can be seen in figure 5.5 and 5.6, respectively. It is also possible to see, in figure 5.7, that the design is fully operational, as expected.

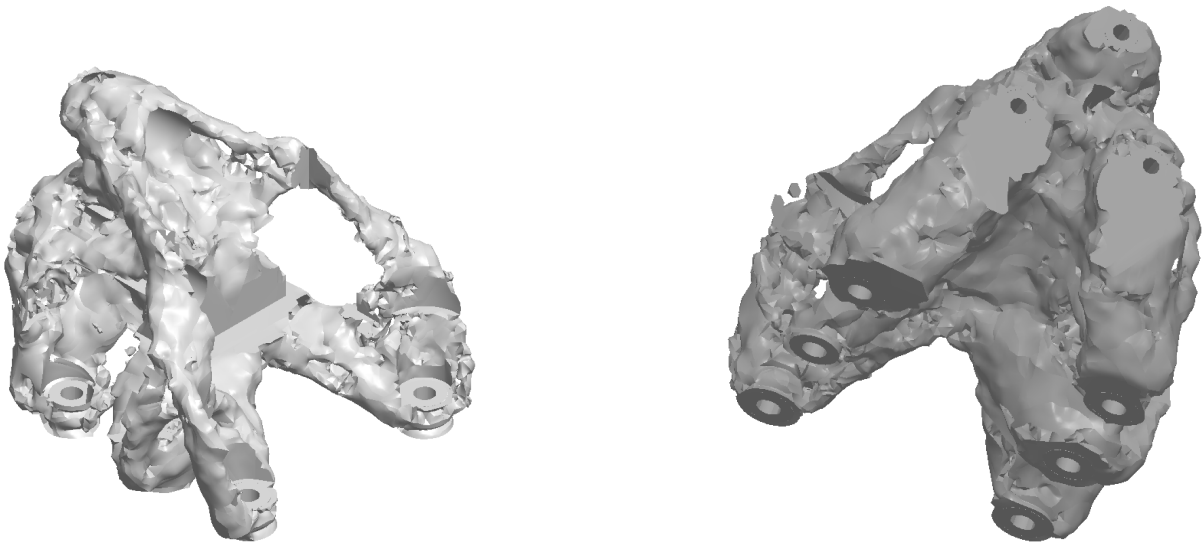

(a) (b)

Figure 5.5: Imported geometry to Solidworks.

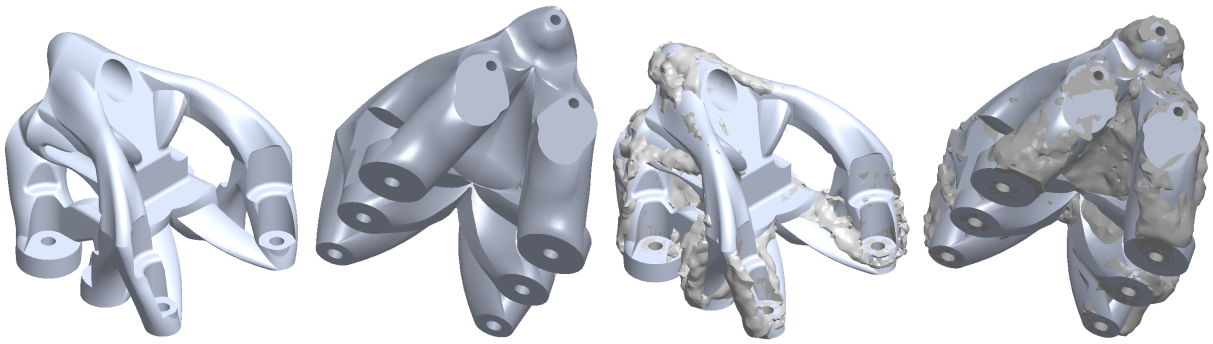

(a) (b) (c) (d)

Figure 5.6: Final structure design (a and b) vs Final structure design comparison with the imported geometry (c and d).

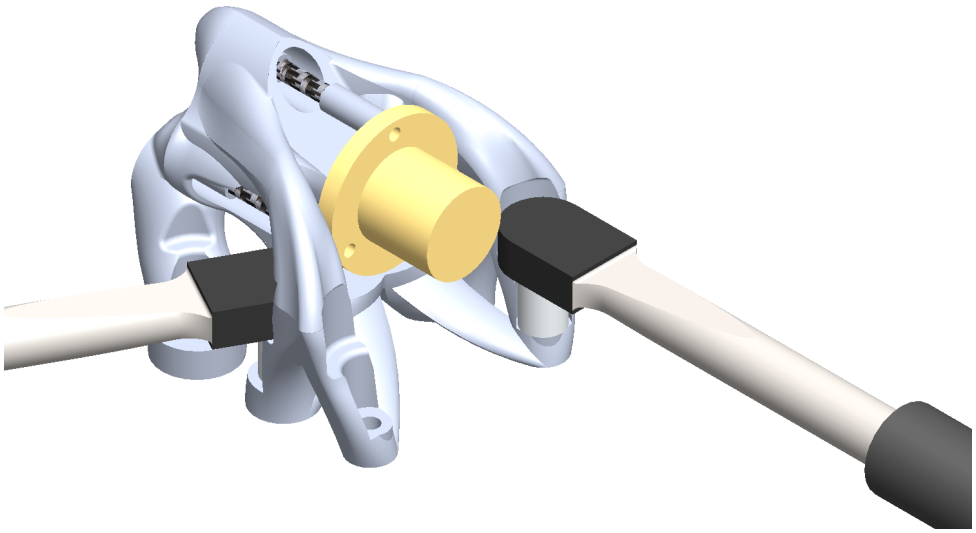

Figure 5.7: Fully operational assembly.

5.3 Optimized final structure analysis

To verify that the final metal structure satisfies the initial requirements, an analysis is performed to assess its current performance. The numerical model was developed exactly in the same way as the modified FEM model in section 4.8.2. The geometry complexity obligated the usage of a global element size of 0.2mm which is excessively refined for this problem. However, since it was just for an analysis, the author accepted this solution and its computational cost. The CPU time (hh:mm:ss format) during the assembly's and interface structure's analysis was 03:37:39 and 03:15:36, respectively. Tetra mesh characteristics for the model are:

- Total number of elements: 16760260
- Global element size: 0.2mm
- Worst jacobian: 1
- Worst aspect ratio: 409.68 in 6682 of 16760260 which is meaningless ($\approx$0.00%)

The analysis results are depicted in table 5.7. It is possible to see that the assembly's first mode frequency is 457.86Hz which does not satisfy the optimization constraint, as expected. The final structure first mode frequency is 2521.19Hz which satisfies the initial requirement of a minimum of 2500Hz. The stress was not taken into account during the optimization process but in this analysis, its maximum value is 20.31MPa which is not significant for fatigue issues. This is supported by Uzan et al. [106], since their results on figure 7 showed that the minimum value that was found as fatigue stress limit for this material was higher than 50MPa.

Table 5.7: Optimized final structure design - analysis results.

	1st mode frequency [Hz]
Assembly	457.86
Final structure	2521.19

5.4 Concluding remarks

The final structure optimization and design process were implemented with success since the structure fulfills the company's demands in terms of the first mode frequency and in terms of the used material. Besides, it is proved by figure 5.8 and animated figure D.5 in appendix D that the final structure does not influence the hardware system dynamic response, as supposed.

It is also of extreme importance to compare the L-shape structure solution to this optimized model as shown in table 5.8. Based in the results, it is possible to see that the first mode frequency of the final metal structure is 4.05% higher than the L-shape's one while the correspondent assembly's improvement is 9.14%. In terms of mass, a significant reduction of 75.72% was achieved. This makes the final metal structure stiffer, significantly lighter and capable of increasing the first mode frequency with the hardware system mounted.

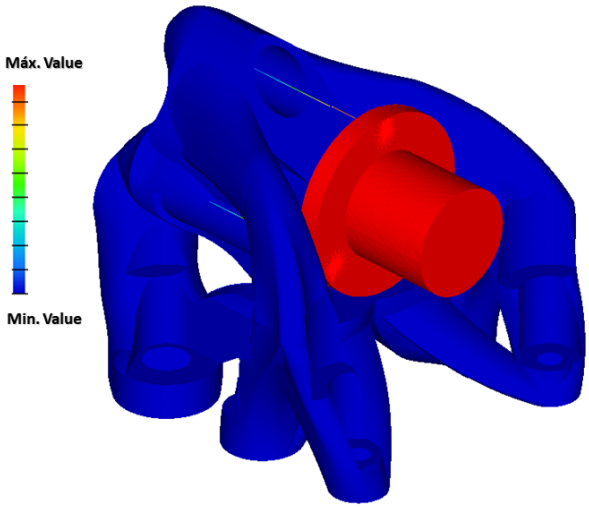

Figure 5.8: Final metal structure influence over hardware system's dynamic response.

Table 5.8: Final structure and L-shape comparison.

	L-shape	Final metal structure	Improvment	L-shape assembly	Final metal structure assembly	Improvment
Mass [g]	2175.81	528.21	-75.72%	-	-	-
1st mode frequency [Hz]	2423.14	2521.19	4.05%	419.51	457.86	9.14%

Chapter 6

Conclusions

6.1 Achievements

Along the thesis development, several objectives were achieved. The comparison between the Altair Optistruct, MSC Nastran SOL200 and Matlab's benchmark examples gave the opportunity to decide which of both commercial softwares is more suitable to this application. More important than that, this comparison also brought new knowledge and sensitivity to TO problems which allowed a different TO approach (not the typical one) for the interface structure optimization.

By using this new approach, an optimization cycle process was developed with several load cases and several optimization steps. Each step had important conclusions that converged to a lighter and operational design. A 3D printed polymer was used instead of a metal in order to produce a prototype and test it. The polymer was subjected to mechanical characterization tests that proved its isotropic behaviour in the elastic regime and the correspondent properties of interest. The 3D printed optimized part was produced, treated in post-processing and tested in *Active Space Technologies* shaker with success. The test results were correlated with the numerical model and after some corrections, the model was validated since an error of 4.16% and 3.21% were achieved for the assembly and interface structure, respectively. This experimental activity validated the TO methodology implemented.

The final metal interface structure was developed using the validated TO methodology where a significant improvement was achieved when this structure is compared to the company's L-shape current solution. An increment of 4.05% in the first mode frequency and a reduction of 75.72% in the mass makes this structure a better solution. The final metal structure complies with all the company's demands being important to refer its non-influence over the hardware system dynamic response and the increase of the assembly's first mode frequency when compared to the L-shape's one (increment of 9.14%).

This design success proved the advantageous relation between topological optimization and additive manufacturing due to its complex geometry. From now on, the develop methodology can also be used to design support structures for flight hardware.

6.2 Future Work

This work established an optimization and design process on which some future relevant improvements may be applied, such as:

- Characterization of the metal material and its optimized structure testing even though the optimization methodology is already validated. This is particularly important because metal structures typically needs significant post-processing processes as hot isostatic pressing (very common in SLM, for example) to achieve good properties and/or realise the residual stresses which can have significant influence in the structure's performance;
- Taking into account the AM procedures for metals during the design. Problems like enclosed voids or overhanging are not a problem in this design since it does not have enclosed voids and it is a PBF method. However, problems as the support material removal during the post-processing can happen and in this design, they probably need to be there to prevent warping and distortion during the manufacturing;
- The usage of lattice structures to simulate an element density. Lattice structures are known by their high stiffness and strength to low mass values [107]. 3D printing machines already have a very refined accuracy that enables the production of lattice structures precisely. So, the lattice structures shall be used to simulate an element density which is achieved by using a reference volume as density equal to 1 and then assuming different densities based on the percentage of used volume. After the TO, instead of choosing a threshold value and use all the elements above that value with the real density, the "real optimum" from the TO can be used with all the elements with their respective density simulated through lattice structures. This solution has a significant potential with the TO and AM relationship since the lattice geometry can also be manipulated to be more suitable to the specific problem's load case and its being currently studied by several engineers around the world [107–118].

Bibliography

[1] A. G. M. Michell. LVIII. The limits of economy of material in frame-structures. *The London, Edinburgh, and Dublin Philosophical Magazine and Journal of Science*, 8(47):589–597, 1904. doi: 10.1080/14786440409463229. URL https://doi.org/10.1080/14786440409463229.

[2] Data Physics. Satellite Qualification and Vibration Testing, February 2018. URL http://www.dataphysics.com/applications/vibration-testing-and-shaker-testing/satellite-testing.html.

[3] N. Silvestre and A. Araújo. *Texto de apoio da disciplina de Mecânica estrutural*. Técnico Lisboa, 2014.

[4] J. N. Reddy. *An Introduction to the Finite Element Method*. McGraw-Hill Primis, 3^{rd} edition, 2006.

[5] E. F. Moreira. Application of topology optimization to satellite tertiary structures. Master's thesis, Mechanical Engineering, Instituto Superio Técnico, November 2016.

[6] Altair Engineering. *Practical Aspects of Finite Element Simulation: A Study Guide*. 3^{rd} edition, May 2015.

[7] MSC Software. *MSC Nastran 2017.1 Documentation*. 2017.

[8] Siemens. *NX Nastran - Theoretical manual*. 2014.

[9] Budynas-Nisbett. *Shigley's Mechanical Engineering Design*. McGraw-Hill Primis, 8^{th} edition, 2006. ISBN: 0-390-76487-6.

[10] T. Tinga. *Principles of loads and failure mechanisms; Applications in maintenance, reliability and design*. Springer, 2013. ISBN: 978-1-4471-4916-3.

[11] ECSS. ECSS-E-ST-32C Rev.1 – Structural general requirements, November 2008. URL www.ecss.nl/standard/ecss-e-st-32c-rev-1-structural-general-requirements/.

[12] NASA. FINITE ELEMENT MODEL VALIDITY CHECK 2., November 2006. URL www.femci.gsfc.nasa.gov/validitychecks/vc2.html.

[13] P. W. Christensen and A. Klarbring. *An Introduction to Structural Optimization*, volume 153. Springer, 2009. ISBN: 978-1-4020-8665-6.

[14] S. S. Rao. *Engineering Optimization: Theory and Practice*. John Wiley & Sons, Inc, 4^{th} edition, 2009. ISBN: 978-0-470-18352-6.

[15] E. Johnson, W. Wu, and X. Yu. Topology optimization with msc.nastran and msc.patran. Huntington Beach, CA, October 2004. MSC.Software VPD conference.

[16] G. Allaire, F. Jouve, and H. Maillot. Topology optimization for minimum stress design with the homogenization method. *Structural and Multidisciplinary Optimization*.

[17] M. P. Bendsøe and O. Sigmund. *Topology Optimization: Theory, Methods and Applications*. Springer, 2003. ISBN: 3-540-42992-i.

[18] Y. X. X. Huang. *Topology optimization of continuum structures: methods and applications*. Wiley, Chichester, April 2010. ISBN: 9780470689486.

[19] A. Remouchamps, M. Bruyneel, C. F. S., and G. S. Application of a bi-level scheme including topology optimization to the design of an aircraft pylon. *Struct Multidiscip Optim*, 44:739–750, 2011. doi: 10.1007/s00158-011-0682-3. URL `https://doi.org/10.1007/s00158-011-0682-3`.

[20] W. Zhang and S. Sun. Scale-related topology optimization of cellular materials and structures. *Int J Numerical Methods Eng*, 68:993–1011, November 2006.

[21] M. P. Bendsøe and N. Kikuchi. Generating optimal topologies in structural design using a homogenization method. *Computer Methods in Applied Mechanics and Engineering*, 71:197–224, November 1988. doi: 10.1016/0045-7825(88)90086-2.

[22] J.-H. Zhu, W.-H. Zhang, and L. Xia. Topology optimization in aircraft and aerospace structures design. *Archives of Computational Methods in Engineering*, 23(4):595–622, December 2016. ISSN 1886-1784. doi: 10.1007/s11831-015-9151-2. URL `https://doi.org/10.1007/s11831-015-9151-2`.

[23] M. P. Bendsøe. Optimal shape design as a material distribution problem. *Structural Optimization*, 1:193–202, December 1989. ISSN 1615-1488. doi: 10.1007/BF01650949.

[24] M. Zhou and G. I. N. Rozvany. The COC algorithm, part ii: topological, geometry and generalized shape optimization. *Computer Methods in Applied Mechanics and Engineering*, 89:197–224, 1991. doi: 10.1016/0045-7825(91)90046-9.

[25] G. I. N. Rozvany. Aims, scope, methods, history and unified terminology of computer-aided topology optimization in structural mechanics. *Structural and Multidisciplinary Optimization*, 21(2): 90–108, April 2001. ISSN 1615-1488. doi: 10.1007/s001580050174.

[26] Y. M. Xie and G. P. Steven. A simple evolutionary procedure for structural optimization. *Computers and Structures*, 49:885–896, December 1993. doi: 10.1016/0045-7949(93)90035-C.

[27] Y. M. Xie and G. P. Steven. *Basic Evolutionary structural optimization*. Springer, June 1997. ISBN 978-1-4471-0985-3. doi: 10.1007/978-1-4471-0985-3_2.

[28] O. Sigmund. A 99 line topology optimization code written in matlab. *Structural and Multidisciplinary Optimization*, 21:120–127, April 2001. ISSN 1615-1488. doi: 10.1007/s001580050176.

[29] M. Zhou and G. I. N. Rozvany. On the validity of eso type methods in topology optimization. *Structural and Multidisciplinary Optimization*, 21:80–83, March 2001. ISSN 1615-1488. doi: 10.1007/s001580050170.

[30] O. M. Querin and V. Young. Computational efficiency and validation of bi-directional evolutionary structure optimization. *Computer Methods in Applied Mechanics and Engineering*, 189:559–573, September 2000. doi: 10.1016/S0045-7825(99)00309-6.

[31] J. H. Zhu, W. Zhang, and K. P. Qiu. Bi-directional evolutionary topology optimization using element replaceable method. *Computational Mechanics*, 40:97–109, June 2006. ISSN 1432-0924. doi: 10.1007/s00466-006-0087-0.

[32] X. Huang and Y. M. Xie. A further review of eso type methods for topology optimization. *Structural and Multidisciplinary Optimization*, 41(5):671–683, May 2010. ISSN 1615-1488. doi: 10.1007/s00158-010-0487-9.

[33] X. Huang, S. W. Zhou, Y. M. Xie, and Q. Li. Topology optimization of microstructures of cellular materials and composites for macrostructures. *Comput Mater Sci*, 67:397–407, February 2013.

[34] L. Xia and P. Breitkopf. Concurrent topology optimization design of material and structure within fe2 nonlinear multiscale analysis framework. *Comput Methods Appl Mech Eng*, 278:524–542, August 2014.

[35] L. Yin and G. K. Ananthasuresh. Topology optimization of compliant mechanisms with multiple materials using a peak function material interpolation scheme. *Structural and Multidisciplinary Optimization*, 23(1):49–62, December 2001. ISSN 1615-1488. doi: 10.1007/s00158-001-0165-z.

[36] L. Xia and P. Breitkopf. A reduced multiscale model for nonlinear structural topology. *Comput Methods Appl Mech Eng*, 280:117–134, October 2014.

[37] X. Yan, X. Huang, Y. Zha, and Y. M. Xie. Concurrent topology optimization of structures and their composite microstructures. *Comput Struct*, 133:103–110, March 2014.

[38] O. Sigmund. Morphology-based black and white filters for topology optimization. *Structural and Multidisciplinary Optimization*.

[39] C. S. Jog and R. B. Haber. Stability of finite element models for distributed-parameter optimization and topology design. *Computer Methods in Applied Mechanics and Engineering*, 130:203–226, April 1996.

[40] O. Sigmund and J. Petersson. Numerical instabilities in topology optimization: a survey on procedures dealing with checkerboards, mesh-dependencies and local minima. *Structural optimization*, 16(01):68–75, August 1998. ISSN 1615-1488. doi: 10.1007/BF01214002.

[41] T. E. Bruns and D. A. Tortorelli. Topology optimization of nonlinear elastic structures and compliant mechanisms. *Computer Methods in Applied Mechanics and Engineering*, 190:3443–3459, March 2001.

[42] G.-W. Jang, J. H. Jeong, Y. Y. Kim, D. Sheen, C. Park, and M.-N. Kim. Checkerboard-free topology optimization using nonconforming finite elements. *International Journal for Numerical Methods in Engineering*, 57:1717–1735, June 2003.

[43] R. B. Haber, C. S. Jog, and M. P. Bendsøe. A new approach to variable-topology shape design using a constraint on perimeter. *Structural optimization*, 11(1):1–12, February 1996. ISSN 1615-1488. doi: 10.1007/BF01279647.

[44] W. H. Zhang and P. Duysinx. Dual approach using a variant perimeter constraint and efficient sub-iteration scheme for topology optimization. *Computers and Structures*, 81:2173–2181, September 2003.

[45] Q. Li, G. P. Steven, and Y. M. Xie. A simple checkerboard suppression algorithm for evolutionary structural optimization. *Structural and Multidisciplinary Optimization*, 22:230–239, Oct 2001. ISSN 1615-1488. doi: 10.1007/s001580100140.

[46] X. Y. Yang and Y. M. Xie. Perimeter control in the bi-direction evolutionary optimization method. *Structural and Multidisciplinary Optimization*, 24:430–440, 2003.

[47] H. A. Eschenauer, H. A. Kobelev, and A. Schumacher. Bubble method for topology and shape optimization of structures. *Structural optimization*, 8:42–51, Aug 1994. ISSN 1615-1488. doi: 10.1007/BF01742933.

[48] J. Sokołowski and A. Zochowski. On the topological derivative in shape optimization. *SIAM J Control Optim*, 37:1251–1272, 1999.

[49] G. Allaire, F. Jouve, and A. M. Toader. Structural optimization using sensitivity analysis and a level-set method. *Journal of Computational Physics*, 194:363–393, February 2004.

[50] J. A. Sethian and A. Wiegmann. Structural boundary design via level set and immersed interface methods. *Journal of Computational Physics*, 163:489–528, September 2000.

[51] M. Y. Wang, S. K. Chen, and X. M. W. Y. L. Mel. Design of multimaterial compliant mechanisms using level-set methods. *Journal of Mechanical Design*, 127:941–956, September 2005. doi: 10.1115/1.1909206.

[52] B. Bourdin and A. Chambolle. Design-dependent loads in topology optimization. *ESAIM: Control Optim Calc Var*, 9:19–48, 2003.

[53] N. V. Dijk, K. Maute, M. Langelaar, and F. V. Keulen. Level set methods for structural topology optimization: a review. *Structural and Multidisciplinary Optimization*, 48(3):437–472, September 2013. ISSN 1615-1488. doi: 10.1007/s00158-013-0912-y.

[54] G. I. N. Rozvany. A critical review of established methods of structural topology optimization. *Structural and Multidisciplinary Optimization*, 37:217–237, January 2009. ISSN 1615-1488. doi: 10.1007/s00158-007-0217-0.

[55] I. Gibson, D. Rosen, and B. Stucker. *Additive Manufacturing Technologies*. Springer, 2^{nd} edition, 2015. ISBN: 978-1-4939-2112-6.

[56] ASTM International. Committee F42 on Additive Manufacturing Technologies, March 2018. URL www.astm.org/COMMITTEE/F42.htm.

[57] ASTM F2792-10, Standard Terminology for Additive Manufacturing Technologies. ASTM International, West Conshohocken, PA USA, 2010. DOI: 10.1520/F2792-10. URL www.astm.org/cgi-bin/resolver.cgi?F2792.

[58] T. Vaneker. 3D printing course, September 2017. 3D printing classes in University of Twente, Netherlands, Course code: 201400103.

[59] E. Herderick. *Additive Manufacturing of Metals: A Review*. Materials Science and Technology (MS &T), EWI, Columbus, OH USA, October 2011.

[60] ASTM International. *The Global Leader in Additive Manufacturing Standards*. West Conshohocken, PA USA, August 2017.

[61] Loughborough University. About Additive Manufacturing, March 2018. URL www.lboro.ac.uk/research/amrg/about/.

[62] K. V. Wong and A. Hernandez. *A Review of Additive Manufacturing*, volume 2012, pages 1–10. ISRN Mechanical Engineering, May 2012.

[63] ASTM International. Committee F42 on Additive Manufacturing Technologies, March 2018. URL www.astm.org/COMMIT/SUBCOMMIT/F42.htm.

[64] U.S. Department of Transportation. Federal Aviation Administration. *Additive Manufacturing in Maintenance, Preventive Maintenance, and Alteration of Aircraft, Aircraft Engines, Propellers, and Appliances*, 2016.

[65] J. Coykendall, M. Cotteleer, J. Holdowsky, and M. Mahto. 3D opportunity in aerospace and defense; Additive manufacturing takes flight. Technical report, Deloitte University Press, 2014.

[66] ISO. ISO/TC 261 - Additive manufacturing, March 2018. URL www.iso.org/committee/629086/x/catalogue/p/0/u/1/w/0/d/0.

[67] ISO. 25.030 - Additive manufacturing, March 2018. URL www.iso.org/ics/25.030/x/p/1/u/1/w/0/d/0.

[68] ASTM International. Additive Manufacturing Technology Standards, March 2018. URL www.astm.org/Standards/additive-manufacturing-technology-standards.html.

[69] T. Kellner. An Epiphany Of Disruption: GE Additive Chief Explains How 3D Printing Will Upend Manufacturing. Technical report, GE Reports, 2017.

[70] M. Tomlin and J. Meyer. *Topology Optimization of an Additive Layer Manufactured (ALM) Aerospace Part*. EADS Innovation Works, 2011.

[71] *Topology Optimisation of an Aerospace Part to be Produced by Additive Layer Manufacturing (ALM)*. Altair Engineering, 1820 E. Big Beaver Rd., Troy, MI 48083-2031 USA, 2011.

[72] O. Sigmund. On the usefulness of non-gradient approaches in topology optimization. *Struct Multidiscip Optim*, 43:589–596, 2011.

[73] D. Brackett, I. Ashcroft, and R. Hague. *Topology Optimization for Additive Manufacturing*. Wolfson School of Mechanical and Manufacturing Engineering, Loughborough University, August 2011.

[74] E. de Sturler, G. H. Paulion, and S. Wang. Topology optimization with adaptive mesh refinement. Ithaca, NY, USA, 2008. 6th International Conference on Computation of Shell and Spatial Structures IASSIACM, Cornell University.

[75] K. A. James, J. S. Hansen, and J. R. Martins. Structural topology optimization for multiple load cases using a dynamic aggregation technique. *Engineering Optimization*, 41(12):1103–1118, 2009. doi: 10.1080/03052150902926827. URL https://doi.org/10.1080/03052150902926827.

[76] Z. Liu and J. G. Korvink. Adaptive moving mesh level set method for structure topology optimization. *Engineering Optimization*, 40(6):529–558, 2008. doi: 10.1080/03052150801985544. URL https://doi.org/10.1080/03052150801985544.

[77] K. Maute and E. Ramm. Adaptive topology optimization. *Structural Optimization*, 10:100–112, 1995. doi: 10.1007/BF01743537ID. URL https://doi.org/10.1007/BF01743537D0.

[78] T. H. Nguyen, G. H. Paulino, J. Song, and C. H. Le. A computational paradigm for multiresolution topology optimization (mtop). *Structural and Multidisciplinary Optimization*, 41:525–539, Apr 2010. ISSN 1615-1488. doi: 10.1007/s00158-009-0443-8. URL https://doi.org/10.1007/s00158-009-0443-8.

[79] M. Verani, M. B. C. Cinquini, and P. Venini. Topology optimization and mesh adaptivity. Siracusa, 2010. XVIII GIMC Conference.

[80] S. Wang and E. de Sturler G. H. Paulino. Dynamic adaptive mesh refinement for topology optimization. *International Journal of Numerical Methods*, 69:2441–2468, 2008.

[81] S. Wang and Krylov. *Subspace methods for topology optimization on adaptive meshes*. PhD thesis, University of Illinois at Urbana-Champaign, 2007.

[82] R. Stainko. An adaptive multilevel approach to the minimal compliance problem in topology optimization. *Communications in Numerical Methods in Engineering*, 22:109–118, 2006.

[83] T. A. Poulsen. A new scheme for imposing minimum length scale in topology optimization. *International Journal for Numerical Methods in Engineering*, 57:741–760, 2003.

[84] J. K. Guest, J. H. Prevost, and T. Belytschko. Achieving minimum length scale in topology optimization using nodal design variables and projection functions. *International Journal for Numerical Methods in Engineering*, 61:238–254, 2004.

[85] Altair Engineering. Altair OptiStruct Overview, March 2018. URL `www.altairhyperworks.com/product/OptiStruct`.

[86] MSC Software. MSC Nastran - Multidisciplinary Structural Analysis, March 2018. URL `www.mscsoftware.com/product/msc-nastran`.

[87] O. Sigmund. *Design of Material Structures using Topology Optimization*. Department of Solid Mechanics, Technical University of Denmark, Lyngby, Denmark, 1994.

[88] E. Andreassen, A. Clausen, M. Schevenels, B. S. Lazarov, and O. Sigmund. Efficient topology optimization in matlab using 88 lines of code. *Structural and Multidisciplinary Optimization*, 43: 1–16, January 2011. ISSN 1615-1488. doi: 10.1007/s00158-010-0594-7.

[89] K. Liu and A. Tovar. An efficient 3d topology optimization code written in matlab. *Structural and Multidisciplinary Optimization*, 50:1175–1196, December 2014. ISSN 1615-1488. doi: 10.1007/s00158-014-1107-x.

[90] P. R. A. Fernandes. *Optimização da topologia de estruturas tridimensionais*. UTL, Instituto Superior Técnico, Lisbon, 1998.

[91] M. P. Bendsøe. *Optimization of structural topology, shape, and material*. Springer, January 1995. doi: 10.1007/978-3-662-03115-5. ISBN: 978-3-662-03115-5.

[92] Altair Engineering. *Practical Aspects of Structural Optimization: A Study Guide*. 2^{nd} edition, June 2015.

[93] 3D SYSTEMS. VisiJet M3 Crystal (MJP), April 2018. URL `www.3dsystems.com/materials/visijet-m3-crystal`.

[94] 3D SYSTEMS. ProJet MJP 3600 Series, April 2018. URL `www.3dsystems.com/3d-printers/projet-mjp-3600-series`.

[95] 3D SYSTEMS. About, April 2018. URL `www.3dsystems.com/about-us`.

[96] Brüel and Kjaer. Accelerometers and charge amplifiers, 2017. URL `www.bksv.com/en`.

[97] Arcam EBM. EBM-Built Materials, February 2018. URL `www.arcam.com/technology/electron-beam-melting/materials/`.

[98] EOS. Materials for Metal Additive Manufacturing, February 2018. URL `www.eos.info/material-m`.

[99] CONCEPTLASER. Materials, February 2018. URL www.concept-laser.de/en/products/materials.html.

[100] SLM SOLUTIONS. 3D Metals, February 2018. URL www.slm-solutions.com/file/201en171023-01-001-powderwebpdf.

[101] 3D SYSTEMS. Metal Materials, March 2018. URL www.3dsystems.com/materials/metal.

[102] E. Brusa, R. Sesana, and E. Ossola. Numerical modeling and testing of mechanical behavior of am titanium alloy bracket for aerospace applications. Funchal, Madeira, Portugal, September 2017. 2^{nd} international conference on structural integrity, ICSI 2017.

[103] D. Waltona and H. Moztarzadeh. *Design and development of an additive manufactured component by topology optimisation*. University of Warwick, United Kingdom, 2017.

[104] Würth. 1/4-INCH TORQUE WRENCH, July . URL www.eshop.wuerth.de/1-4-inch-torque-wrench-TRQWRNCH-RTCH-1-4IN-4-20NM-/071471%2020.sku/en/US/EUR/?VisibleSearchTerm=1%2F4+torque+wrenc&CampaignName=SR001.

[105] Würth. 1/4-INCH TORQUE WRENCH, July . URL www.eshop.wuerth.de/Product-categories/1-4-inch-socket-wrench-metric-hex-short/14016019060110.cyid/1401.cgid/en/US/EUR/?CatalogCategoryRef=14016019060110%40WuerthGroup-Wuerth-1401&CampaignName=SR001&SelectedFilterAttribut=%255B%255D.

[106] N. E. Uzan, R. Shneck, O. Yeheskel, and N. Frage. Fatigue of alsi10mg specimens fabricated by additive manufacturing selective laser melting (am-slm). *Materials Science and Engineering: A*, 704:229–237, September 2017. URL https://doi.org/10.1016/j.msea.2017.08.027.

[107] N. S. Sripada. A methodology for topology and lattice structure optimization of a cargo drone motor mount. Master's thesis, Mechanical Engineering, The University of Texas at Arlington, December 2017.

[108] S. Park, D. W. Rosen, and C. E. Duty. Comparing mechanical and geometrical properties of lattice structure fabricated using electron beam melting. *Solid. Free Fabr. Symp*, pages 1359–1370, 2014.

[109] J. Nguyen, S. Park, D. W. Rosen, L. Folgar, and J. Williams. Conformal lattice structure design and fabrication. *Sff*, pages 138–161, 2012.

[110] M. McMillan, M. Jurg, M. Leary, and M. Brandt. Programmatic lattice generation for additive manufacture. *Procedia Technol*, 20:178–184,, July 2012.

[111] P. S. Chang and D. W. Rosen. The size matching and scaling method: A synthesis method for the design of mesoscale cellular structures. *Int. J. Comput. Integr. Manuf*, 2013.

[112] J. Chu, S. Engelbrecht, G. Graf, and D. W. Rosen. A comparison of synthesis methods for cellular structures with application to additive manufacturing. *Rapid Prototyp*, 16:275–283,, 2010.

[113] X. Guo. Additive manufacture oriented topology optimization based on approaches with explicit geometry description. In *IUTAM SYMPOSIUM: When topology optimization meets additive manufacturing - theory and methods*, Dalian, China, October 2018. Dalian University of Technology, State Key Laboratory of Structural Analysis for Industrial Equipment and International Research Center for Computational Mechanics.

[114] L. Gao, J. Fu, H. Li, and M. Xiao. Multiscale topology optimization of shell-infill structures using a distance regularized parametric level-set method. In *IUTAM SYMPOSIUM: When topology optimization meets additive manufacturing - theory and methods*, Dalian, China, October 2018. Dalian University of Technology, State Key Laboratory of Structural Analysis for Industrial Equipment and International Research Center for Computational Mechanics.

[115] J. Yan, T. Yu, C. Zhang, J. Guo, and Q. Zhou. Parallel multi-scale topology optimization of lattice materials in point view of additive manufacturing. In *IUTAM SYMPOSIUM: When topology optimization meets additive manufacturing - theory and methods*, Dalian, China, October 2018. Dalian University of Technology, State Key Laboratory of Structural Analysis for Industrial Equipment and International Research Center for Computational Mechanics.

[116] S.-Y. Duan, W.-B. Wen, and D.-N. Fang. Mechanical performance of additively-manufactured three-dimensional lattice meta-materials designed via topological optimization. In *IUTAM SYMPOSIUM: When topology optimization meets additive manufacturing - theory and methods*, Dalian, China, October 2018. Dalian University of Technology, State Key Laboratory of Structural Analysis for Industrial Equipment and International Research Center for Computational Mechanics.

[117] X. Zhang, H. Zhou, and H. Zeng. Additive manufacturing spacecraft structure: Design and evaluation. In *IUTAM SYMPOSIUM: When topology optimization meets additive manufacturing - theory and methods*, Dalian, China, October 2018. Dalian University of Technology, State Key Laboratory of Structural Analysis for Industrial Equipment and International Research Center for Computational Mechanics.

[118] W. Chen, X. Zheng, and S. Liu. Finite-element-mesh based method for modeling and optimization of lattice structures for additive manufacturing. In *IUTAM SYMPOSIUM: When topology optimization meets additive manufacturing - theory and methods*, Dalian, China, October 2018. Dalian University of Technology, State Key Laboratory of Structural Analysis for Industrial Equipment and International Research Center for Computational Mechanics.

[119] ISO. ISO 527-1: Plastics – Determination of tensile properties – Part 1: General principles, February 2012. URL `www.iso.org/standard/56045.html`.

[120] ASTM International. D638-14: Standard test method for tensile properties of plastics, 2014. URL `www.astm.org/Standards/D638.htm`.

Appendix A

L-shape technical draw

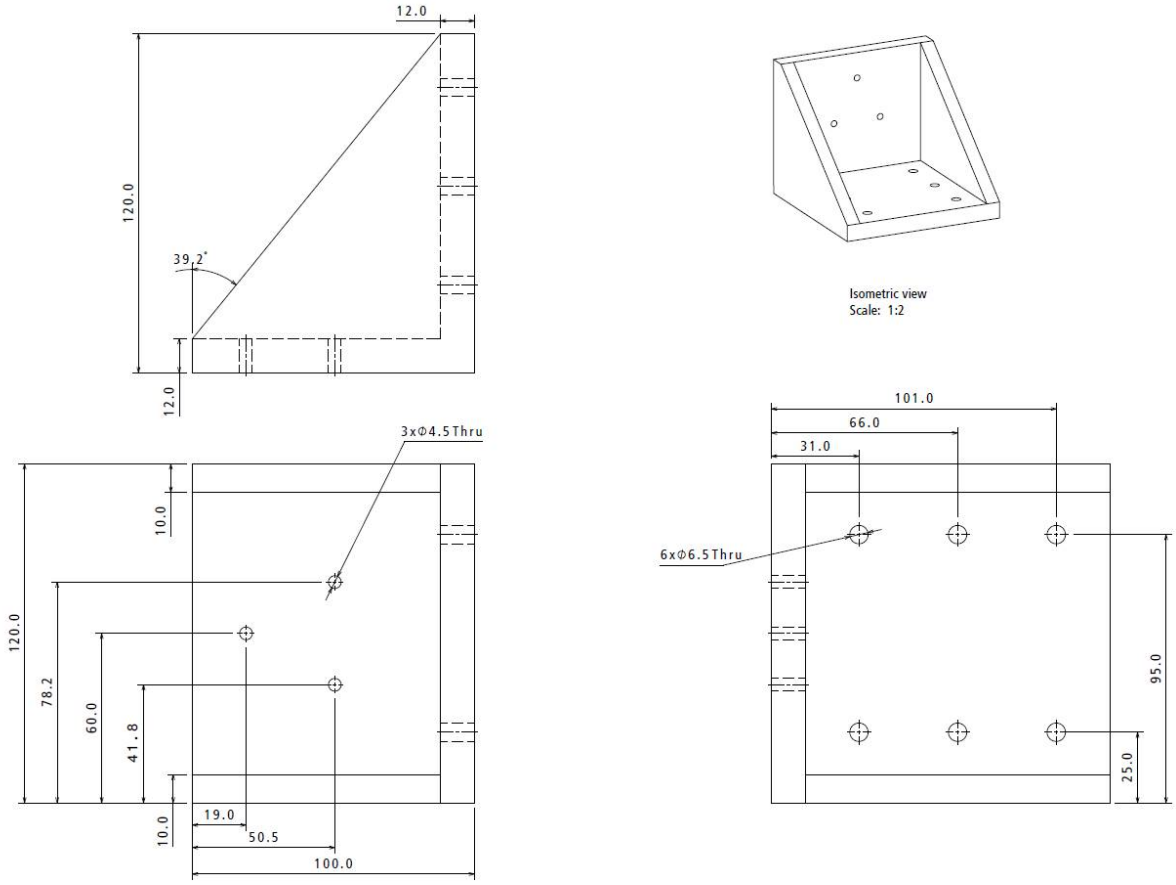

Figure A.1: L-shape technical draw.

Appendix B

Benchmark examples

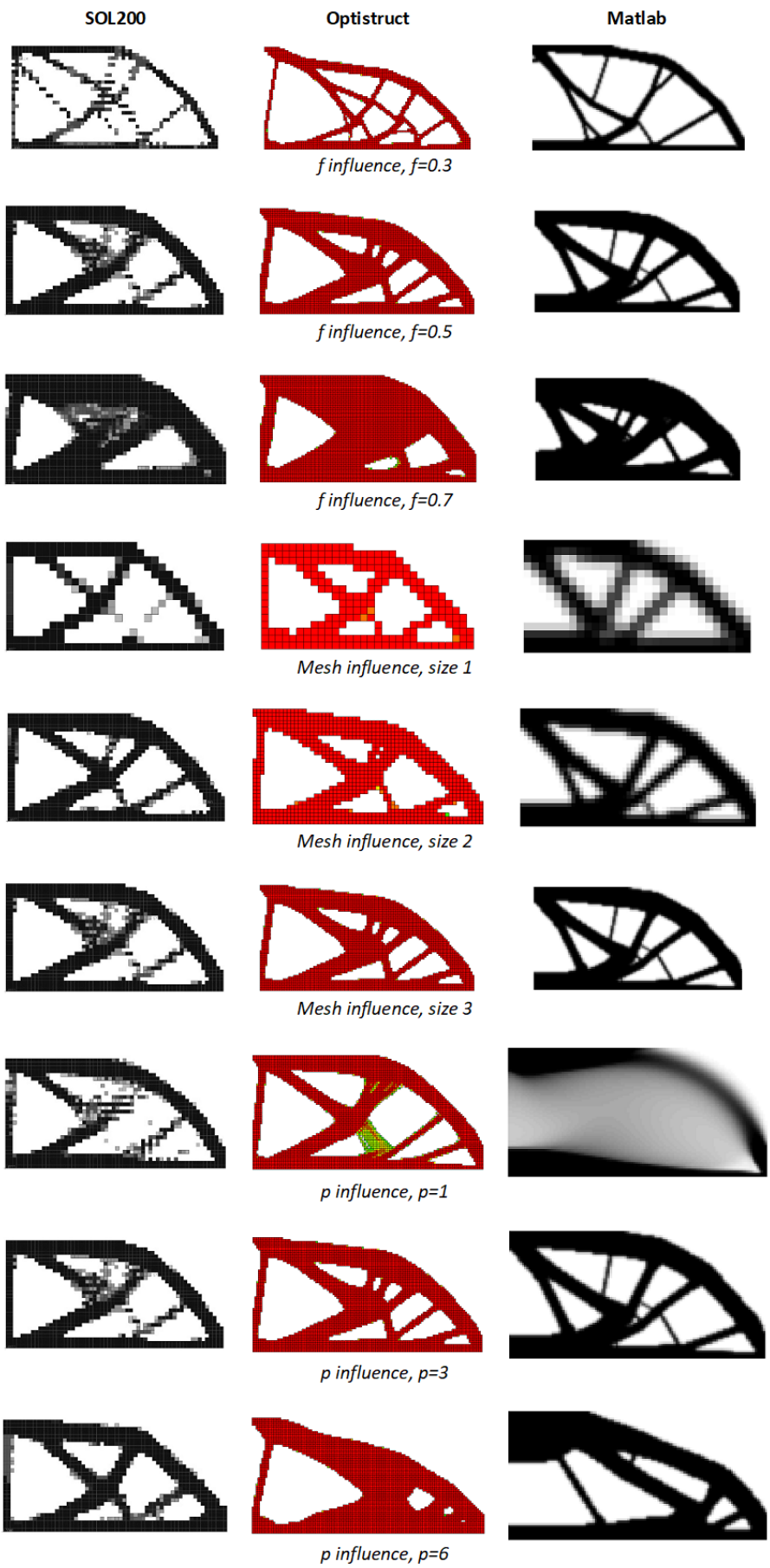

Figure B.1: 2D obtained geometries.

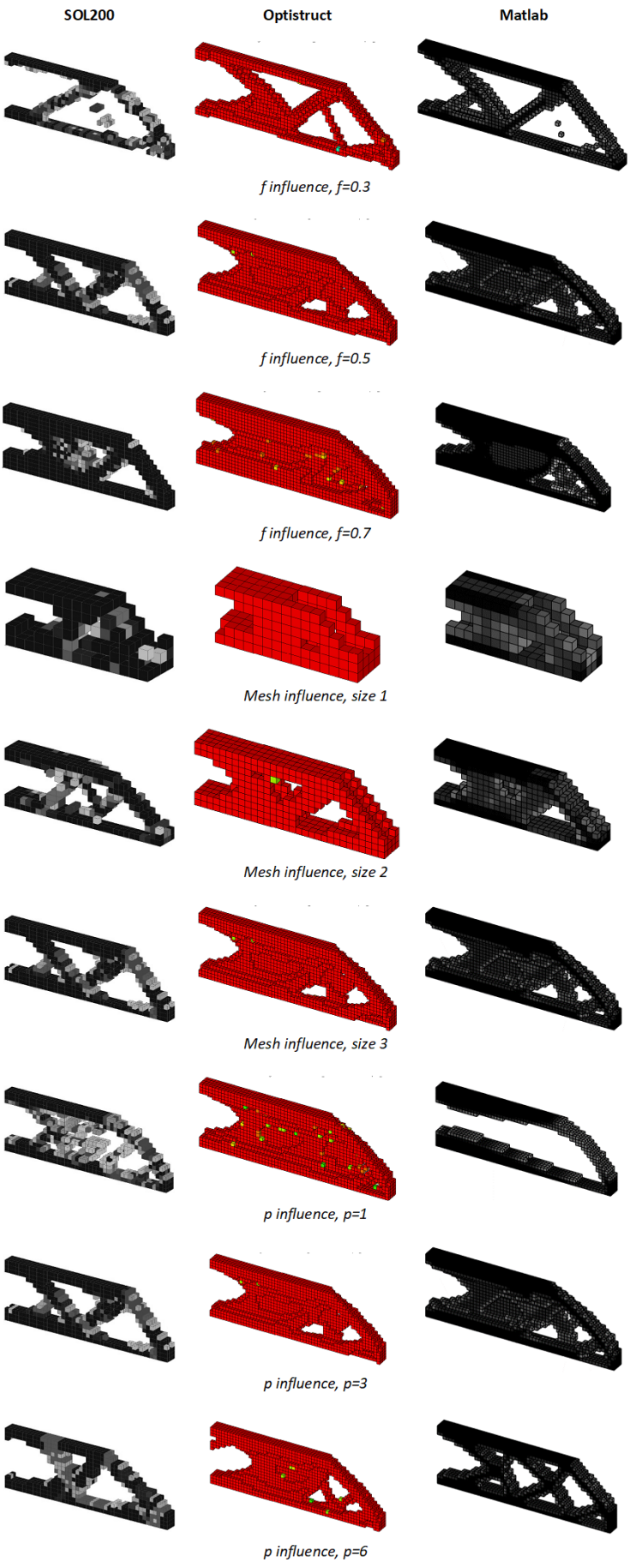

Figure B.2: 3D obtained geometries.

Appendix C

VisiJet M3 Crystal characterization

C.1 Objectives

The experimental activity aims to characterize *VisiJet M3 Crystal* properties. Some properties like Young's modulus, tensile strength and strain at break will be verified and compared with the material's datasheet values while others, like yield strength and Poisson's ratio, will be evaluated without any base value in the datasheet. It will also be verified if the material is isotropic or not. The material's fatigue behaviour will not be evaluated since it would be time consuming and would not help in this thesis work due to the small present stresses observed in section 2.3. The purpose of this experiment is to use accurate properties during the numerical work.

C.2 Description

C.2.1 Measurements

The test specimen is extended along its major longitudinal axis at a constant speed of 1.4 mm/min until it fractures. During this procedure, the load sustained by the specimen and the respective strain are measured. The strain measurement is done through a mechanical and a video extensometer. Both complies with ISO 9513 which is a standard for static calibration of extensometers systems for uniaxial tests. The video extensometer is an Instron AVE – Advanced Video Extensometer with 4 points of measurement in the same plane (2 in each direction) which enable the measure of the strain in two directions and consequently the Poisson's ratio calculation. The mechanical extensometer (Instron 2630-100 Series Clip-On) has been used for long in Instituto Superior Técnico experimental assignments and is a trustworthy sensor. So, in order to verify the video-extensometer results, both of them were used in all tests to compare their acquired longitudinal data.

C.2.2 Specimens

In order to assess the isotropy of the material, the specimens will be produced with several orientations along the machine layer/platform plan and along the perpendicular one. The machine layer/platform plan will be called "xy" direction plan from now on while the perpendicular one will be called "z" direction plan. In the xy plan, the layer/platform length is x and its width is y.

Using 3 specimen for each orientation and assuming the angles between the x and y axis, table C.1 and figure C.1 shows the combination of specimens.

Table C.1: Specimen plan

	Printing axis direction	
Orientation [Deg]	***xy***	**z**
0	3	3
45	3	3
90	3	3

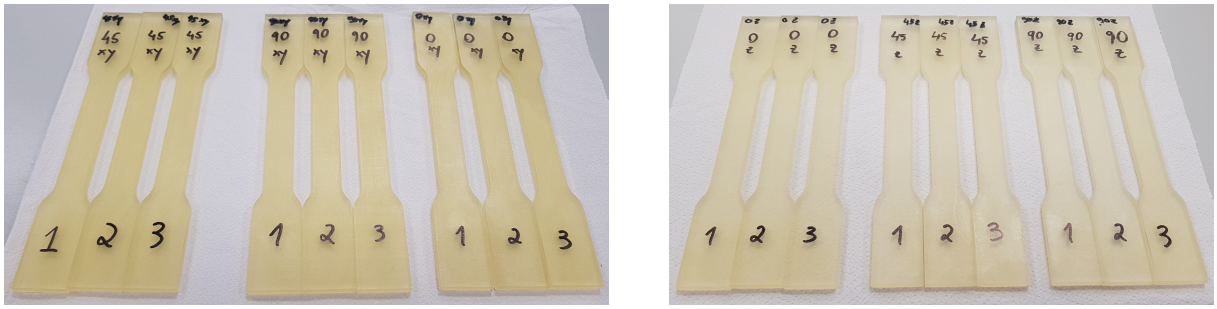

(a) xy. (b) z.

Figure C.1: Specimens.

C.2.3 Procedure and Set-up

Although it is not for 3D printed materials, ISO 527-1 [119] was used as a guideline since it is a standard for the determination of tensile properties in plastics and is a variant of the standard used by *3D Systems* for the properties in the material's datasheet – ASTM D638 [120].

The specimen's material is the *VisiJet M3 Crystal* and its dimensions were chosen to use most of the grip area to avoid any relative slip between the gripping jaws and the specimen without using too much force to avoid any premature fracture in the gripping area. The geometry can be seen in figure C.2.

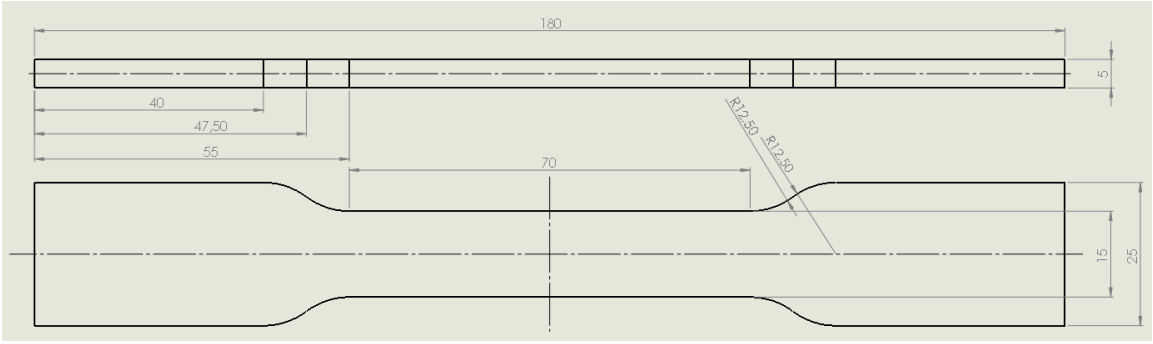

Figure C.2: Specimen's geometry.

The specimens were produced in the "XHD" mode of *3D systems' ProJet MJP 3600* machine (figure C.3a) using *Visijet S300* as support material (figure C.3b). After the printing, the specimens were for 2 minutes inside the fridge to facilitate their removal from the printing platform. Furthermore, they were collocated in the oven (figure C.4a) at 65 ºC for 25 minutes to melt the support material. The oven used is the *3D systems Projet Finisher 1-B model* (figure C.4b).

(a) *ProJet MJP 3600* machine.

(b) Specimens after printing with support material.

Figure C.3: ProJet MJP 3600 machine and produced specimens.

(a) Specimens inside the oven.

(b) *3D systems Projet Finisher 1-B oven.*

Figure C.4: Support material melting.

The last step for the specimens' preparation was the marks for the video extensometer. Following Instron's AVE model K manual, the specimen was marked with white dots as shown in figure C.5a. The marks are very important to achieve good accuracy in the results, therefore, a JIG was developed to perform the marks in the right spots. The longitudinal distance between dots' centers was supposed to be 66mm while the horizontal one was supposed to be 11mm. It is possible to see in figure C.5b that this was almost achieved.

To control the experiment, software Bluehill was used in an Instron 5566J model with a load cell of 10 KN that was calibrated together with both extensometers: Instron AVE model K and Instron 2630-100 Series Clip-On. Theoretically, the maximum necessary load to achieve fracture can be calculated through equation C.1.

$$\sigma_{uts} = \frac{F}{A} \Leftrightarrow 40.2 = \frac{F}{15 \cdot 5} \Leftrightarrow F \approx 3\ KN \tag{C.1}$$

With σ_{uts} as the material tensile strength, F as the uniaxial load and A as the cross-sectional area. So, in order to improve the accuracy of the experimental test, the used load cell needs to be able to fracture the specimen but at the same time, its load capacity must be as close as possible of the maximum necessary load. The load cell of 10 KN was chosen since it was the one available that could fulfill these two requirements. Two pictures from the experimental setup are shown in figure C.6.

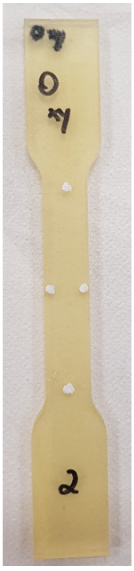

(a) Specimen's white dots .

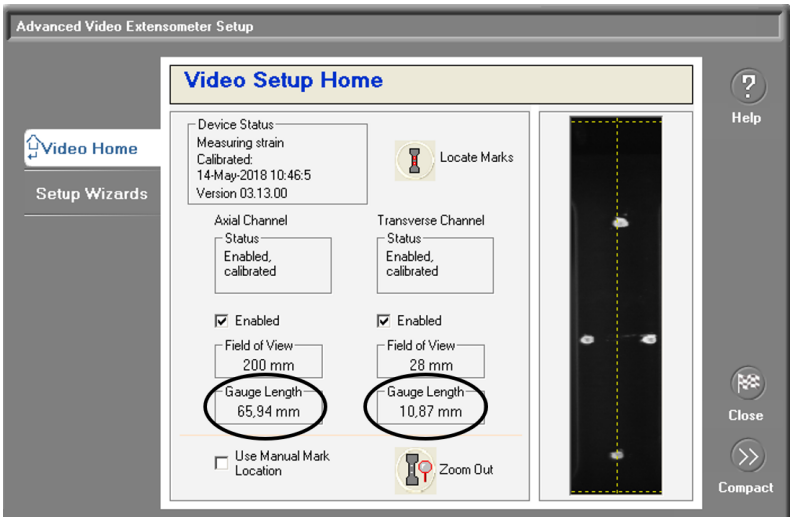

(b) AVE dots reading .

Figure C.5: Measurement marks setup.

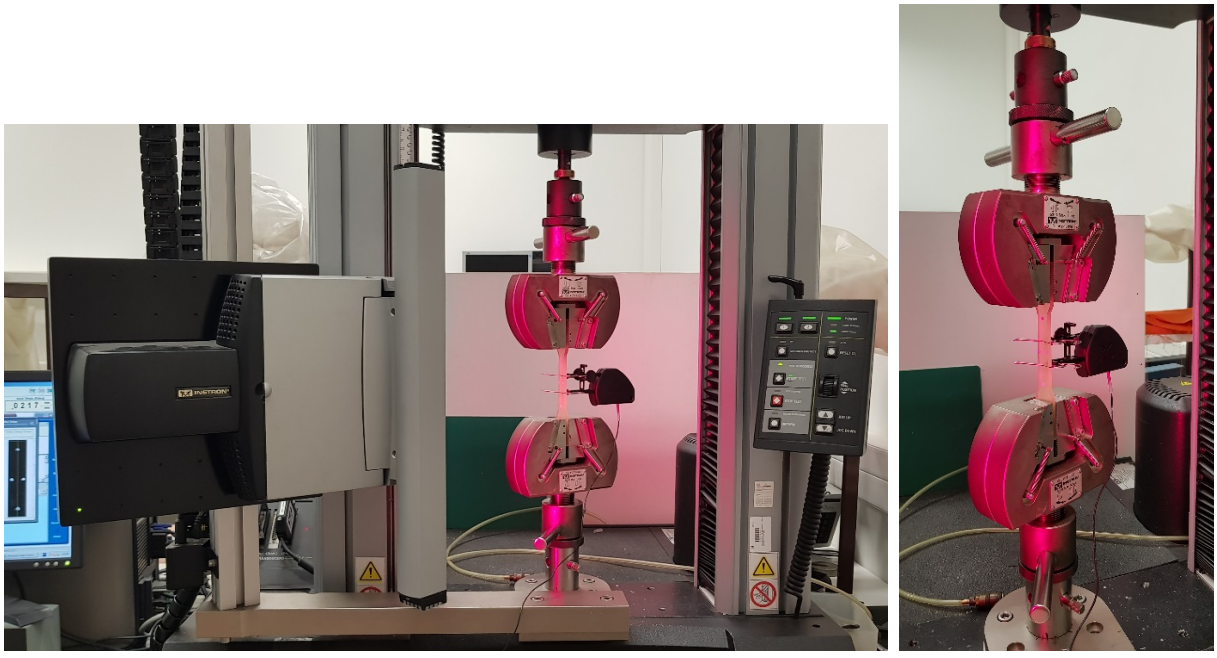

(a) (b)

Figure C.6: Experimental setup.

C.2.4 Results

As explained before, the experiment was done until the fracture of the specimen as shown in figure C.7.

Figure C.7: Fractured specimen.

From figure C.8, it is possible to see that the specimens had a similar behavior for the several orientations within the same building direction (xy or z). From the same figure, it is also possible to conclude that during the elastic region the specimens present a similar behavior, although the specimens built along z direction are stiffer than the ones built along xy direction. Besides, even though these ones are stiffer, it is important to note that they are also considerably less ductile.

From figure C.9 to C.11, it is shown that the three specimens produced in the same way have similar response which give confidence about these results due to their consistency.

Several graphics were produced from the different specimens but just these ones are presented to illustrate the results. All the other specimens presented similar results.

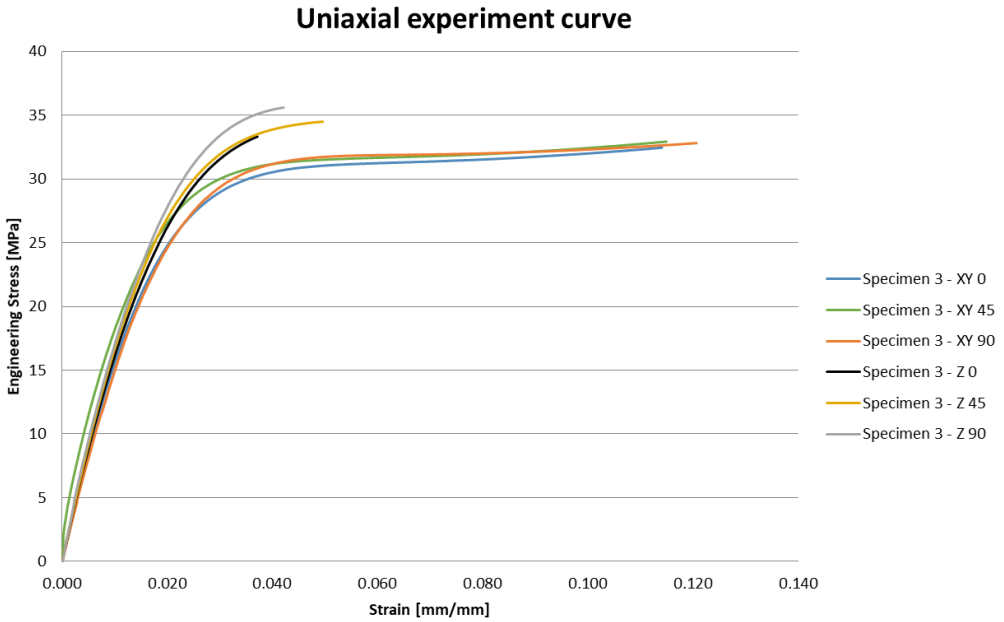

Figure C.8: Data acquired from 6 specimens with different building directions and orientations.

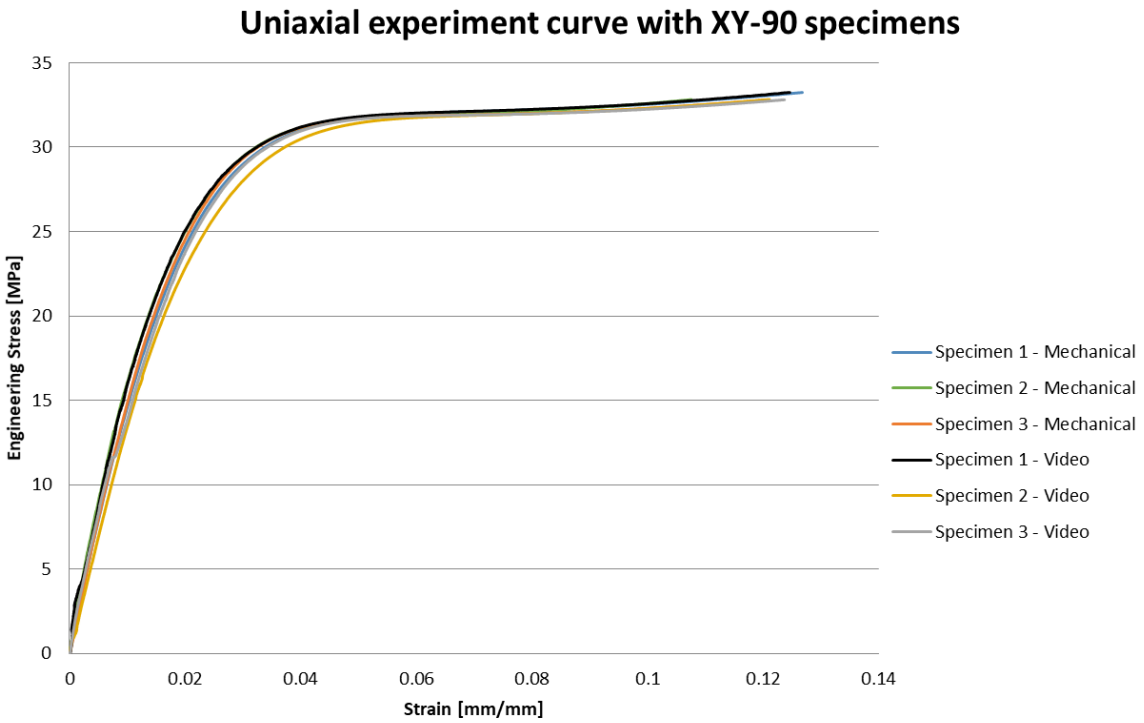

Figure C.9: Data acquired from the 3 specimens xy with 90 degrees orientation.

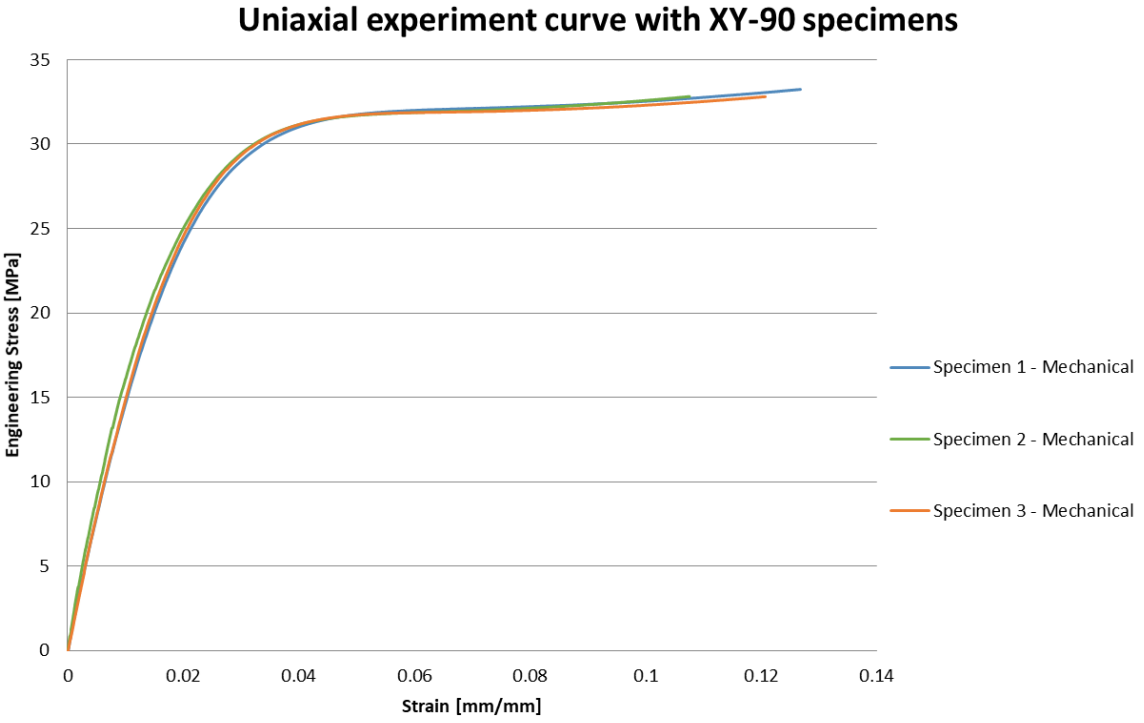

Figure C.10: Data acquired by mechanical extensometer from the 3 specimens XY with 90 degrees orientation.

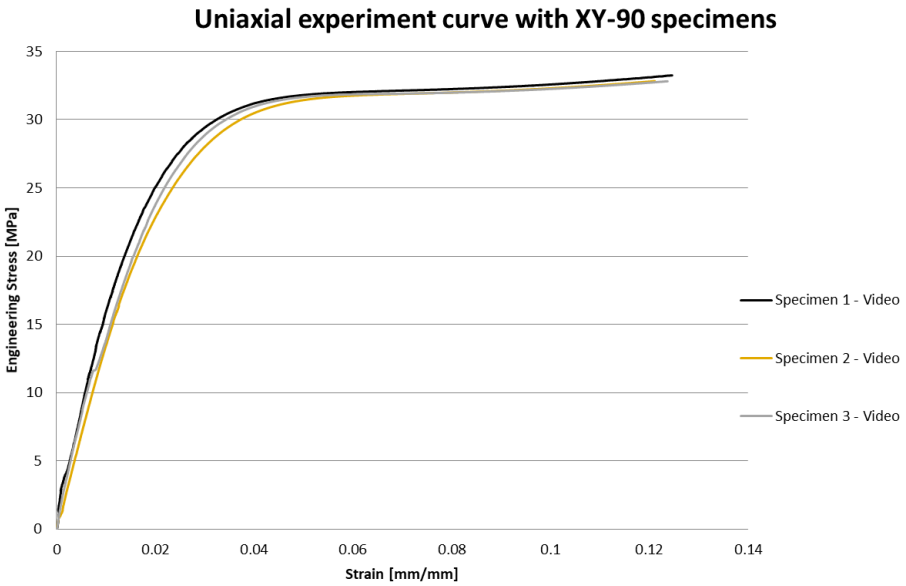

Figure C.11: Data acquired by video-extensometer from the 3 specimens XY with 90 degrees orientation.

The average values of several properties were calculated for each building direction and orientation as shown in table C.2. The average "Young's modulus" and average "strain at break" values will be used to assess the relative difference between the mechanical and video extensometer where the reference value used is the mechanical one since it is the sensor were the author have more confidence as explained before. The calculated values can be seen in table C.3.

Table C.2: Experimental average values.

	Experimental average					
	xy			**z**		
	0	*45*	*90*	*0*	*45*	*90*
ν	0.34	0.34	0.54	0.42	0.38	0.4
σ_{uts} *[MPa]*	32.47	32.77	32.96	33.46	32.02	34.98
σ_y *[MPa]*	19.64	20.11	19.35	20.67	21.07	22.91
Mechanical E *[MPa]*	1393.27	1420.17	1377.87	1467.43	1504.80	1492.47
Video E *[MPa]*	1243.47	1318.03	1280.23	1462.60	1437.97	1452.13
Mechanical strain at break	12.76%	12.18%	13.11%	3.81%	3.84%	4.10%
Video strain at break	13.86%	12.81%	13.66%	3.81%	3.93%	3.92%

Table C.3: Relative difference between the mechanical and vídeo-extensometer.

	Relative difference between mechanical (reference) and video extensometer					
	xy			**z**		
	0	*45*	*90*	*0*	*45*	*90*
E	10.75%	7.19%	7.09%	0.33%	4.44%	2.7%
Strain at break	8.63%	5.19%	4.19%	0.08%	2.34%	4.53%

There are slight differences (typically below 10%) between the data acquired by the mechanical and video extensometer which enables the calculation of the Poisson's ratio through the video one. From now on, only the **Young's modulus** and **strain at break** values measured by the **vídeo extensometer** will be used.

Using the average values calculated before, table C.4 was developed to assess the relative difference between the different orientation values within each building direction plan. The reference orientation is the one presented in the left side. For example, in the “0-45” column, the “0” values are used as reference.

Table C.4: Relative difference between different orientation specimens.

	Relative differences between orientation specimens (Left orientation asreference)					
	xy			**z**		
	0-45	*45-90*	*0-90*	*0-45*	*45-90*	*0-90*
ν	1.08%	58.26%	56.57%	9.28%	3.17%	6.73%
σ_{uts}	0.93%	1.52%	0.58%	4.31%	4.55%	9.26
σ_y	2.36%	1.51%	3.78%	1.94%	10.85%	8.74%
E	6.00%	2.96%	2.87%	1.68%	0.72%	0.99%
Strain at break	7.58%	1.43%	6.65%	3.25%	2.75%	0.48%

During the experiment, a problem occurred with the horizontal dots on 2 of the $xy - 90$ specimens which gave a senseless result in the average Poisson’s value. In table C.2, the average value is 0.54 due to the 3 different specimen values: 1.03, 0.06 and 0.51. This is the reason for the unmeaningful values for the xy “0-90” and “45-90” relative difference in the Poisson’s ratio row. Besides these 2 values, the others typically are below 10% which indicates only slightly differences between them. This enables the calculation of an average value for the xy and z specimens and a comparison between these ones and the properties available in the material’s datasheet [93]. This comparison is shown in table C.5 using the left value as reference as done before.

Table C.5: Relative and absolute difference between experimental and datasheet values.

	Experimental average		**Datasheet**	**Relative difference (Left as reference)**			**Absolute difference**		
	xy	**z**		**z-xy**	**Data-xy**	**Data-z**	**z-xy**	**Data-xy**	**Data-z**
ν	0.34	0.4	-	14.61%	-	-	0.06	-	-
σ_{uts} *[MPa]*	32.73	33.49	42.40	2.26%	22.80%	21.02%	0.76	9.67	8.91
σ_y *[MPa]*	19.70	21.55	-	8.58%	-	-	1.85	-	-
E *[MPa]*	1397.10	1488.23	1463.00	6.12%	4.50%	1.72%	91.13	65.90	25.23
Strain at break	12.68%	3.92%	6.83%	223.73%	85.67%	42.65%	0.09	0.06	0.03

There are some significant differences in the results obtained and the ones presented by the datasheet for the tensile strength and strain at break. The experimental results show higher strain values but lower tensile strength values which does not make sense. However, the variables of interest for this thesis work will be the Poisson’s ratio, yield strength and Young’s modulus. So, based on table C.5 and in the conclusions from figure C.8, the material can be assumed as isotropic in the elastic region and an average value (using only the experimental values) can be used for the three properties. This is possible since there are small differences between the properties values and there is a FoS for the project that takes into account these uncertainties. The final values to be used are show in table C.6.

Table C.6: Final material properties to be used

ν	0.37
σ_y *[MPa]*	20.63
E *[MPa]*	1442.67

Appendix D

Special figures

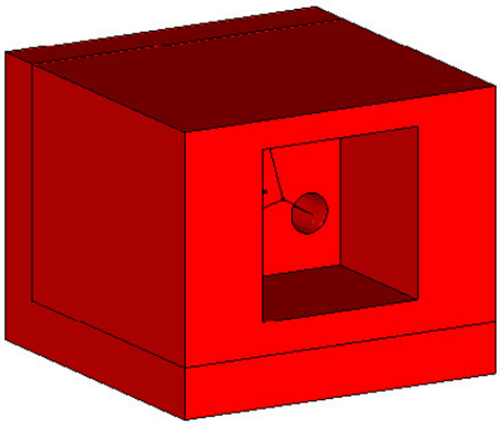

Figure D.1: Animated topology optimization.

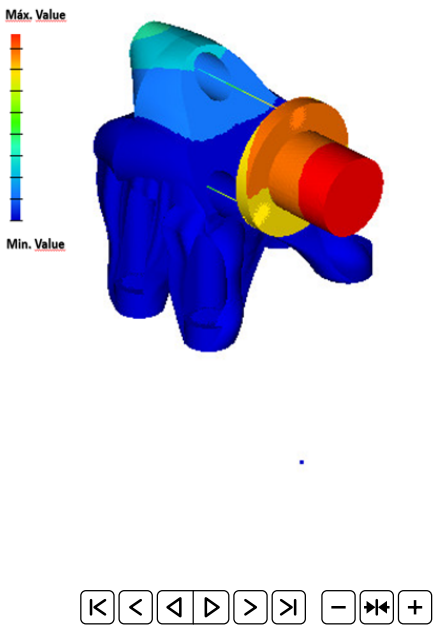

Figure D.2: Animated 1st mode shape on assembly - z displacement.

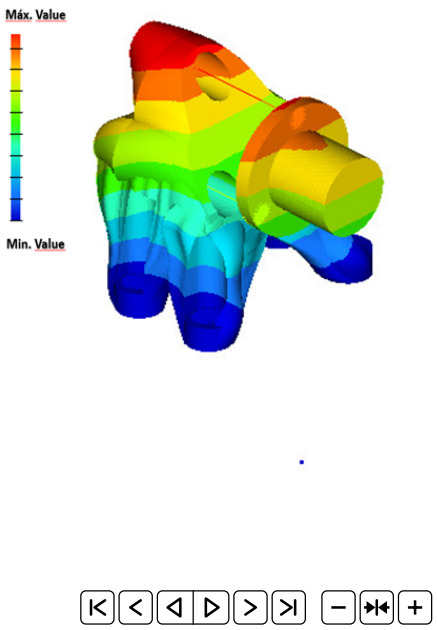

Figure D.3: Animated 2nd mode shape on assembly - z and x displacement with x predominance.

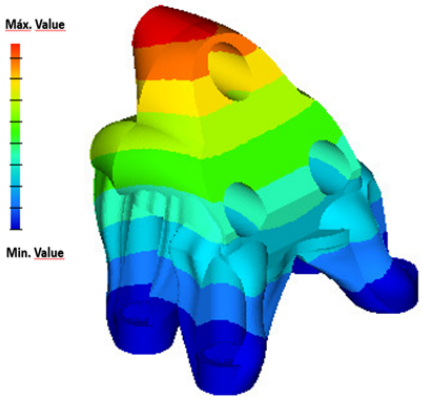

Figure D.4: Animated 1st mode shape on individual structure - z displacement.

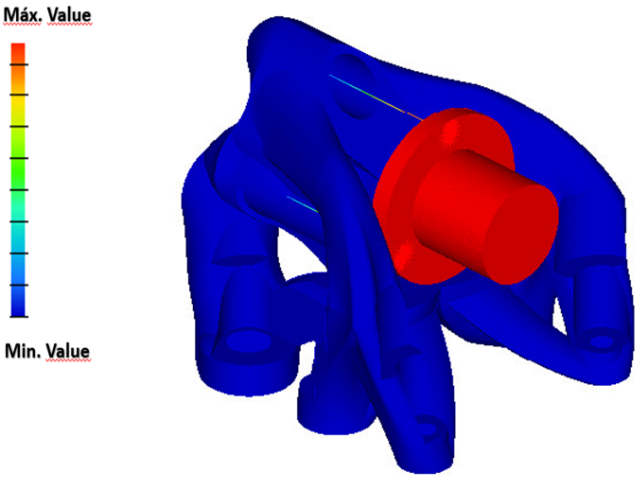

Figure D.5: Animated metal structure assembly's 1st mode frequency.